DOCTORAL THESIS

博士論文

Experimental Study of Dynamic Magnetic Reconnection in Tokamak Plasma Merging Experiment

（トカマクプラズマ合体実験を用いた動的磁気リコネクション現象の実験的研究）

Student No.: **37-117092**

Author: **Qinghong Cao**

曹　慶紅

Academic Supervisor: **Prof. Yasushi Ono**

小野　靖

Department of Electrical Engineering and Information Systmes
Graduate School of Engineering
The University of Tokyo

Submitted in partial fulfillment of the requirements for the degree of

Doctor of Philosophy

June 1, 2020

ABSTRACT

The formation process of magnetic fine structures in the guide-field reconnection with plasmoid dynamics has been investigated in the TS-6 tokamak plasma merging experiment. The evidence of plasmoid, formation of closed flux surface, has been clearly revealed in the two stages of reconnection process, before the initiation of fast reconnection and before entering the impulsive phase, for the first time in the 30-years history of merging-type reconnection experiment. Through the optimization of pickup coils assembly into a limited space using super-high resolution 3D printer ($\leq$ 16 μm), our new 2D magnetic probe array satisfies ion-gyro scale spatial resolution and successfully leads to the following new findings.

A new type plasmoid, two X-points, and two current sheets are formed near the midplane during the early phase of the reconnection. The current sheet between the plasmoid and its parent torus plasma ring is dominant. The plasmoid with parallel plasma current is completely different from the previously reported plasmoid formed in current sheet. Although the formation condition of the plasmoid remains unsolved, we found that the plasmoid does not appear in very low gas pressure discharge. The duration and the axial size of the plasmoid are weakly related to the guide field ratio.

The dynamic evolution of the plasmoid can affect the reconnection speed and common flux ratio that is the ratio of the common flux to peak flux at the magnetic axis of the merging tokamak plasma. During the plasmoid formation, the reconnection is slow due to the plasma pileup in the current sheet and the growth of the plasmoid. After the formation, the plasmoid starts to merge with the two major tokamak plasma rings simultaneously. When the plasmoid fully merges, the reconnection speed increases rapidly and significantly, which is considered to trigger the fast magnetic reconnection (initial fast reconnection).

The plasmoid plays a key role on the ion heating around the X-points. The ions in the outflow area of both X-points are obviously heated. When the plasmoid is completely absorbed to the tokamak plasma rings, the downstream ion heating increases significantly. Right after the plasmoid absorption, the common flux ratio α reaches about 20% and the downstream ion T_i reaches about 10 $\sim$ 12 eV, while the maximum of T_i is about 30 eV after merging (α = 100%). It suggests that a considerable amount

of magnetic energy stored around the current sheets during the plasmoid formation is converted to thermal and kinetic energy of ions, providing the initial ion heating for the spherical tokamak plasma.

The initial fast reconnection lasts a few microseconds, during which the magnetic reconnection is so fast that the newly reconnected flux (common flux) far exceeds its outflow, resulting in the rapid accumulation of common flux around the X-point. And at the same time, the common flux together with the current sheet is strongly compressed into an elongated shape by the two approaching tokamaks, so the X-point shifts outward. As the magnetic reconnection continues, the common flux is almost compressed into antiparallel lines, resulting in the decreasing of the pressure gradient in R direction inside the current sheet. Therefore, the common flux continues to accumulate and the X-point continues to shift outward, forming a transition phase of the magnetic reconnection. During this phase, the antiparallel lines of the common flux have a chance to contact each other, forming a new X-point and another plasmoid inside the current sheet. When the current sheet is compressed to a limit, it will be torn and ejected, maybe accompanied by the plasmoid ejection. The ejection of the current sheet and plasmoid can trigger the reconnection to an impulsive phase and heat the downstream ion significantly.

Although the two types of plasmoid can increase the reconnection speed and heat the downstream ion significantly, their formation regimes are completely different. The first plasmoid (appears early) with parallel plasma current, is formed from a part of the peripheral plasma of the tokamak plasma ring, while the two tokamak plasma rings are still in their respective formation region. Regardless of the discharge gas species, discharge gas pressure, and guide field ratio, it is always observed. Only when the discharge gas pressure is extremely low, it does not appear. It suggests that the first plasmoid has a high reproducibility and can be used as a usual phase to promote reconnection.

The second plasmoid is formed in the current sheet and has antiparallel plasma current. It is observed only when the current sheet is rapidly compressed to be elongated shape in the high guide field merging experiments, but it does not appear very often. Since its small scale, high-resolution magnetic probe array is required. However, it is difficult to achieve high-resolution in both R and Z directions because of the need to

ensure a plasma passing rate in the experiments. Although the current experimental results indicate that the second plasmoid has a poor reproducibility, it may just be that we have not observed it.

Although the plasmoid is the local phenomenon around the X-point and needs to be studied in more detail, it was confirmed that the both types of the plasmoids trigger the fast reconnection and heat downstream ion effectively.

ACKNOWLEDGEMENT

With immense pleasure and deep sense of gratitude, I wish to express my sincere thanks to my supervisor **Professor Yasushi Ono**, without his motivation and continuous encouragement, this research would not have been successfully completed.

I have experienced a series of problems such as suspension from school, returning to school, pregnancy, childbirth, childcare and so on. The study and research was suspended for about four years. I return back to the laboratory again with uneasy feelings. I was very scared of the disgust of teachers and classmates. I hesitated whether I could continue my research in this laboratory or not. Professor Ono patiently encouraged me to say that previous things have passed, work hard and concentrate on the research, you still have an opportunity to make a difference, and eventually get a doctorate. Further, professor Ono, whose preciseness and passion in teaching and research impressed me a lot. Owing to his insightful guidance and advices on my research, the completion of this paper is made possible.

Prof. Michiaki Inomoto, without whose careful and responsible lecture, I would not have acquired the knowledge needed for this academic task. Prof. Takuma Yamada, who taught me how to write program using IDL and how to run the experiment in UTST device. My heart-felt gratitude also goes to my tutor, Dr. Kamio, who gave me a lot of help in my studies.

I am particularly indebted to Dr. Tanabe, who guide me how to prepare and write academic papers, and gave me a lot of advices and comments. A lot of precious knowledge he gave me will benefit me for life.

I give my sincere thanks to my dear friends and fellow students. They setup the experimental device with me, experimented together with me, sharing the joy of the success of the experiment and the sorrow when the experiment dropped in trouble. I am glad to thank sato-san, who helped me a lot in handwork.

My husband's second elder sister and brother-in-law have helped me raise my little daughter for about 4 years, and words can no longer express my gratitude to them. I also want to say thanks to my daughter, thank her for growing up healthily, so that I can continue my studies and researches without worry. I am deeply grateful for my parents' expectation and trust. Last but not the least, I would like to thank my husband for

his constant encouragement and support along with patience and understanding, many thanks to him.

Place: The University of Tokyo

Date: 01/06/2020 **Qinghong Cao**

TABLE OF CONTENTS

LIST OF FIGURES

CHAPTER 1

Introduction

1.1 Background

1.1.1 Nuclear Energy

Everything in the world is made up of atoms. Any atom is composed of a positively charged nucleus and one or more negatively charged electrons that rotate around the nucleus. The atomic nucleus is generally composed of protons and neutrons called nucleons. The ability of nucleus to block spontaneous decay and fission is called nuclear stability, is related to the nucleons number A. Nucleus with too large A is unstable.

Nuclear energy (or atomic energy) is the energy released from the atomic nuclei through through the following three types of nuclear reactions: 1, Nuclear fission between heavy nuclei; 2, Nuclear fusion between light nuclei, 3, Spontaneous nuclear decay of the atomic nucleus. We all know that the equivalent relationship between mass and energy conforms to Albert Einstein's mass-energy equivalence

$$E = mc^2 \tag{1.1}$$

This formula states that the equivalent energy (E) can be calculated as the mass (m) multiplied by the speed of light (c = $\sim$ 3 $\times$ 10^8 m/s) squared. In the process of the above three nuclear reactions, a mass defect inevitably occurs, and the mass defect is assumed to completely convert into kinetic energy, the released nuclear energy ΔE will be huge. Assuming that the mass defect in the nuclear reaction is completely converted into kinetic energy, released energy ΔE is very large.

Currently, the vast majority of electricity from nuclear power is generated by nuclear fission of uranium and plutonium. As we known, the heaviest known nuclides in nature are uranium-235, uranium-238, and small amount of plutonium-244, all of which are unstable. Unstable nuclei can spontaneously emit certain rays and decay into stable nuclei; some heavy nuclei can spontaneously split into two (in a few cases, they can split into three or more) atomic nuclei with similar mass, i.e. nuclear fission, and finally became stable nuclei. The total energy released by the fission of 1 kg of uranium is equal to the chemical energy released by the combustion of 2700 tons of standard coal.

A 1 gigawatt nuclear plant requires only 25 to 30 tons of low enriched uranium fuel per year, and only 10 trucks are needed to transport these nuclear fuels; While a coal-fired power station of the same power requires more than 3 million tons of raw coal each year, and 1000 trains are needed to transport these coal.

There are a considerable amount of uranium, thorium and other fission resources on the earth. If we make full use of their fission energy, they can meet the energy need of human beings for thousands of years. Civilian nuclear power supplied 2,563 terawatt hours (TWh) of electricity in 2018, equivalent to about 10% of global electricity generation, and was the second largest low-carbon power source after hydroelectricity [1, 2]. However, nuclear fission energy is also limited and no inexhaustible. So, it is clean energy, but not renewable energy.

With respect to nuclear safety, there have been many major nuclear accidents to date, including the Chernobyl disaster in the Soviet Union in 1986, the Fukushima Daiichi nuclear disaster in Japan in 2011, the Three Mile Island accident in the United States in 1979, and some nuclear submarine accidents. Therefore, There is a debate about nuclear power. Proponents, such as the World Nuclear Association and Environmentalists for Nuclear Energy, contend that nuclear power is a safe, sustainable energy source (see also Nuclear power proposed as renewable energy) that reduces carbon emissions. Nuclear power opponents, such as Greenpeace and NIRS, contend that nuclear power poses many threats to people and the environment [3]. As a result, nuclear fusion become the focus in international research.

1.1.2 Nuclear Fusion

Compared with nuclear fission fuel, nuclear fusion fuel is more abundant, and it can be said that it is inexhaustible. In the ocean, there are not less than 40 trillion tons of nuclear fusion resources - deuterium, if the controlled nuclear fusion becomes a reality in the early 21st century, the fusion energy of these deuterium will be equivalent to trillions of hundreds of millions of tons of coal, which meet the energy demand of human beings for ten billion years. Further value is that there is almost no radioactive contamination in nuclear fusion reactions. In addition, due to extremely high temperature required for nuclear fusion, once a problem occurs in a link, fusion fuel temperature will drop rapidly, and then the fusion reaction will also terminate spontaneously.

Fusion energy is an ideal energy source for the future. Therefore, mankind has pinned its hopes of solving resource problems on nuclear energy, the future giant of the energy world. It has been over 60 years since the start of research on controllable fusion power generation in the 1950s.

In order for the fusion reaction to take place, the two light nuclei must get enough high velocities to overcome the long-range electrostatic repulsion between them and

approach sufficiently close to penetrate the nuclear potential barrier and undergo fusion, releasing the huge energy contained in the nucleus. Several main possible nuclear fusion reactions are shown below.

$$ {}_1^2D + {}_1^3T \rightarrow {}_2^4He(3.5MeV) + n^0(14.1MeV) \tag{1.2} $$

$$ {}_1^2D + {}_1^2D \rightarrow {}_1^3T(1.01MeV) + p^+(3.02MeV) \tag{1.3} $$

$$ {}_1^2D + {}_1^2D \rightarrow {}_2^3He(0.82MeV) + n^0(2.45MeV) \tag{1.4} $$

$$ {}_1^2D + {}_2^3He \rightarrow {}_2^4He(3.6MeV) + p^+(14.7MeV) \tag{1.5} $$

$$ {}_1^3T + {}_1^3T \rightarrow {}_2^4He + 2n^0 + 11.3MeV \tag{1.6} $$

$$ {}_2^3He + {}_2^3He \rightarrow {}_2^4He + 2p^+ + 12.9MeV \tag{1.7} $$

$$ p^+ + {}_1^3T \rightarrow {}_2^3He + n^0 - 0.764 \tag{1.8} $$

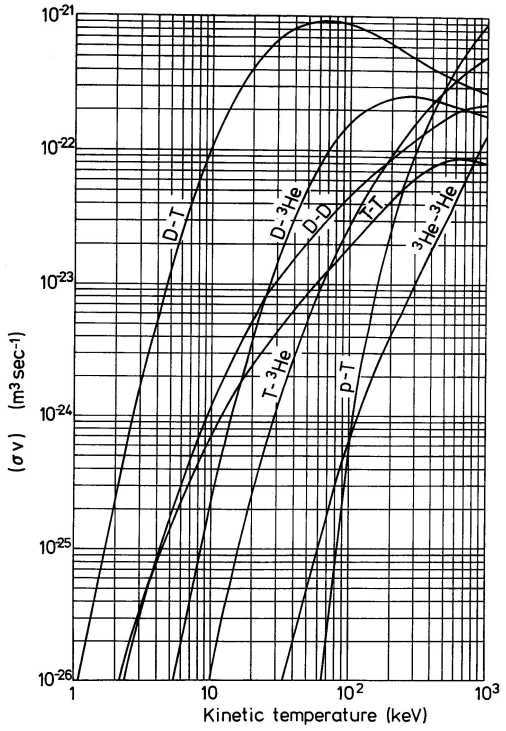

Fig. 1.1 Fusion reaction rates for seven main reactions

Here, D is deuterium, T is tritium, He is helium, p is proton, and n is neutron. These fusion reaction rates are shown in Fig. 1.1 [4]. It can be identified that the Largest fusion reaction rate at relative lower temperature (10 keV to 100 keV) is for D - T fusion, so it is the easiest fusion reaction on the earth. At thermonuclear temperatures of 10^8 K to 10^9 K corresponding to energies of the order of 10 keV to 100 keV (conversion factor: $1\ eV = 11,600^\circ K$), the fusion reactants are ionized to thermonuclear plasma composed of positively charged light atomic nuclei and electrons. The plasma, which is

often regarded as the fourth state of matter of the sequence solid-liquid-gas-plasma, is defined physically and precisely as a quasi-neutral gas of charged and neutral particles which exhibits collective behavior [5]. In other words, although the plasma contains positive and negative charges and neutral particles, it appears to be macroscopically neutrally over a volume.

There are two forms of thermonuclear fusion: 1. Uncontrolled type, which can generate a large amount of thermal energy in an instant, cannot be utilized yet ("hydrogen bombs"). 2. Controlled type refers to confine thermonuclear reaction in a certain area, generating and proceeding it in a controlled manner according to people's intentions. It is exactly the major subject of challenging research field in the world at present. The ultimate goal of using nuclear energy is to achieve controlled nuclear fusion, which is the basis of fusion reactors. Once a fusion reactor succeeds, it can provide the cleanest and inexhaustible energy for human beings forever.

1.2 Magnetic Confinement Fusion

1.2.1 Magnetic Field Configurations

No conceivable material could resist the thermonuclear plasma, so it must be confined in a vacuum to prevent it from directly contacting with the material wall. The key problem in achieving thermonuclear fusion is how to confine the hot plasma. At present, there are two main plasma confinement regimes in experimental research field, inertial confinement and magnetic confinement.

Magnetic confinement fusion using the fact that charged particles spiral about magnetic fields to create magnetic field configurations to confine the hot plasma in a vacuum. There are various magnetic field configuration such as θ - pinch, mirror, stellarator, tokamak, spheromak, reverse magnetic field pinch (RFP), field-reversed configuration (FRC). However, the current mainstream magnetic confinement method is the tokamak [6], which has become the center of fusion research worldwide from the 1970s due to its excellent confinement performance. Experiments on the world's three major tokamak (TFTR, JT-60 [7], JET [8]) have started since the 1980s. TFTR achieved the critical plasma condition $Q = 1$ for the first time in the world, which is equivalent to that human being is obtaining energy gain from fusion reaction [9]. An international nuclear fusion facility called ITER (International Thermonuclear Experimental Reactor) which will be the largest tokamak plasma experiment in the world, is under construction in France by the cooperation of seven member entities - the European Union, India, Japan, China, Russia, South Korea, and the United States (Fig. 1.2 [10]) .

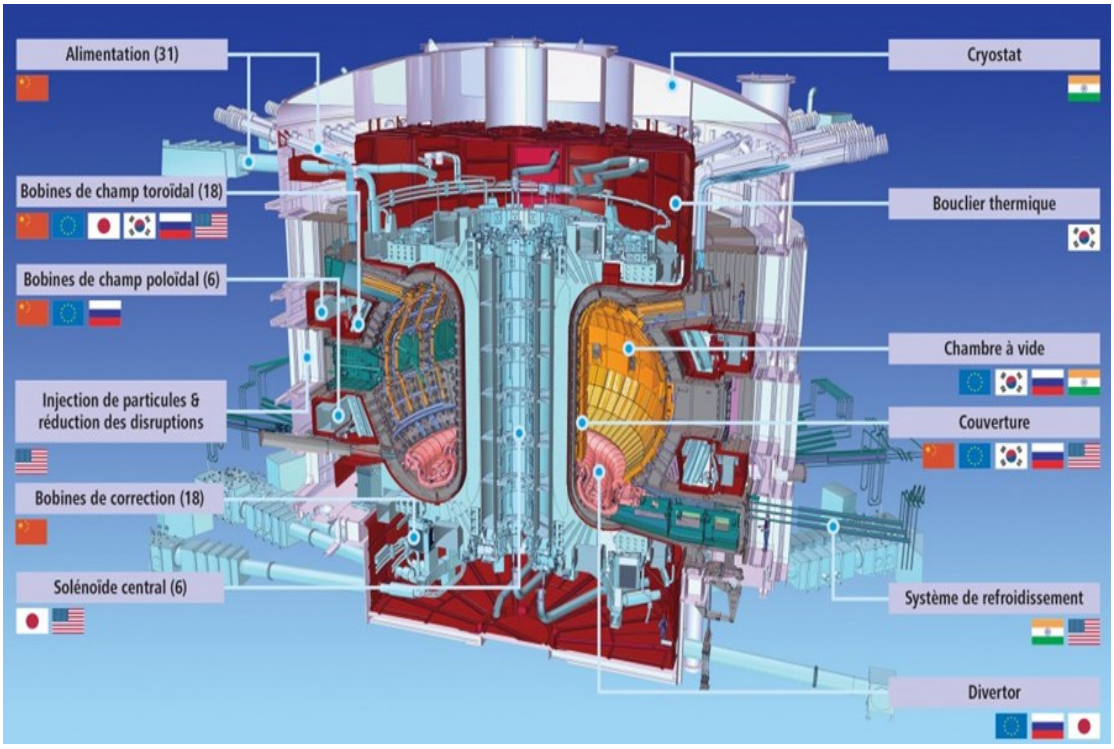

Fig. 1.2 Schematic view of ITER Device

1.2.2 β Value

In order to use fusion reactor as a commercial reactor through the prototype reactor and the demonstration reactor after the ITER device, the tokamak reactor is very large, so it becomes expensive, which is not economically desirable. A value β defined as the ratio of the plasma pressure p to the magnetic pressure $B^2/2\mu_0$ is one important parameter to evaluate the efficiency of a magnetically confined fusion plasma. The higher the β value is, the higher the fusion power density, the higher economic performance of the fusion power plant can be achieved. According to the Troyon rule known as a semi-empirical rule for predicting the upper limit of the β value. Its definition is:

$$\beta_{max} = \beta_N \frac{I_p}{aB_t} \tag{1.9}$$

where B_t is the toroidal magnetic field, a is the minor radius, I_p is the plasma current, and β_N is normalized beta determined numerically by Troyon to 2.8 percent (0.028). There are aspect ratio A, ellipticity κ, and triangle δ as parameters representing the shape feature of tokamak. These elements correlating with plasma performance is defined as $A = R_0/a$, $\kappa = b/a$, $\delta = c/a$, indicated in Fig. 1.3.

Since the upper limit of I_p/aB_t is determined by the kink mode instability of the plasma, β_N needs to be increased in order to increase the β value. In the tokamak system, it is generally known that non-circular cross-section and low aspect ratio A

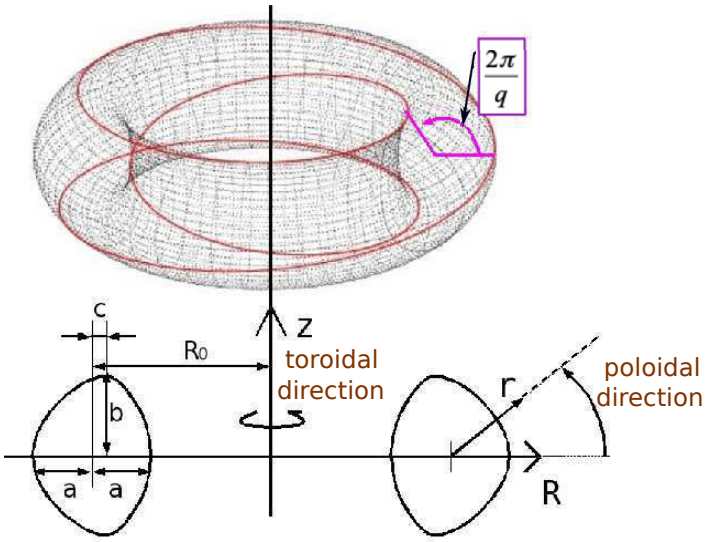

Fig. 1.3 Tokamak geometry parameters

toroidal direction:
Circumferential direction of major circle

poloidal direction:
Circumferential direction of minor circle

major radius: R_0

minor radius: a

aspect ratio: A=R_0/a

ellipticity: κ=b/a

triangle: δ=c/a

safety factor: q=$2\pi/\iota$
ι is the angle rotated in the poloidal direction when the magnetic field lines make one round in the toroidal direction.

improve the β limits significantly. Increasing the ellipticity κ increases the safety factor q, allowing larger plasma current to flow and achieving an expected high β_N. Increasing the three angles δ increases the magnetic well effect, stabilizes the ballooning mode at the periphery, and increases the β value.

1.2.3 Spherical Tokamak

In a tokamak with an aspect ratio smaller than 2, the poloidal cross-section becomes D shape, and it becomes a spherical shape than a donut shape when looking at the appearance. Fusion power device based on the tokamak principle but with this specialized magnetic field configuration is called spherical tokamak (ST) (shown in Fig. 1.4(a)). From the viewpoint of plasma stability, ST confines plasma with a strong toroidal magnetic field compared with conventional tokamak, so the safety factor at the plasma boundary is high and current driven type disruption is unlikely to occur.

Because of its advantages over other devices, ST has rapidly attracted attention as a promising candidate for the realization of inexpensive fusion reactor since the late 1980s. Major large-scale ST experimental devices include pioneering START [11], MAST at Culham in the UK [12], etc. Our ST devices such as TS-3 [13], TS-4 [14], UTST [15] and TS-6 in the University of Tokyo are compact.

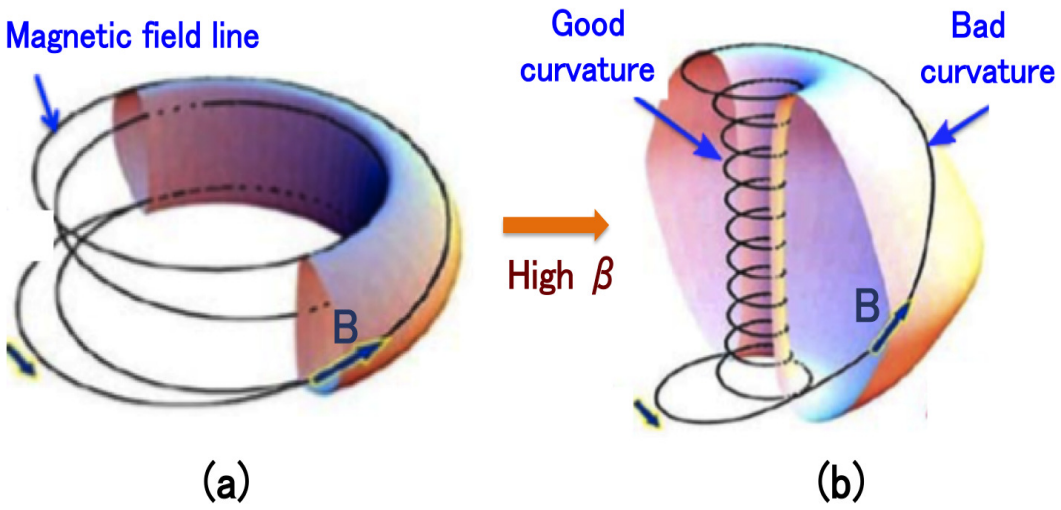

Fig. 1.4 Schematic view of magnetic field lines of (a) Conventional Tokamak and (b) Spherical Tokamak

1.3 Merging Startup of ST

Although the ST has advantages in terms of economy and stability, engineering problems arise due to the small aspect ratio. Since the aspect ratio of ST is small, there is no enough space for arranging center solenoid (CS). Therefore, it is necessary to develop CS-less start-up method for compact ST experimental devices. Several experimental CS-less start-up schemes, such as RF current drive, coaxial helicity injection [16, 17] and two plasmas merging, were proposed and demonstrated. Plasma merging method is a novel plasma start-up scheme to form a high beta ST plasma by utilizing the magnetic reconnection (to be introduced in detail in chapter 2) between two initial torus plasmas, which leads to a rapid conversion from magnetic energy to plasma kinetic or thermal energy. This plasma merging process will provide a drastic increase of the beta value.

In our TS-6 device, when light atomic gas (H_2, He, Ar) is injected from two washer guns that are symmetric in the left and right direction, two torus plasmas are generated independently and merges together through magnetic reconnection to form a single high β ST due to the attraction force of the plasma current. The schematic view of plasma merging process is shown in Fig. 1.5. The effectiveness of this method have been verified in both large devices such as START [11] and MAST [12], and compact devices such as TS-3/4/6 devices [13, 14].

1.4 Dissertation Objectives

The experimental device TS-6 was constructed to study axial merging and heating application of magnetic reconnection. Fast magnetic reconnection has been verified to heat the downstream ion effectively [18]. However, many dynamic issues related to

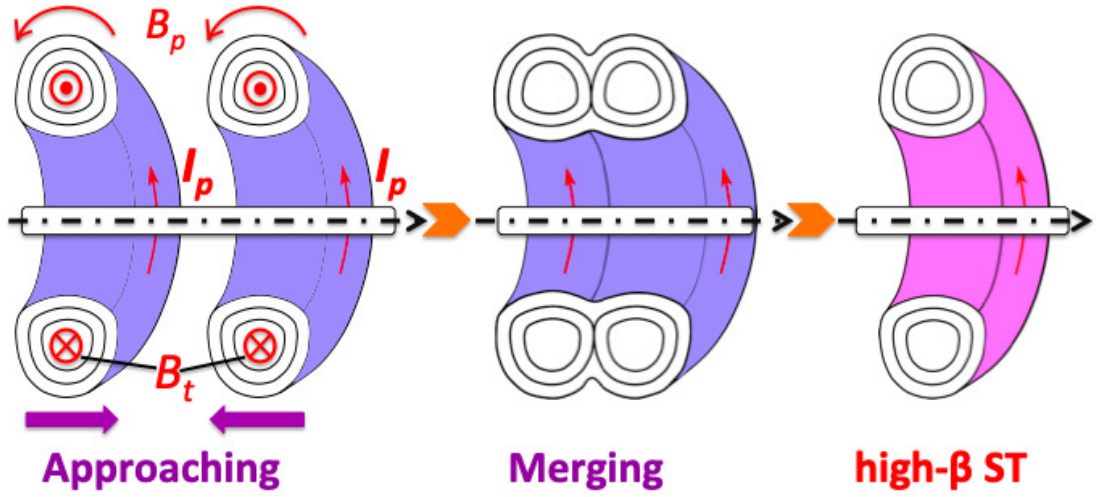

Fig. 1.5 Schematic view of plasma merging process

magnetic reconnection, such as the formation of plasmoid and its effect on magnetic reconnection speed/rate, have not reached consensus. This research intends to investigate dynamic magnetic reconnection in detail by developing a new 2D high-resolution magnetic field measurement system.

Specific objectives of this dissertation can be divided into the following four points.

1. To investigate fine structure (such as plasmoid) and its mechanism in the local reconnection region.
2. To clarify the role of the plasmoid in the fast mechanism of magnetic reconnection.
3. To analyze the effect of the formation and absorption of the plasmoid on ion heating.
4. To investigate the formation conditions and characteristics of the plasmoid.

1.5 Outline of This Dissertation

This dissertation provides a detailed study of dynamics magnetic reconnection in tokamak plasma merging experiment of TS-6 device using a new 2D high-resolution magnetic field measurement system, ion Doppler tomography system, and electrostatic probes.

This dissertation consists of six main chapters:

Chapter 1 is the introduction, mainly introduce the importance of the research of the controlled nuclear fusion reaction, the magnetic confinement fusion, a promising configuration of Spherical Tokamak and its CS-less merging start-up scheme. Finally the objectives are summarized.

Chapter 2 introduces the magnetic reconnection in nature and laboratory experiments, and describes some research models and unsolved questions.

Chapter 3 describes the experimental device of TS-6 and the experimental reset-up method. Some diagnostic systems are introduced.

Chapter 4 presents experimental results of the plasmoid formation during early reconnection phase when two torus plasmas are still in their respective formation regions.

Chapter 5 describes the characteristics of the plasmoid in various operation conditions.

Chapter 6 describes experimental results during fast reconnection phase.

Chapter 7 draws the conclusion of this dissertation.

a

CHAPTER 2

Magnetic Reconnection

2.1 Concept

Among the active solar phenomenon, solar flares and corona mass ejection (CME) are the most intense. Their main feature is the release of great energy in a very short time (minutes to tens of minutes). Since the Sun is very close to the Earth, the release of this energy may have a serious impact on the earth. Known effects include effects on space exploration and aerospace, satellite operations and communications, ground-based communications that rely on the ionosphere, power grids, power facilities, and even oil pipelines. Its influence can be said to cover all aspects of people's lives.

What causes flares and coronal mass ejections which are always accompanied by numerous flares? Although scientists have been trying to clarify the mechanism of their formation, it was not until the introduction of some new observation techniques in the 1990s that observations reached a level sufficient to reveal their complexity and elucidate the physical mechanisms behind them. The key to the problem is the sudden rearrangement of the magnetic field lines, which is called magnetic reconnection.

The concept of magnetic reconnection was originally proposed by Giovanelli in1946 [19], although the terminology he used at that time was not "magnetic reconnection" but "magnetic annihilation". Since then, magnetic reconnection has been recognized as not only one of the fundamental processes in magnetized plasmas but also a mechanism for particle acceleration in solar flares. Fig. 2.1 shows a schematic view of magnetic reconnection. When highly conducting plasmas carrying antiparallel magnetic field lines approach each other, a thin sheet-like current (called "current sheet") is induced around approaching lines. If the highly conductive plasma is place in the framework of ideal magnetohydrodynamics (MHD), magnetic field lines move with the plasma and remain intact. However, when a pair of antiparallel field lines are close to each other, current sheet is compressed and its resistivity will increase, then the plasma around this small area can no longer be regarded as ideal MHD model. Therefore, when this pair of antiparallel magnetic field lines collide together and form a magnetic neutral point (X-Point), since the non-ideal MHD effect is locally dominant, the dissipation of the current sheet will allow the plasma to diffuse, then magnetic field lines break

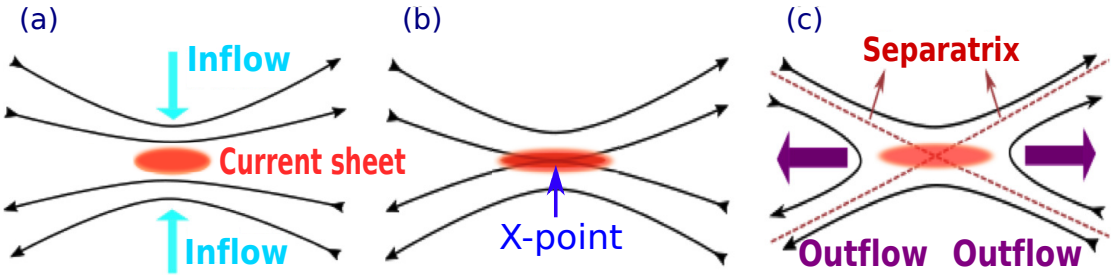

Fig. 2.1 Schematic view of magnetic reconnection. (a) Before reconnection, (b) During reconnection, (c) After reconnection. Orange region indicate the current sheet, light blue arrows and purple arrows show inflow and outflow directions, respectively.

and reconnect to rearrange their topologies around the diffusion region, then magnetic reconnection occurs [20].

We can see that, with the ongoing reconnection, the individual field lines lose their original identity where they pass through a local diffusion region. Newly reconnected field lines have high tension and therefore quickly flow away from the diffusion region. During this fast tension release, released magnetic energy is converted to kinetic energy, thermal energy, radiation, and so on.

Magnetic reconnection involves global and local processes. Therefore, the dynamics of reconnection depends on both the global boundary conditions and the local plasma parameters. Moreover, it seems that there is a complex coupling between the local and global scales, which makes magnetic reconnection even more challenging. This is why, in despite of the progress made in the past few decades, a lot of effort is still needed to understand this intriguing phenomenon. Magnetic reconnection has been studied whether in space and astronomical observations, or theoretical and numerical simulations, or laboratory experimental plasmas [21].

2.2 Examples of Magnetic Reconnection in Nature and Laboratory Experiments

2.2.1 Magnetic Reconnection on the Sun

The solar atmosphere is full of magnetic field. The more complex the magnetic field structure, the easier it is to store more magnetic energy. When there is too much magnetic energy stored in the magnetic field, this energy will be released through the solar explosion activity. Long-term observations have found that most flares occur above the sunspot group, and the more complex the structure and magnetic field polarity of the sunspot group, the higher the probability of occurrence of large solar flares. Solar flare is one of the most explosive phenomena among dynamic solar activities. The duration of the solar flare varies from a few minutes to tens of minutes. During this short time,

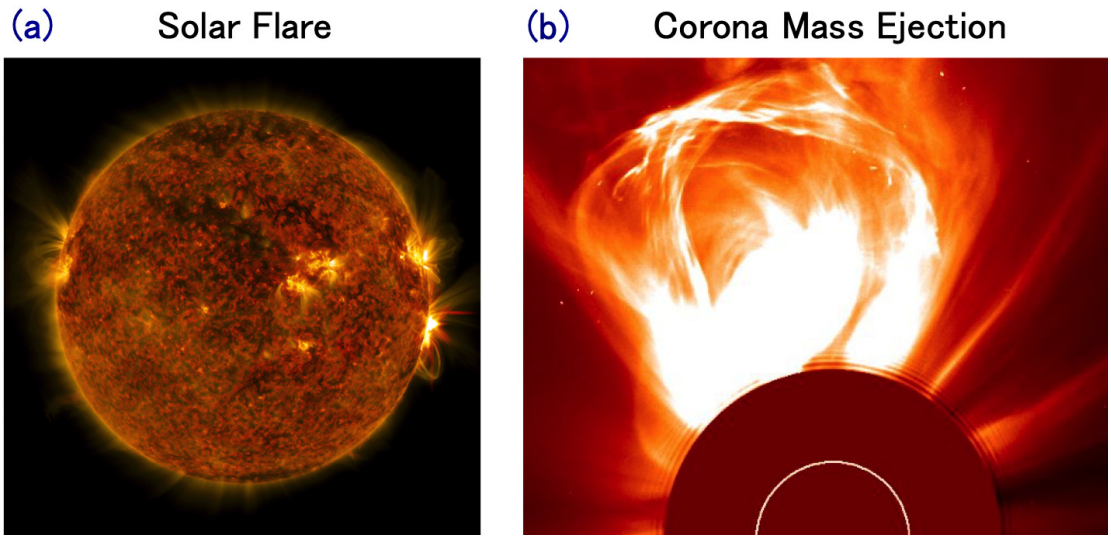

Fig. 2.2 (a) An X8.2 class solar flare flashes in the edge of the Sun on Sept. 10, 2017. (b) Coronal mass ejection of February 27, 2000. The white circle indicates the sun's surface.

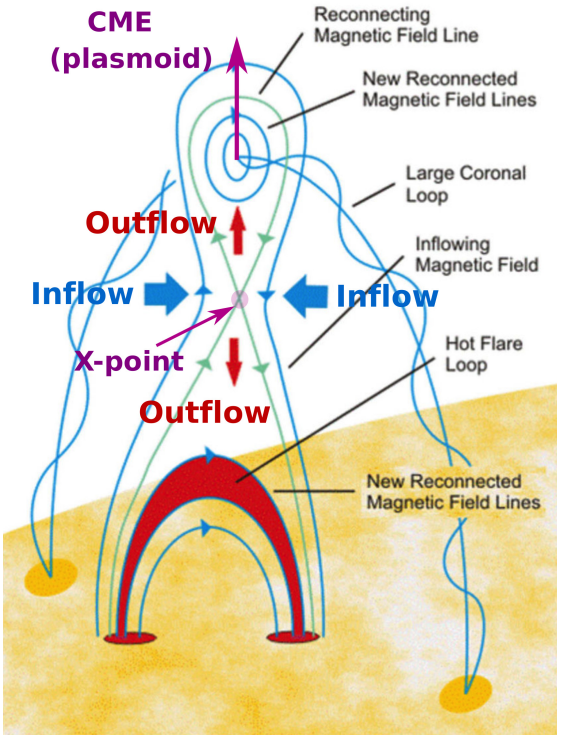

Fig. 2.3 An illustrated model of magnetic reconnection and solar flare diagram.

solar flare can release a huge energy of $10^{20} \sim 10^{25}$ joules. It is widely believed that solar flares result from a rapid release of magnetic energy stored in the solar coronal magnetic field through magnetic reconnection. Figure 2.2(a) [22] shows an X8.2 class solar flare flashes on the edge of the Sun on September 10, 2017, which was captured by NASA's Solar Dynamics Observatory and shows a blend of light from the 171 and 304 angstrom wavelengths. Figure 2.2(b) [23] shows a Coronal Mass Ejection on February 27, 2000. A disk is being used to block out the light of the sun. Figure 2.3 [24] is a model of magnetic reconnection and solar flare diagram. When a pair of antiparallel magnetic field lines collide together, magnetic reconnection occurs. Corona Mass Ejection (CME) is formed by the plasmoid ejected from the surface of the Sun. When the energetic particles in the outflow close to the surface of the sun travel along the magnetic field and collide with the dense chromosphere plasma, they generate bursts of light called hot flare loop.

2.2.2 Magnetic Reconnection in the Earth's Magnetosphere

Due to the interaction with the solar wind, the geomagnetic field are compressed and stretched very far away, thus forming a magnetotail on the nightside of the Earth's magnetosphere as shown in Fig. 2.4 [25]. Magnetic reconnection is now believed to play an important role in this dynamic interaction between the geomagnetic field and the solar wind, and considered to occur in both the dayside and the nightside of the Earth's magnetosphere at the same time. Dungey's original picture of reconnection in the Earth's magnetosphere has also been supported by many in situ satellite observations [26]. However, when Dungey first applied the concept of magnetic reconnection to the study of the magnetosphere and established the first open magnetosphere model, the Dungey model was not immediately accepted. Part of the reason is that it took a long time for people to gradually understand the process of magnetic reconnection and its importance.

Observations of modern advanced satellites and spacecrafts have confirmed that the magnetic reconnection occurring in the dayside deforms the configuration of the geomagnetic field at the two poles, and the solar wind causes the magnetic flux and plasma flow to the magnetotail. When the almost antiparallel magnetic field lines are approaching each other in the magnetotail, a neutral sheet develops with the magnetic field approximately zero. The dense plasma is filled around the neural sheet, and its equivalent temperature is about 10 million degrees. The energy transmitted by the solar wind to the earth's magnetosphere is mainly stored there. Magnetic reconnection occurs when almost antiparallel magnetic field lines meet and collide together, forming a magnetic neutral point (X-point) at the center of neutral sheet. After reconnection, incoming magnetic flux and plasma are released into the outer space and the inner magnetosphere,

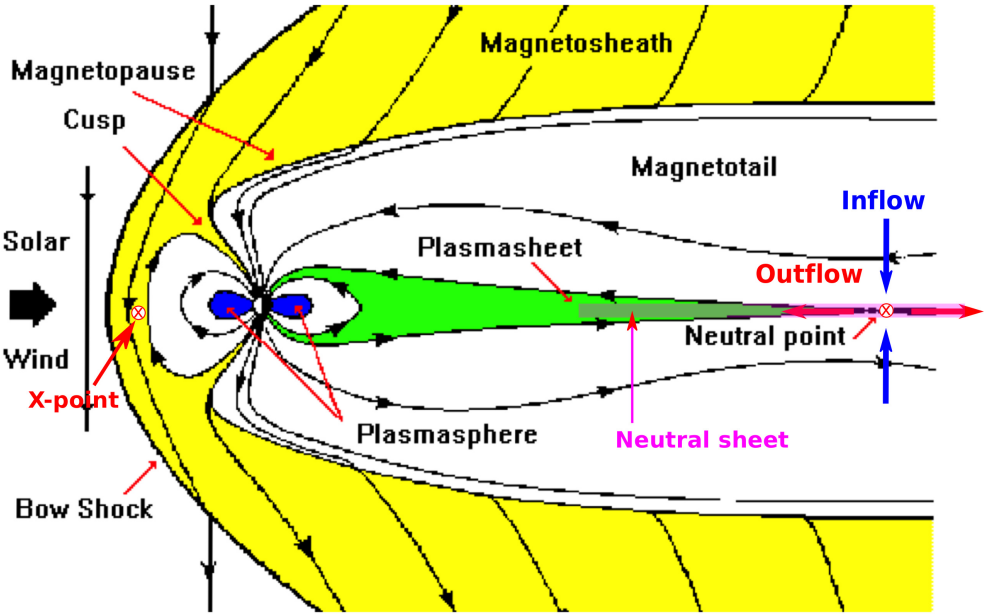

Fig. 2.4 Schematic view of magnetic reconnection in the earth's magnetosphere.

and most of the latter are injected into the poles of the Earth along the magnetic field lines to feed Aurora occurrence.

Cluster II has observed numerous reconnection events in which the Earth's magnetic field reconnects with that of the Sun. These include "reverse reconnection" that causes sunward convection in the Earth's ionosphere near the polar cusps; "dayside reconnection", which allows the transmission of particles and energy into the Earth's vicinity and "tail reconnection", which causes auroral substorms by injecting particles deep into the magnetosphere and releasing the energy stored in the Earth's magnetotail [27]. The Magnetospheric Multiscale Mission, launched on 13 March 2015, improved the spatial and temporal resolution of the Cluster II results by having a tighter constellation of spacecraft. This led to a better understanding of the behavior of the electrical currents in the electron diffusion region [28]. On 26 February 2008, THEMIS probes were able to determine the triggering event for the onset of magnetospheric substorms [29]. Two of the five probes, positioned approximately one third the distance to the Moon, measured events suggesting a magnetic reconnection event 96 seconds prior to auroral intensification [30]. Dr. Vassilis Angelopoulos of the University of California, Los Angeles, who is the principal investigator for the THEMIS mission, claimed, "Our data show clearly and for the first time that magnetic reconnection is the trigger." [31]

2.3 Frozen-in Magnetic Fields

As the charged particles in a plasma move around, they can generate local concentrations of positive or negative charge which give rise to electric fields. Motion of these

charges generates electric currents which produces magnetic field. When the density of plasma is high enough the whole plasma can be considered as a single charged species, and hence a single conducting fluid. A simplified concept of assumption is known as MHD theory.

Now, let us consider the resistive MHD equations, for a non-viscous magnetized plasma, we write the generalized Ohm's law and Faraday's law as

$$\boldsymbol{E} + \boldsymbol{v} \times \boldsymbol{B} = \eta \boldsymbol{j} \tag{2.1}$$

$$\boldsymbol{\nabla} \times \boldsymbol{E} = -\frac{\partial \boldsymbol{B}}{\partial t} \tag{2.2}$$

Here η is the plasma resistivity. Taking curl of Eq. (2.1) we obtain

$$\boldsymbol{\nabla} \times \boldsymbol{E} = \boldsymbol{\nabla} \times (\boldsymbol{\eta j}) - \boldsymbol{\nabla} \times (\boldsymbol{v} \times \boldsymbol{B}) \tag{2.3}$$

From Eq. (2.2) and Eq. (2.3) we have

$$\frac{\partial \boldsymbol{B}}{\partial t} = \boldsymbol{\nabla} \times (\boldsymbol{v} \times \boldsymbol{B}) - \boldsymbol{\nabla} \times (\boldsymbol{\eta j}) \tag{2.4}$$

Since Ampère's law is

$$\boldsymbol{\nabla} \times \boldsymbol{B} = \mu_0 \boldsymbol{j} \tag{2.5}$$

Eq. (2.4) can be described as

$$\frac{\partial \boldsymbol{B}}{\partial t} = \boldsymbol{\nabla} \times (\boldsymbol{v} \times \boldsymbol{B}) + \frac{\eta}{\mu_0} \boldsymbol{\nabla}^2 \boldsymbol{B} \tag{2.6}$$

The first term and second term of Eq. (2.6) on the right-hand side represent the advection of field by the flow, and a diffusion of the magnetic field due to the resistivity, respectively.

Since the resistivity of highly conducting plasma is very small, substituting $\eta \simeq 0$, Eq. (2.6) can be simplified to

$$\frac{\partial \boldsymbol{B}}{\partial t} = \boldsymbol{\nabla} \times (\boldsymbol{v} \times \boldsymbol{B}) \tag{2.7}$$

Eq. (2.7) is the idealized MHD equation for non-viscous and non-resistive magnetized plasma.

If we consider an arbitrary open surface S bounded by a closed circumference l moving with idealized MHD plasma velocity $\boldsymbol{v}$, the magnetic flux Ψ through S at any time t is

$$\Psi = \int_S \boldsymbol{B} \cdot d\boldsymbol{S} \tag{2.8}$$

The flux may change due to time variations of $\boldsymbol{B}$ or due to the surface moving with the plasma fluid element to a new position, the total rate of change of flux is obtained by integrating along around the circumference of S. Thus

$$\frac{d\Psi}{dt} = \int_S \frac{\partial \boldsymbol{B}}{\partial t} \cdot d\boldsymbol{S} + \oint_l \boldsymbol{B} \cdot (\boldsymbol{v} \times d\boldsymbol{l}) \tag{2.9}$$

Since Stoke's theorem is

$$\begin{aligned} \oint_l \boldsymbol{B} \cdot (\boldsymbol{v} \times d\boldsymbol{l}) &= -\oint_l (\boldsymbol{v} \times \boldsymbol{B}) \cdot d\boldsymbol{l} \\ &= -\int_S \boldsymbol{\nabla} \times (\boldsymbol{v} \times \boldsymbol{B}) \cdot d\boldsymbol{S} \end{aligned} \tag{2.10}$$

Hence, Eq. (2.9) is written as

$$\frac{d\Psi}{dt} = \int_S \left[\frac{\partial \boldsymbol{B}}{\partial t} - \boldsymbol{\nabla} \times (\boldsymbol{v} \times \boldsymbol{B}) \right] \cdot d\boldsymbol{S} \tag{2.11}$$

Inserting Eq. (2.7) we have

$$\frac{d\Psi}{dt} = 0 \tag{2.12}$$

Eq. (2.12) is called "frozen-in" condition. The magnetic flux through any open surface moving with a highly conducting fluid is constant. This statement is known as Alfvén theorem [32]. It implies that magnetic field lines are "frozen" into the plasma and are transported with it by any motion of the fluid perpendicular to the field lines. Since any velocity component parallel to $\boldsymbol{B}$ gives no contribution to the term $\boldsymbol{u} \times \boldsymbol{B}$, there will be no restriction on the motion of the fluid along the field lines [33].

In Eq. (2.6), the magnetic field lines are not exactly tied to the plasma but can "slip" this distance. If this distance is small enough compared to the typical scale of the plasma then we can consider the magnetic field as frozen even if the resistivity is not exactly zero. In this case, the plasma and the magnetic field lines are in a frozen state with each other, which can be considered as a whole.

If it is assumed that the occurrence of the magnetic reconnection is completely dominated by the "global diffusion", the time scale of magnetic reconnection will be calculated by the diffusion time, i.e. [34]

$$\tau_R = \tau_D = \frac{\mu_0 L^2}{\eta} \tag{2.13}$$

Here, L is a characteristic length scale of the system, μ_0 is the permeability of free space, and η is plasma resistivity. For a typical solar flare, τ_D is about 10^{14}s, while the observed duration of a solar flare is less than 10^3s [35]. The huge gap between theory and observations shows that the former is at least not adequate or insufficient.

2.4 Theoretical Models of Magnetic Reconnection

2.4.1 Sweet-Parker model: Slow Reconnection

The Sweet-Parker model intends to explain the fast magnetic reconnection in solar flare. Peter Sweet proposed a two-dimensional magnetic reconnection model at a conference in 1956. Eugene Parker was in attendance at this conference and developed scaling relations for this model during his return travel [36]. Sweet also independently completed this quantitative theoretical model in 1958 [37]. The Sweet–Parker model introduces the concept of a current sheet and describes time-independent magnetic reconnection in the resistive MHD framework. The plasma inside the current sheet is assumed to be incompressible, non-viscous, and based on the Spitzer resistivity [38]. The physical process inside the current sheet is also assumed in a steady state. Figure 2.5 shows a configuration of Sweet-Parker model which is characterized by the following parameters.

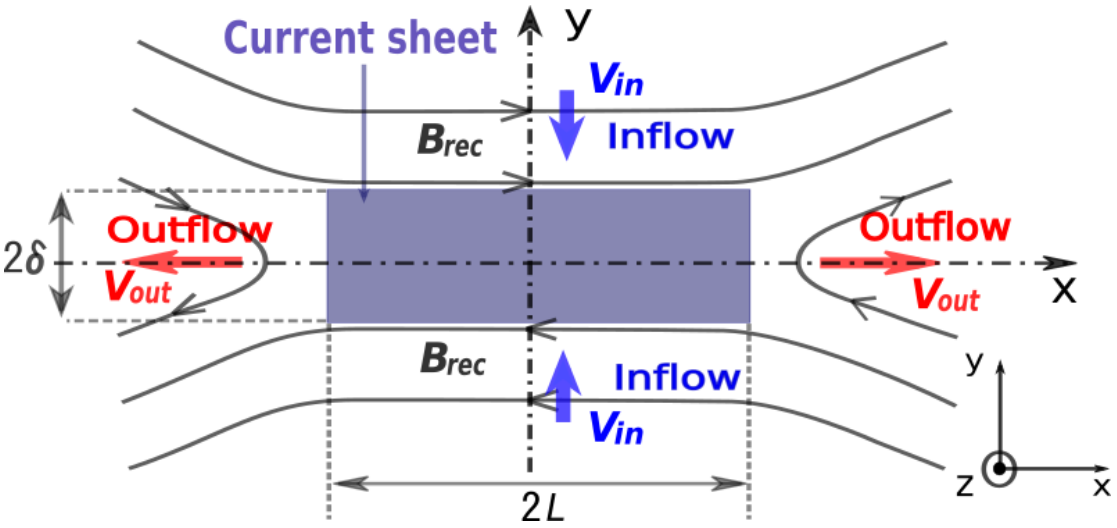

Fig. 2.5 Schematic view of Sweet-Parker model.

1. δ: half-width of the current sheet
2. L: half-length of the current sheet ($L \gg \delta$)
3. V_{in}: the inflow velocity in y direction
4. V_{out}: the outflow velocity in x direction
5. η: the plasma resistivity in current sheet
6. ρ_m: the mass density of plasmas in current sheet

7. B_{rec}: the (poloidal) magnetic field B (almost along x axis) immediately outside the current sheet, called the upstream filed or reconnection field.

From the generalized Ohm's law Eq. (2.1), the electric field is described as

$$\boldsymbol{E} = -\boldsymbol{v} \times \boldsymbol{B} + \eta \boldsymbol{j} \tag{2.14}$$

Considering the boundary conditions inside and outside the current sheet, there are

- Inner region solution:
  Because the current sheet is very thin, and the magnetic field lines on both sides are merging, so there is $\boldsymbol{v_y} \approx 0$ in the inner region. Hence, the uniform E_z can be described as
  $$E_z = \eta j_z \tag{2.15}$$

- Outer region solution:
  Because the plasma outside the current sheet is ideal MHD, so there is no resistivity, i.e. $\eta \approx 0$ in the outer region, Hence
  $$E_z = -V_{in} B_{rec} \tag{2.16}$$

Applying Ampère circuital law, Eq. (2.5) is integrated along the edge of the current sheet, we get

$$\oint_S (\boldsymbol{\nabla} \times \boldsymbol{B}) \cdot d\boldsymbol{S} = \oint_l \boldsymbol{B} \cdot d\boldsymbol{l} = \oint_S \mu_0 \boldsymbol{j} \cdot d\boldsymbol{S} \tag{2.17}$$

Hence ($B_y = 0 \rightarrow 4LB_{rec} = \mu_0 j_z 4L\delta$)

$$B_{rec} = \mu_0 j_z \delta \tag{2.18}$$

By combining Eq. (2.15), Eq. (2.16), and Eq. (2.18), we get

$$V_{in} = \frac{j_z}{\mu_0 \delta} \tag{2.19}$$

Applying the continuity equation of fluid (or conservation of mass) for the current sheet, there is

$$V_{in} L = V_{out} \delta \tag{2.20}$$

Next, considering the steady state or equilibrium conditions, there are

$$\boldsymbol{j} \times \boldsymbol{B} = \boldsymbol{\nabla} p \tag{2.21}$$

$$\boldsymbol{\nabla} \cdot \boldsymbol{B} = 0 \tag{2.22}$$

Here, p is plasma kinetic pressure. Eq. (2.21) describes the balance between the plasma kinetic pressure gradient force and Lorentz-force on each fluid element. It indicates that $\boldsymbol{j}$ and $\boldsymbol{B}$ are perpendicular to $\boldsymbol{\nabla} p$, or in other words, $\boldsymbol{j}$ and $\boldsymbol{B}$ must lie on surface of constant pressure. Combining Eq. (2.21) and Eq. (2.5) to obtain

$$\boldsymbol{\nabla} p = \frac{1}{\mu_0}(\boldsymbol{\nabla} \times \boldsymbol{B}) \times \boldsymbol{B} = \frac{1}{\mu_0}\left[(\boldsymbol{B} \cdot \boldsymbol{\nabla})\boldsymbol{B} - \frac{1}{2}\boldsymbol{\nabla}(B^2)\right]$$

or

$$\boldsymbol{\nabla}(p + \frac{B^2}{2\mu_0}) = \frac{1}{\mu_0}(\boldsymbol{B} \cdot \boldsymbol{\nabla})\boldsymbol{B} \tag{2.23}$$

If the field $\boldsymbol{B}$ does not vary along $\boldsymbol{B}$. Eq. (2.23) can be written to

$$p + \frac{B^2}{2\mu_0} = constant \tag{2.24}$$

Here, $\frac{B^2}{2\mu_0}$ is magnetic field pressure. For the current sheet, in view of its incompressibility, the magnetic energy of the upstream inflow is considered to fully convert into kinetic energy of the downstream outflow. Equating the upstream magnetic pressure with the downstream dynamic pressure gives

$$\frac{B_{rec}^2}{2\mu_0} = \frac{\rho {V_{out}}^2}{2} \tag{2.25}$$

Eq. (2.25) can also be rewritten as

$$V_{out}^2 = V_A^2 = \frac{B_{rec}^2}{\mu_0 \rho} \tag{2.26}$$

Here, V_A is Alfvén velocity. Eq. (2.26) states that the outflow velocity in the downstream reaches the Alfvén velocity owing to magnetic reconnection.

Using above relations, Mach number M can be expressed as

$$M = \frac{V_{in}}{V_{out}} = \frac{\delta}{L} \tag{2.27}$$

or

$$M = \frac{V_{in}}{V_A} = \frac{1}{\sqrt{S}} = \sqrt{\frac{\eta}{V_A L}} \tag{2.28}$$

Where S is dimensionless Lundquist number:

$$S = \frac{\mu_0 L V_A}{\eta} \tag{2.29}$$

In Sweet-Parker model, the diffuse distance of the magnetic field lines is just δ, which reduces the diffuse time scale significantly. Therefore, the Sweet-Parker recon-

nection time is expressed by the geometric mean of the diffuse time and Alfvén time as

$$\tau_{SP} = \sqrt{\tau_D \tau_A} = \sqrt{S}\tau_A \tag{2.30}$$

Where $\tau_D = \frac{L^2 \mu_0}{\eta}$ and $\tau_A = \frac{L}{V_A}$. Taking a typical solar flare as an example, S is about 10^{14}, according to this calculation, the Sweet-Parker reconnection time is about 10^7s. Although Sweet-Parker reconnection is much faster than global diffusion, narrowing the huge gap between the theory and observation, it is not adequate for the fast magnetic reconnection in the solar flare. Generally, Sweet-Parker reconnection is also called slow reconnection.

2.4.2 Petschek Model: Fast Reconnection

One of the reasons why Sweet–Parker reconnection is slow is that the aspect ratio of the diffusion region is very large in high Lundquist number plasmas. It is like, although all fluids have to pass through the diffusion region, the entrance is too large and the exit is too small, resulting in "queuing up" of the merging magnetic field lines that have been very close to the diffusion region, that is, magnetic flux piles up there [39].

In 1964, Harry Petschek proposed a fast magnetic reconnection mechanism to solve the discrepancy between the Sweet-Parker model and observation in solar flare. Figure 2.6 shows a configuration of Petschek reconnection model, which is characterized by the following features.

1. The topology of the reconnection region is a two-dimensional structure with X-shaped separatrices, the length scale of the system is denoted by L.

2. Only part of fluid needs to pass through the diffusion region, which saves the diffusion time (τ_D).

3. The length ($2L^*$) of the inflow and the width (2δ) of the outflow are about in the same order of magnitude, which reduces the Alfvén time (τ_A) significantly owing to $L^* \ll L$.

4. Two pairs of slow mode shocks in the Trumpet-shaped regions also reduce the Alfvén time (τ_A) by accelerating the outflows.

In this mechanism, the maximum of the Mach number is estimated as

$$M = \frac{\pi}{8 \ln S} \tag{2.31}$$

M calculated from this expression is approximately three orders of magnitude faster than the Sweet-Parker model. It seems that it can explain the fast process of solar flare well. Therefore, it has been widely accepted and applied by people for a long time.

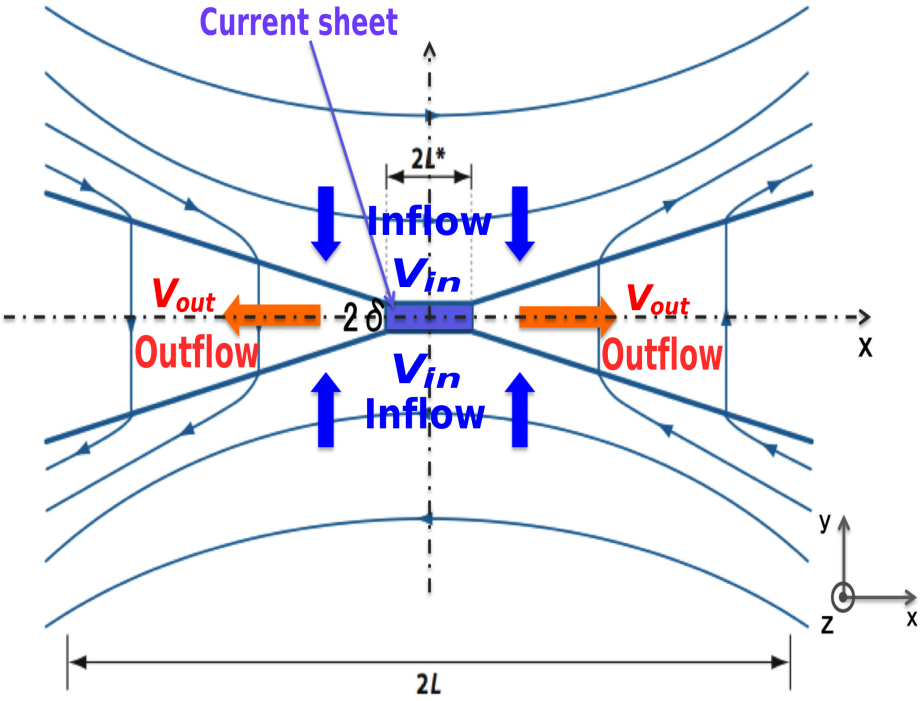

Fig. 2.6 Schematic view of Petschek model. The diffusion layer is thin, and only part of the fluid needs to pass through the layer. Original figure from Zweibel and Yamada, 2009.

But two decades later, it was found that Petschek's theory is not supported by MHD simulations. Under the framework of uniform resistive MHD that the physical discussion of the Petschek model relied on, it was impossible to obtain X-shaped magnetic field geometry structure [40], unless an anomalous resistivity is locally enforced in the diffusion region [41].

At this time, researchers realized that although the magnetic field topology of the Petschek model was proposed to increase the reconnection rate (This is undoubtedly the correct consideration), the physical model of the resistive MHD used is inappropriate. The most accurate fast magnetic reconnection model relies on the development of the collisionless magnetic reconnection theory in the 1990s. Since then, two main different candidates for collisionless reconnection have been studied: (1) anomalous resistivity at the diffusion region; (2) two-fluid effects in the diffusion region due to the fundamental length scale difference between ions and electrons.

2.5 The Mechanism of Fast Magnetic Reconnection

2.5.1 Two-Fluid Effects

The importance of two-fluid effects in the diffusion region was first recognized by Sonerup [42]. Aa we all know, the Larmor radius of electrons and ions are

$$\rho_e = \frac{\sqrt{k_B T_e / m_e}}{\omega_{ce}} = \frac{\sqrt{k_B T_e m_e}}{eB} \tag{2.32}$$

$$\rho_i = \frac{\sqrt{k_B T_i / m_e}}{\omega_{ci}} = \frac{\sqrt{k_B T_i m_i}}{ZeB} \tag{2.33}$$

Here, $\omega_{ce} = \frac{eB}{m_e}$ and $\omega_{ci} = \frac{ZeB}{m_i}$ are cyclotron frequency (or gyrofrequency) of electrons and ions respectively, k_B is Boltzmann's constant, Z is ion charge. Since $m_i \approx 1838 m_e$, ρ_i is much larger than ρ_e. As a result, when the ion becomes unmagnetized and decouples form the electron, the electron is still frozen in the magnetic field line and moves with it. As shown in Fig. 2.7, unmagnetized ions form an ion diffusion region, the

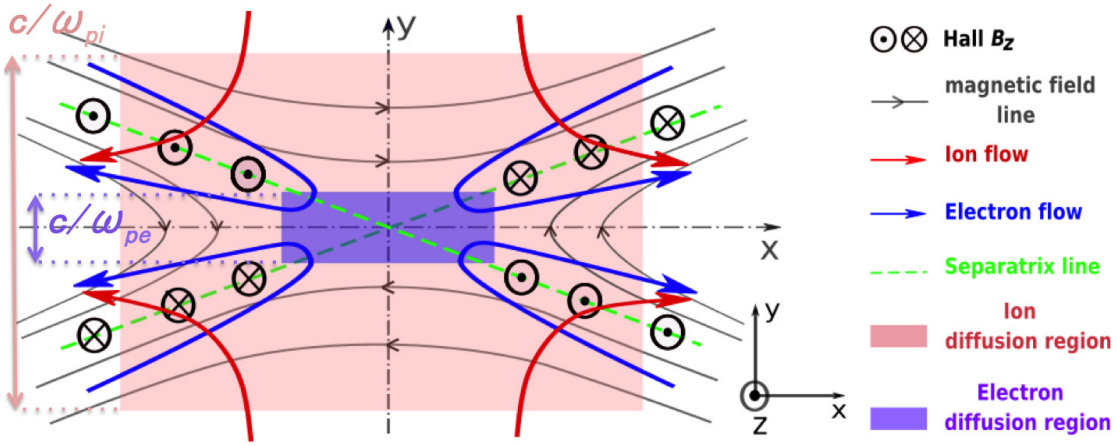

Fig. 2.7 Schematic view of two-fluid effects in magnetic reconnection. Ions decouple from electrons in the ion diffusion region whose width is on the order of ion inertial length d_i. Electrons are frozen in the magnetic field lines until they reach to the electron diffusion region with a width comparable to the electron skin depth d_e.

width of which is on the order of the ion inertial length d_i, while the electrons become unmagnetized until they reach to the electron diffusion region with a small scale whose width is comparable to the electron skin depth d_e. d_e and d_i are calculated by

$$d_e = \frac{c}{\omega_{pe}} = c\sqrt{\frac{\epsilon_0 m_e}{n_e e^2}} \tag{2.34}$$

$$d_i = \frac{c}{\omega_{pi}} = c\sqrt{\frac{\epsilon_0 m_i}{Z^2 n_i e^2}} \tag{2.35}$$

Here, $\omega_{pe} = \sqrt{\frac{n_e e^2}{\epsilon_0 m_e}}$ and $\omega_{pi} = \sqrt{\frac{Z^2 n_i e^2}{\epsilon_0 m_i}}$ are, respectively, electron plasma frequency and ion plasma frequency (oscillation frequency), ϵ_0 is vacuum permittivity.

The electrons magnetized in the ion diffusion region, flow in along the reconnecting field lines in the inflow region and out along the reconnected lines in the outflow regions, which form an electron pattern current. The difference behavior of ions and electrons leads to a strong Hall effect from the $\boldsymbol{J} \times \boldsymbol{B}$ force inside the ion diffusion region. The in-plane electron pattern currents distributed in quadrupoles around the separatrices also creates the quadrupole out-of-plane magnetic filed, a signature of the Hall effect.

Hall magnetic field exerts the Lorentz force on ion outflows, allowing them to have two trumpet-shaped outlets, which is similar to Petschek model. The difference of electric potential between the upstream and downstream is considered to play an important role in fast reconnection. If there is no guide-field, Hall effect makes the plasmas form high electric potential in the upstream where ions remain, and low one in the downstream where electrons flow out. If there is a guide-field, Hall effect causes the ions and the electrons form a quadrupole distribution around X-point, the Hall electric field (E_x or E_r) is considered to accelerate the reconnection.

It is now widely believed that two-fluid effects facilitate fast reconnection. Fast reconnection due to two-fluid effects has been verified by the combined efforts of numerical simulations, space observations, and laboratory experiments [21].

2.5.2 Anomalous Resistivity

In Sweet-Parker model, the magnetic reconnection speed (= Mach number M) us proportional to the square root of the resistivity ($\sim \sqrt{\frac{\eta}{V_A L}}$), so it is considered that the reconnection speed increases when the resistivity increases abnormally (often called anomalous resistivity) due to the microscopic instabilities in the current sheet. Anomalous resistivity has been considered as a fast reconnection mechanism for a long time.

In our experiments of TS-3 device, the current sheet is compressed rapidly when the reconnection is driven by the strong external force. It has been confirmed that the reconnection speed increases significantly when the half-width of current sheet becomes smaller than ion Larmor radius ρ_i during fast compressing reconnection [43]. This is because the ions can not continue the cyclotron motion in the thin current sheet, thereby the plasma can not be regarded as one-fluid. Similar results have been observed with Princeton-sized MRX equipment [44].

At present, ρ_i is concluded to be a key parameter to trigger the anomalous resistivity. It probably triggers microscopic instabilities inside the current sheet, affecting its anomalous resistivity. The frequency of measured magnetic fluctuations is the order of MHz, which is much higher than that of the tearing instabilities [45]. Some correlations between the anomalous resistivity and magnetic fluctuation inside the current

sheet have been observed [46].

2.5.3 Plasmoid

The plasmoid, as a coherent structure of plasma and magnetic fields, possess a measurable magnetic moment, a measurable translational speed, a transverse electric field, and a measurable size. Plasmoids can interact with each other, seemingly by reflecting off one another. Their orbits can also be made to curve toward one another [47]. In recent years, plasmoid research has been conducted by three approaches: astronomical observation, laboratory experiments, and computer simulation.

The CME in the solar flare and mass ejection in the magnetotail are essentially large-scale plasmoids generated and released from the magnetic reconnection as shown in Fig. 2.3 and 2.4. There is tentative observational evidence [48] that the plasmoids might play a key role in the dynamics of magnetic reconnection in the Earth's magnetosphere and in solar flares. Plasmoid formation have also been observed in numerical reconnection studies using other physical descriptions, e.g., fully kinetic simulations [49, 50]. In previous years, plasmoids are less well diagnosed in fusion devices, but results from the TEXTOR tokamak [51] suggest that they might also be present. Recently, there have been some reports about plasmoid in pull mode reconnection such as in MRX experiment.

Recent high-resolution MHD simulations have shown that when the magnetic Reynolds number exceeds 10^4, the current sheet becomes tearing instability and forms a chain of plasmoids [52]. Since currents in the same direction flow in the centers (O points) of the formed plasmoids, they attract each other and grow due to coalescence of the plasmoids with secondary reconnection (Coalescence instability) as shown in Fig. 2.8 - IV. The position of the plasmoid is unstable in the length direction of the current sheet, and after repeated coalescence, it is ejected to the outside of the current sheet (Fig. 2.8 - V) [53, 54]. Since a large amount of energy is released momentarily when such plasmoids are merged and released, this type of reconnection is called transient (Impulsive) reconnection or explosive (Bursty) reconnection [55, 56, 57].

Figure 2.9 (a) shows an example of the plasmoids observed in TS-4 experiment [53]. The formed plasmoid is eventually released downward and absorbed by the magnetic flux in the outflow region via the secondary reconnection. When a large plasmoid is ejected, a temporary increase in the reconnection electric field is observed Simultaneously, as shown in Fig. 2.9 (b) [58]. It is considered that super fast reconnection occurs with the release of plasmoid. Laboratory experiments show that when the acceleration of the magnetic island is at its maximum, the reconnection of the electric field increases most significantly [53]. It is confirmed that the formation and ejection of plasmoids lead to a spike in the reconnection rate both in simulation and in laboratory experiments

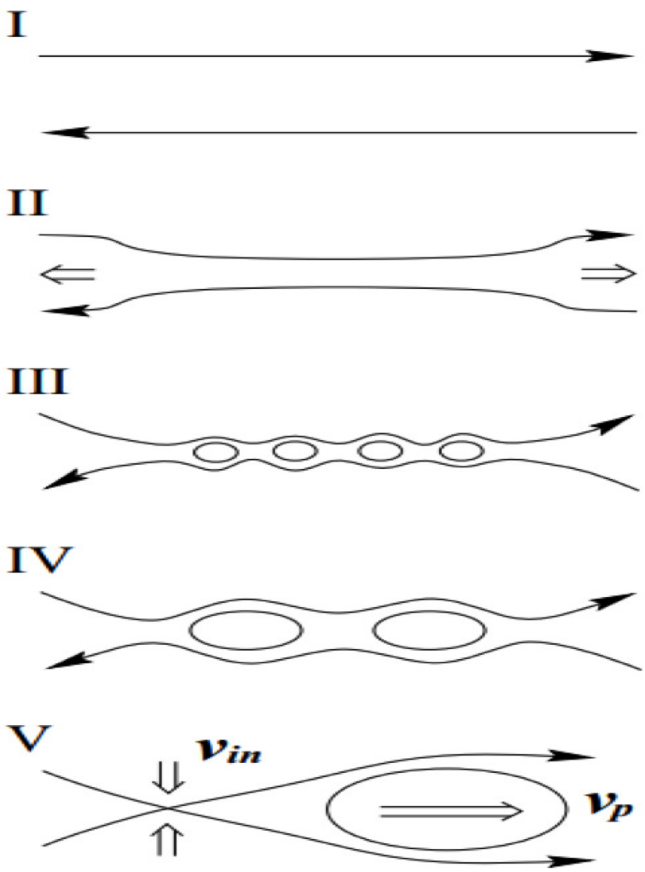

Fig. 2.8 Schematic diagram of plasmoid formation and release in pull mode reconnection.

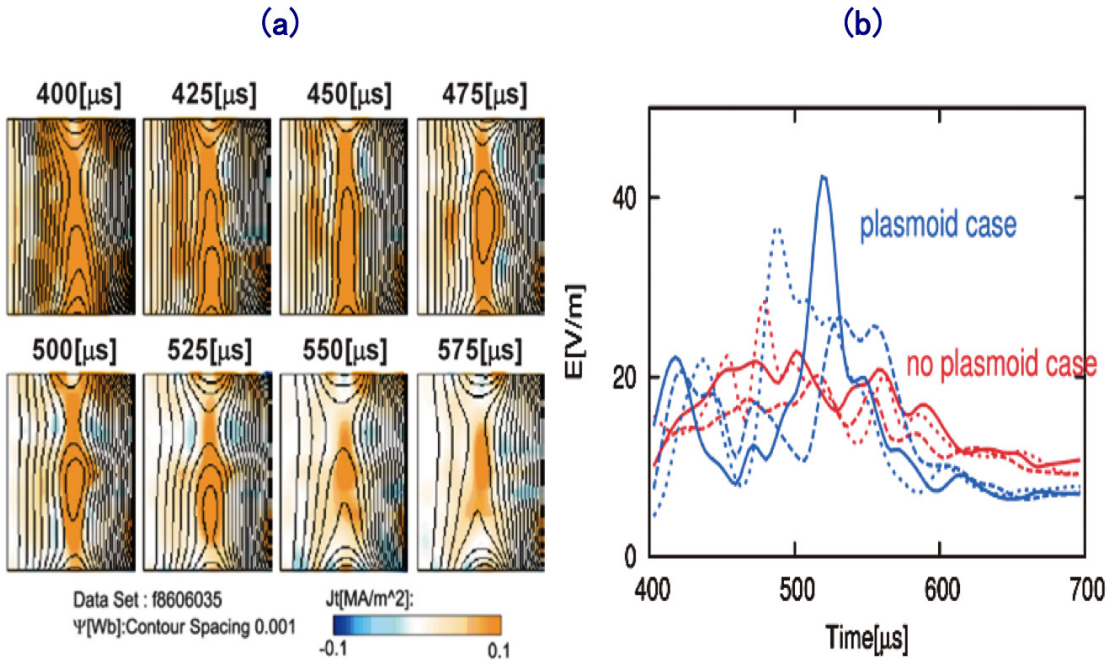

Fig. 2.9 (a) Generation and release of plasmoid appearing in poloidal magnetic surface measurements in the TS-4 experiment. (b) Change of reconnection electric field with and without plasmoid.

[59].

CHAPTER 3

Experimental Setup

3.1 Tokamak Plasma Merging Device TS-6

In this chapter, TS-6 experimental device is briefly introduced. Then, diagnostics used for this dissertation are decribed. Finally, key plasma parameters and details of the experimental regime are presented. As introduced in chapter 1, the experimental device TS-6 is constructed to study axial merging and reconnection of two torus plasmas for heating application of magnetic reconnection, without using the center-solenoid coil (CS). Figure 3.1 is an overview of the appearance of the TS-6 device.

Fig. 3.1 A photograph of the appearance of the TS-6 device.

TS-6 has a cylindrical vessel with an axial length of 144 cm and an inner diameter of 75 cm, and is made of stainless steel to prevent impurities from entering. Compared with the old device TS-3, the glass window of the TS-6 has been significantly increased,

so the measurement range of ion Doppler system, high-speed camera and Thomson scattering system has been expanded.

3.1.1 Coils and Their Charge System

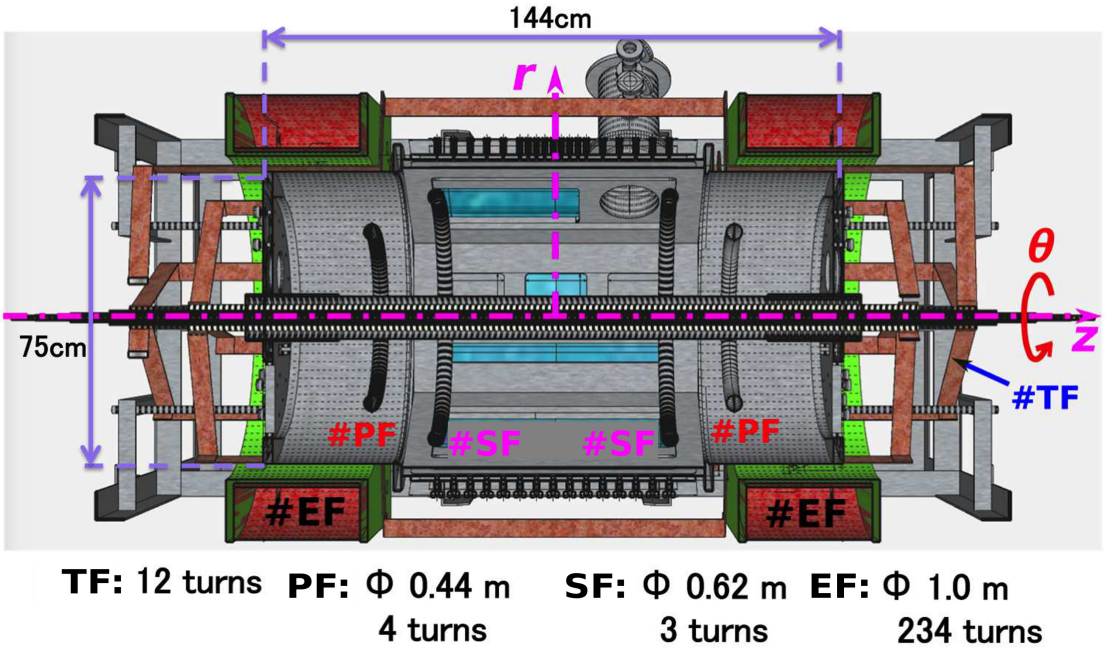

Fig. 3.2 Cross-section of the TS-6 device.

Figure 3.2 shows a cross-section view of the TS-6 device. The main components of the TS-6 system are as follows.

- Poloidal Field coils (PF)
  Inside the chamber, a pair of poloidal magnetic field (PF) coils with a diameter of 44 cm and an axial interval of about 70 cm, are connected to the fast capacitor bank, which has a set of capacitors of 18.75 μF, a rated voltage of 40 kV, and a maximum charging energy of 15 kJ. It takes about 2 minutes and 40 seconds to charge to 39 kV, which is quite fast. The discharge generally starts from 400 μs and the discharge waveform period is about 100 μs.

  The PF coils are used to form two parallel toroidal plasma currents (poloidal magnetic field) of two tokamak plasmas. Thanks to the novel design, the axial distance between the two PF coils can be adjusted in order to generate different types of tokamak. Unfortunately one of the PF coils is broken and is unavailable for a while.

- Separation Coils (SF)
  A pair of separation coils, whose diameters and axial distance are 62 cm and

about 60 cm, respectively, are also located in the chamber. Since the magnetic field generated by them can help the tokamak plasmas separate from the PF coils, they are called SF coils. Due to the damage on one of the PF coils, the SF coils temporarily take place of PF coils and rent their fast capacitor bank.

- TF coils
  The toroidal magnetic field coils (TF) are composed of two parts. One part is located inside the center stack. It contains 12 elongated cylindrical copper plates insulated from each other. The other part surrounds the periphery of the device at equal intervals and connects with the part inside the center stack, forming a set fo TF coils with 12 turns.
  The capacitor bank of the TF coils has a capacitor of 8.3 mF, a rated voltage of 8 kV, and a maximum charging energy of 266 kJ. According to the experimental needs and the withstand voltage capability of the outer insulation layer of the TF coil, the maximum charge is generally 3.6kV. If exceeding 3.6kV, it may damage the insulation layer and cause discharge sparks. The TF coils usually discharge from 50 μs with a discharge period of about 2 ms.

- EF coils (EF)
  Outside the vessel, there is a pair of 234-turn equilibrium field coils (EF) with diameters of 100 cm. The axial interval between them is adjustable within 110 $\sim$150 cm. The EF coils can provide equilibrium field to keep the tokamak from contacting with the wall of the vacuum chamber and maintain them in a stable state. When the EF coils are connected to a DC power source and charged to a maximum current of 150 A, the axial magnetic field ($B_{z,EF}$) generated in the chamber can be considered to be approximately uniform, about18.6 mT.

- CS Coil
  The center solenoid coil (CS) is inserted on the center axis of the center stack. A toroidal current can be induced in the plasma by the induced electromotive force generated by raising the current flowing in the CS coil. The regime of this experiment is to perform a CS-less merging Start-up of ST, so do not use the CS coil.

3.1.2 Vacuum Pumping System and Gas Supply System

- Gas pumping System
  Figure 3.3 (a) shows a schematic diagram of the gas pumping system and supply system in TS-6. The pumping system has one turbo molecular pump (TMP) and three rotary pumps. A high power rotary pump connects to the TMP, and two low power pumps are used for differential pumping when needed.

The internal vacuum degree is measured by a Pirani vacuum gauge and an ionization vacuum gauge. The highest record of vacuum degree is 1.4×10^{-6} Torr, but in the normal experiments it is about $1.8 \sim 2.0 \times 10^{-5}$ Torr.

- Gas Supply System
  The washer gun, consisting of anode and cathode electrodes, is installed in the discharge path. Its washer part is formed by alternately stacked stainless steel washer and insulating washer. While supplying gas, the washer gun can also apply high voltage between the anode and cathode to cause arc discharge and generate plasma. Figure 3.3 (b) shows a photo and a schematic diagram of the washer gun [60].

  The generated plasma is emitted by the Lorentz force of the electric current and magnetic field created by itself in the discharge path [61]. Normally, the washer gun is inserted from both ends in the axial direction of the device, and is installed so as to eject gas near the separation coil. In this experiment, the washer gun is not used for discharge, but only as a pure gas supply channel.

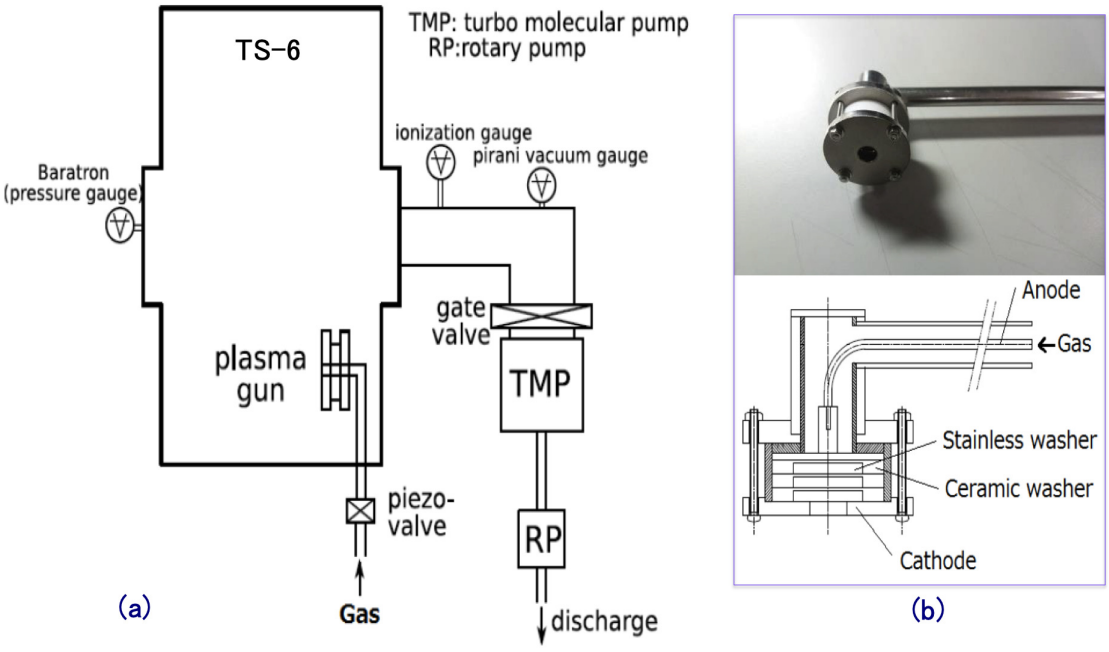

Fig. 3.3 (a) Schematic diagram of the gas pumping system and supply system in TS-6. (b) Schematic diagram and a photo of the washer gun.

3.2 ST Merging Startup Operation

The torus plasma merging device TS-6 can independently generate two torus plasmas at the same time. Two tokamaks with parallel currents attract each other and merge

together in the axial direction, forming a high-beta tokamak through the magnetic reconnection heating that occurs on the contact surface of the two torus tubes. The steps for generating plasma and high-beta ST are shown below.

1. Check the vacuum degree to make sure it is below about 3×10^{-5} Torr. If this value is exceeded, an ideal plasma will not be generated.

2. In order to be able to charge each coil to the preset discharge voltage at the same time, we charge the PF bank first and after waiting for an appropriate time start to charge the TF bank.

3. When PF coils and TF coils are fully charged, Energize the EF coil to apply an equilibrium magnetic field in the chamber in advance. The direction of EF current is opposite to that of plasma current. (about t = 3s)

4. Open the gas valve and inject gas (H, He, Ar). (about t = 2s)

5. The measurement is started at the same time when the discharge trigger on the capacitor bank control panel is started. The acquisition start time of the digitizer for magnetic field measurement is t = 0, as the absolute time from the start of measurement.

6. The capacitor bank for the TF coils starts discharging at t = 50 μs, reaches a peak at about t = 500 μs, and a toroidal magnetic field is applied to the plasma.

7. At t = 400 μs, the capacitor bank for PF coils starts to discharge and generate a poloidal magnetic field, as shown in Fig. 3.4 a [62].

8. A toroidal current is induced in the plasma as the PF current falls, as shown in Fig. 3.4 b.

9. As the polarity of the falling PF current is reversed, the torus plasmas are separated from the PF coils by the repulsive force due to the reversal current, and are pushed toward the mid-plane as shown in Fig. 3.4 c.

10. The two tokamaks pushed out by the PF coils are merged together near the mid-plane through magnetic reconnection heating and form a high-beta ST.

3.3 Plasma Diagnostic Systems

To study the dynamics of the magnetic reconnection in TS-6 experiment, various diagnostics are employed.

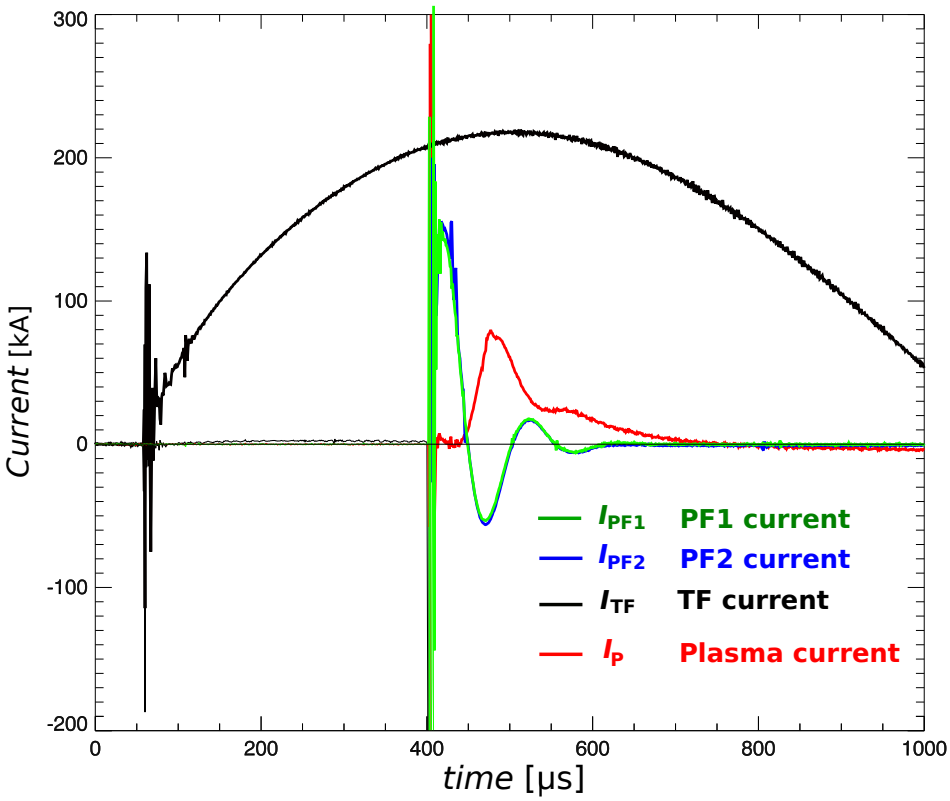

Fig. 3.4 The current waveforms of TF coil, PF coils and the plasma.

3.3.1 Rogowski Coil

A Rogowski coil is a non-contact electrical device for measuring alternating current (AC), and is a safety measurement tool often used to measure large currents. It consists of an annular solenoid, whose wire with the lead from one end returning through the centre of the coil to the other end, so that both terminals are at the same end of the coil. The whole assembly is then wrapped around the straight conductor whose current is to be measured as shown in Fig. 3.5.

When the current which is flowing through the center of the coil changes, the magnetic flux inside the solenoid coil also changes, resulting in an induced electromotive force between the terminals. The current value can then be calculated. When the windings of turns of the coil is N and the cross-sectional area of the coil is S, the magnetic flux passing through the coil is as

$$\Psi = N \oint_l \int_S dS\boldsymbol{B} \cdot d\boldsymbol{l} \tag{3.1}$$

Applying Ampère circuital law, integrate the magnetic field around a annular solenoid to the electric current $I(t)$ passing through the solenoid, we get

$$\Psi = \mu_0 NSI(t) \tag{3.2}$$

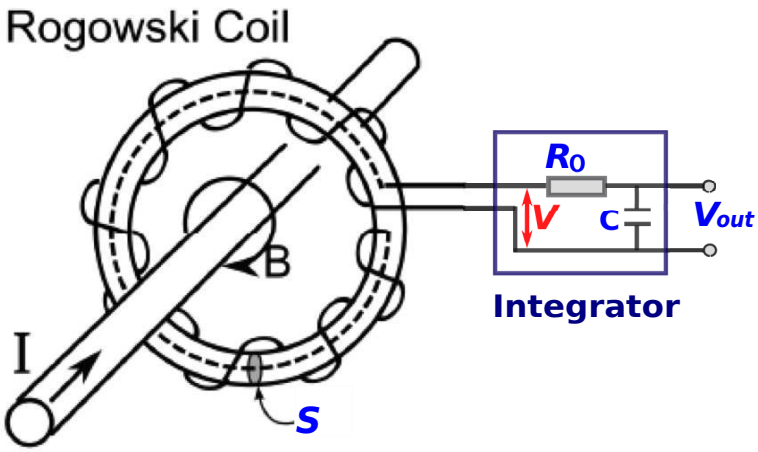

Fig. 3.5 Schematic diagram of rogowski coil circuit.

The induced electromotive force $V(t)$ of the Rogowski coil is

$$V(t) = \frac{d\Psi}{dt} = \mu_0 NS \frac{dI(t)}{dt} \tag{3.3}$$

Assuming an integrator is connected to the output side of the Rogowski coil, the resistance is R_0 and the capacitor is C, the flowing current is denoted as $I'(t)$. We can get

$$\begin{aligned} I'(t) &= \frac{V(t)}{R_0} \\ &= \frac{\mu_0 NS}{R_0} \frac{dI(t)}{dt} \end{aligned} \tag{3.4}$$

The output voltage $V_{out}(t)$ of the integrator is calculated

$$\begin{aligned} V_{out} &= \frac{\int_t I'(t)dt}{C} \\ &= \frac{\mu_0 NS}{R_0 C} I(t) \end{aligned} \tag{3.5}$$

So the AC current that we want to measure is expressed as

$$I(t) = \frac{R_0 C}{\mu_0 NS} V_{out}(t) \tag{3.6}$$

Eq. (3.6) is very convenient.

3.3.2 2D Magnetic Probe System

To study the magnetic reconnection, we design a 2D high-resolution magnetic field probe array, which is installed on the poloidal cross-section ($R-Z$ plane) with B_z and B_t (or B_r) components. The B_z pickup coil is a hollow cylindrical structure, with windings of 300 turns, and its length, inner and outer diameters are 5 mm, 1 mm, 1.9 mm, respectively. The B_t pickup coil is a hollow ellipse structure, with windings of 200 turns, and its width, length, inner and outer diameters are 1.5 mm, 5 mm, 1 mm and 2 mm. They are fixed into the holder printed by the super-high resolution 3D printer (16 μm) which can provide high positional accuracy. In the magnetic reconnection region, the pickup coils are arranged at high density, as shown in the Fig. 3.6.

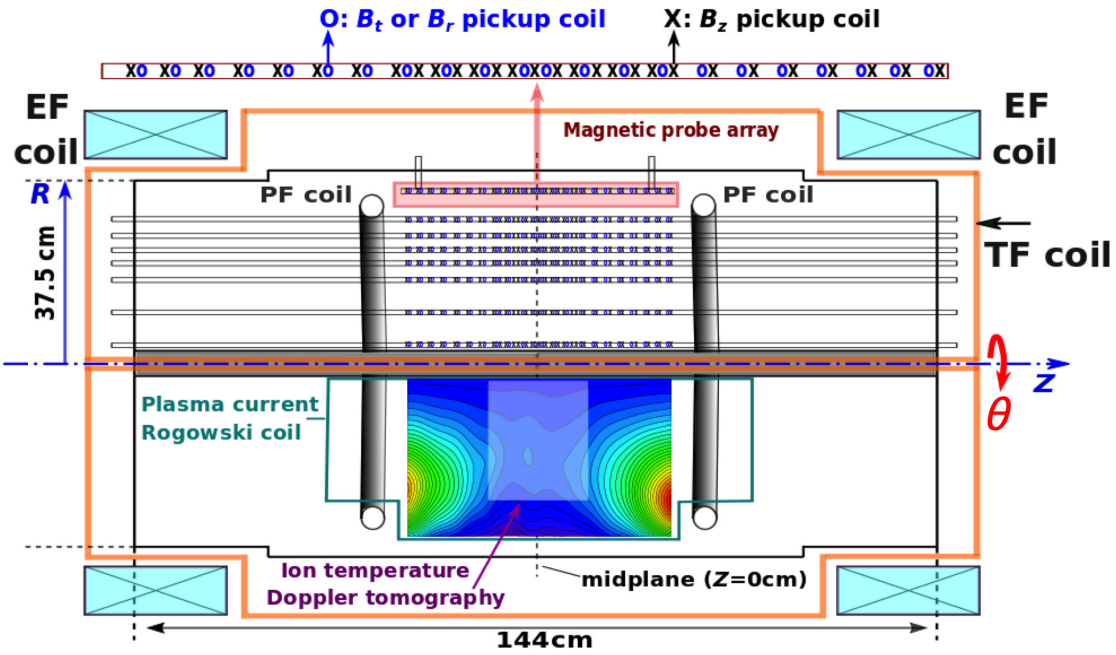

Fig. 3.6 Location of the 2D high-resolution magnetic probe array on cross-section of TS-6 device.

A schematic view of high-resolution 3D printed holder of pickup coils is shown in Fig. 3.7. The indentations can hold B_z pickup coils tightly, and protrusions can fix B_t (or B_r) pickup coils in exact position.

Figure 3.8 shows a table of the location of all the B_z pickup coils, which is used to write the magnetic flux surface.

The measurement principle of the magnetic probe is that the induced electromotive force caused by the time change of the magnetic field passing through the pickup coil outputs an integrated voltage V_{out} through the integrator, and the derivative of the integrated voltage is derived, and the magnetic field B_t at the pickup coil can be obtained. The measurement principle is described below.

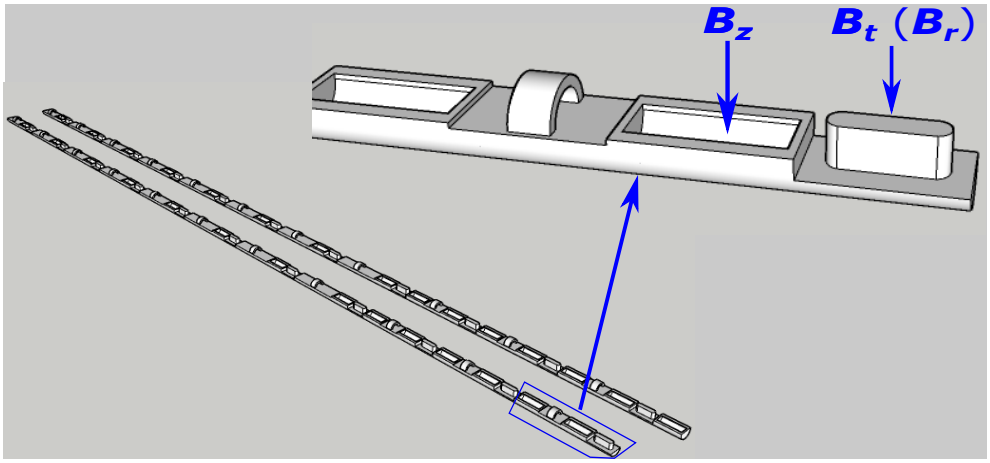

Fig. 3.7 Schematic view of 3D printed pickup coils holder. B_z and B_t (or B_r) pickup coils are fixed by indentations and protrusions, respectively.

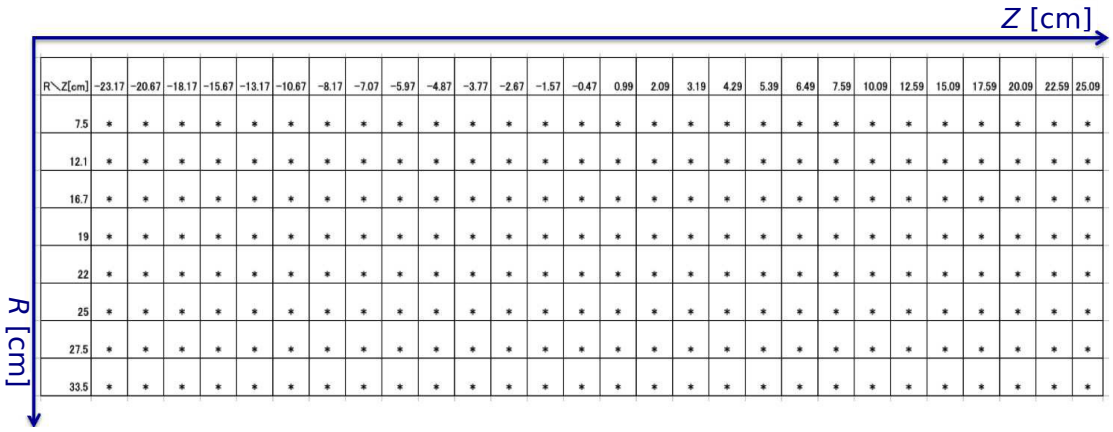

Fig. 3.8 The location of all the B_z pickup coils.

From Faraday' law, the output voltage of the pickup coil is described as

$$V_{coils}(t) = -NS\frac{dB(t)}{dt} \tag{3.7}$$

where NS is called as effective area of the coil: N is the number of turns and S is the area per turn of the coil. $B(t)$ is the magnetic field passing through the pickup coil.

When the integrator is connected to the pickup coil, the subsequent calculation method is the similar to that of the Rogowski coil. But because the output signal of the pickup coil is too small, the integrator needs to be connected to an operational amplifier of non-inverting amplifier type. If the amplification coefficient is denoted as A, we have

$$\begin{aligned} V_{out}(t) &= -\frac{\int_t V_{coil}(t)dt}{RC}A \\ &= -\frac{NSA}{RC}B(t) \end{aligned} \tag{3.8}$$

Hence,

$$B(t) = -\frac{RC}{NSA}V_{out}(t) \tag{3.9}$$

Here, RC is often called the time constant of the integrator. If $RC \gg T$ (T: waveform period of the signal), Eq. (3.8) and Eq. (3.9) are available. In this experiment, the discharge waveform periods of TF coils and PF coils are about 2 ms and 0.1 ms respectively, while RC is about 10 ms.

There is a difference between each coil (NS) and each channel of the signal collector (RC/A), so calibration is required.

- Calibration of NS
  We use Helmholtz coils to create a given magnetic field to calibrate the pickup coils, and get a calibration coefficient $k1$.

- Calibration of $\frac{RC}{A}$
  We use the signal source to output a sine wave with a certain frequency and a certain voltage, to calibrate each channel of the integrator-amplifier-digitizer, and obtain a calibration coefficient $k2$.

The comprehensive coefficient k (= $\frac{RC}{NSA}$) is calculate by $k1$ and $k2$.

The magnetic field $B(t)$ is written as $\boldsymbol{B}$. In the experiment of forming a ST, $\boldsymbol{B}$ usually includes two parts, one is the changing magnetic field $\boldsymbol{B}_{coil}$ measured by the pickup coils, and the other is the constant magnetic field $\boldsymbol{B}_{EF}$ generated by the currents of EF coils. $\boldsymbol{B}$ consists of three spatial components, B_r, B_z and B_t, of which B_t (or B_θ) refers to the toroidal component.

The magnetic field generated by the current of the EF coils is as follows [63].

$$B_{r,EF} = \frac{\mu_0 I}{2\pi}\frac{2z}{r\sqrt{(R+r)^2+z^2}}\left[-K(k)+\frac{R^2+r^2+z^2}{(R-r)^2+z^2}E(k)\right] \tag{3.10}$$

$$B_{t,EF} = 0 \tag{3.11}$$

$$B_{z,EF} = \frac{\mu_0 I}{2\pi}\frac{2z}{\sqrt{(R+r)^2+z^2}}\left[K(k)+\frac{R^2-r^2-z^2}{(R-r)^2+z^2}E(k)\right] \tag{3.12}$$

$$k^2 = \frac{4Rr}{(R+r)^2+z^2} \tag{3.13}$$

Where, I and R are respectively, the current and the radius of the EF coil. r and z are the spatial coordinates. $K(k)$ and $E(k)$ are the complete elliptic integrals of the first and second kind, respectively.

In the following, $\boldsymbol{B}$ represents the total magnetic field, which is the vector sum of $\boldsymbol{B}_{coil}$ and $\boldsymbol{B}_{EF}$. If the EF currents are not used, $\boldsymbol{B}$ is equal to $\boldsymbol{B}_{coil}$. Assuming toroidal symmetry in the TS-6 experiment, the poloidal magnetic flux can be gotten

$$\Psi = \int_{r_0}^{r} 2\pi r B_z dr \tag{3.14}$$

Where r_0 is the radius of the center stack. B_z can be written as

$$B_z = \frac{1}{2\pi r}\frac{\partial \Psi}{\partial r} \tag{3.15}$$

Since $\boldsymbol{\nabla}\cdot\boldsymbol{B}$ = 0, we can get

$$\frac{1}{r}\frac{\partial(rB_r)}{\partial r}+\frac{1}{r}\frac{\partial B_t}{\partial \theta}+\frac{\partial B_z}{\partial z}=0 \tag{3.16}$$

Where B_t is B_θ.
Due to the toroidal symmetry, $\frac{\partial}{\partial\theta}$ = 0, so

$$\frac{1}{r}\frac{\partial(rB_r)}{\partial r} = -\frac{\partial B_z}{\partial z} \tag{3.17}$$

Substituting Eq. (3.15) into Eq. (3.17), we can obtain

$$B_r = -\frac{1}{2\pi r}\frac{\partial \Psi}{\partial z} \tag{3.18}$$

Since $\boldsymbol{\nabla}\times\boldsymbol{B} = \mu_0 J$, we can get

$$\begin{aligned}\boldsymbol{r}\left(\frac{1}{r}\frac{\partial B_z}{\partial\theta}-\frac{\partial B_\theta}{\partial z}\right)+\boldsymbol{\theta}\left(\frac{\partial B_r}{\partial z}-\frac{\partial B_z}{\partial r}\right)+\boldsymbol{z}\left(\frac{1}{r}\frac{\partial(rB_\theta)}{\partial r}-\frac{1}{r}\frac{\partial B_r}{\partial\theta}\right)\\ = \mu_0(\boldsymbol{r}J_r+\boldsymbol{\theta}J_\theta+\boldsymbol{z}J_z)\end{aligned} \tag{3.19}$$

For a given poloidal cross-section, θ is a constant, so $\frac{\partial B_z}{\partial \theta} = 0$, $\frac{\partial B_r}{\partial \theta} = 0$.
Hence, form Eq. (3.19) we can get

$$J_r = -\frac{1}{\mu_0}\frac{\partial B_t}{\partial z} \tag{3.20}$$

$$J_t = \frac{1}{\mu_0}(\frac{\partial B_r}{\partial z} - \frac{\partial B_z}{\partial r}) \tag{3.21}$$

$$J_z = -\frac{1}{\mu_0}\frac{1}{r}\frac{\partial (r B_t)}{\partial r} \tag{3.22}$$

From $\boldsymbol{\nabla} \times \boldsymbol{E} = -\frac{\partial \boldsymbol{B}}{\partial t}$, we can get

$$E_t = -\frac{1}{2\pi R}\frac{\partial \Psi}{\partial t} \tag{3.23}$$

Where E_t is the electric field in toroidal direction.

$$\eta_{eff} = \frac{E_t}{J_t} \tag{3.24}$$

Here, η_{eff} is the effective resistivity of the plasma. Figure 3.9 and Fig. 3.10 show two samples of the poloidal flux contours in a case of vacuum shot and that of a plasma merging shot, respectively.

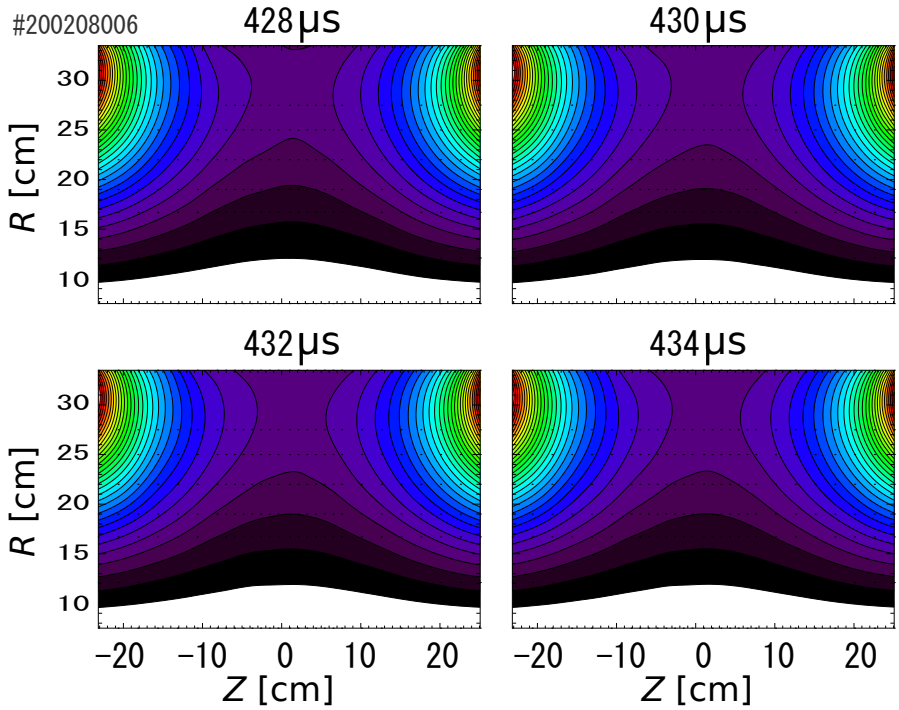

Fig. 3.9 The poloidal magnetic flux contours during vacuum discharge.

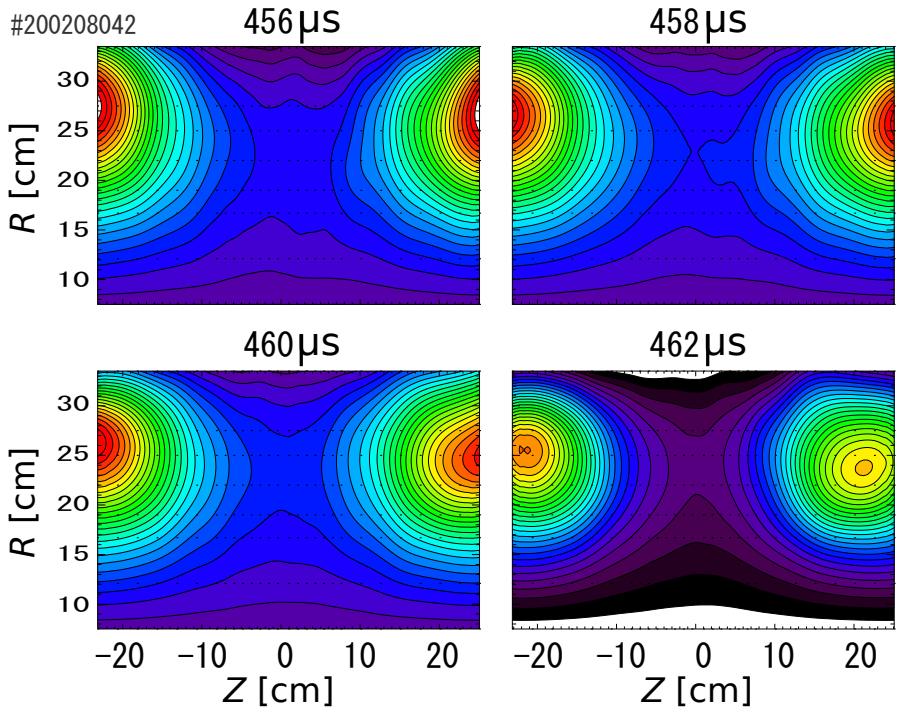

Fig. 3.10 The poloidal magnetic flux contours during two plasma merging.

3.3.3 Doppler Spectroscopy

The spectroscopic measurement is a non-contact measurement for plasma, therefore, this measurement does not affect the plasma. Thanks to this advantage, it can be applied to a high temperature plasma in which the contact diagnostic methods such as magnetic probe and Langmuir prove are not applicable. Now, in fusion plasma research, Doppler spectroscopy of light emission from plasma or impurity [64, 65] ions is a standard technique to measure ion temperature and flow velocity. Its measurement principle will be briefly described below.

- Doppler spectroscopy for ion temperature and flow velocity

When the electron in the excited state transition to a low energy state in the plasma, an electromagnetic wave of a specific wavelength or frequency will be emitted. This electromagnetic wave can be measured as a spectral line. If the ion, as a radiation source of the spectral line, moves with a velocity v, a Doppler shift $\Delta\lambda$ will be caused by the Doppler effect.

Denoting the emitted wavelength as λ_0, observed wavelength as λ, and the speed of light in vacuum is c, we have the Doppler shift:

$$\Delta\lambda = \frac{v}{c}\lambda_0 \tag{3.25}$$

Where $\Delta\lambda$ = λ - λ_0.

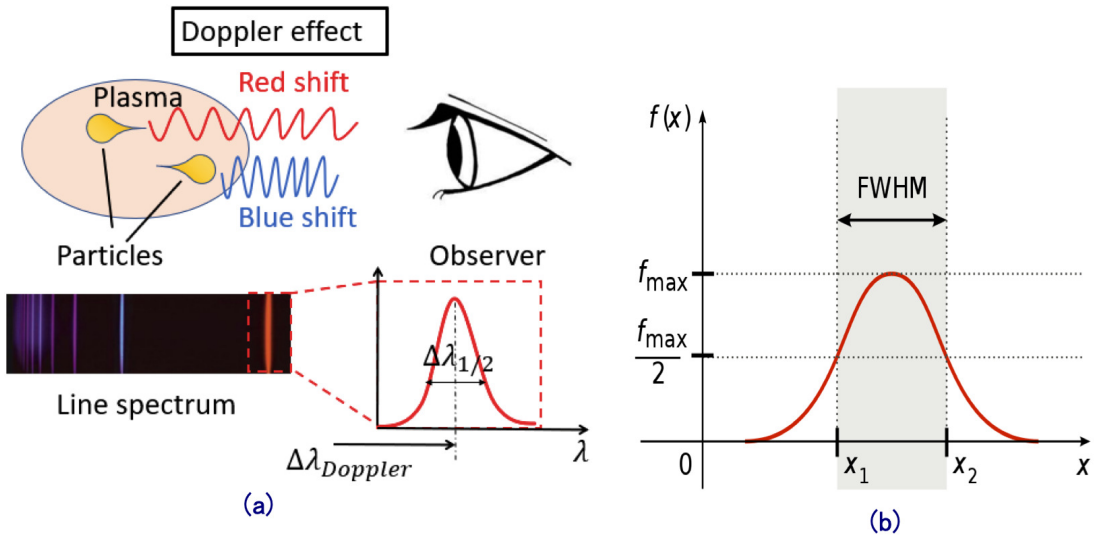

Fig. 3.11 (a) A simplified diagram of the Doppler effect and Maxwellian distribution of spectral lines. (b) Full width at half maximum (FWHM).

Doppler spectroscopy measurement applies this principle to diagnose the collective behavior of ions in plasma. The velocity distribution determined by the thermal and collective motions is considered to be Maxwellian distribution as shown in Fig. 3.11 (a) [62]. A emission line intensity I in Gaussian form is considered to be yielded, as:

$$I(\Delta\lambda) = \frac{I_0}{\sqrt{\pi}\Delta\lambda_D}\exp\left[-(\frac{\Delta\lambda}{\Delta\lambda_D})\right]^2 \tag{3.26}$$

$$\Delta\lambda_D = \frac{\lambda_0}{c}\sqrt{\frac{2k_BT_i}{m_i}} \tag{3.27}$$

Where T_i and m_i are the temperature and mass of the ion, recpectively.

Eq. (3.26) can be fitted by a Gaussian function. T_i can be obtained by comparing with the Maxwell distribution and using the full width at half maximum (FWHM), which is the width of a spectrum curve measured between those points on the y-axis ($f(x)$-axis) which are half the maximum amplitude as shown in Fig. 3.11 (b). Using the FWHM, T_i can be obtained:

$$\Delta\lambda_{FWHM} = 2\sigma\sqrt{2\ln 2} \tag{3.28}$$

$$= 2\sqrt{\ln 2}\Delta\lambda_D \tag{3.29}$$

$$= 7.69\times10^{-5}\lambda_0\left(\frac{T_i}{A}\right)^{\frac{1}{2}}\ [\text{Å}] \tag{3.30}$$

$$T_i = 1.7\times A\times10^8\left(\frac{\Delta\lambda_{FWHM}}{\lambda_0}\right)^2\ [\text{eV}] \tag{3.31}$$

Where A is mass number of the ion. The ion flow velocity V_i is calculated from the peak wavelength of the spectral line λ_{peak} as

$$V_i = \frac{\lambda_{peak} - \lambda_0}{\lambda_0} c \tag{3.32}$$

- Ion Doppler Tomography

Computed tomography (CT) refers to a reconstruction technique that use radiation, visible light, ultrasound, etc., to scan an object, and then uses a computer to process it based on information obtained only from the outside, to create an image of the internal structure of the object. X-ray CT, which is often used in the medical field, is already widely known. At recent years, CT technology has been used in the diagnostic of nuclear fusion plasma, especially in the reconstruction of ion temperature distribution. Because this method often uses the Doppler effect in the analysis, it is called tomographic ion Doppler spectroscopy or ion Doppler tomography [66, 67].

In plasma measurement, applying the principle of CT, the physical quantity in the plasma cross-section is reconstructed based on the information of the emission intensity that integrates the emitted light on the line of sight. The principle of CT is expressed by the following equation, taking X-ray CT as an example.

It is assumed that $g(r)$ function denotes the X-ray absorptance distribution on a cross-section of an object. When X-rays are incident along the straight line L on the cross-section, there is

$$I = I_0 \exp\left[-\int_L g(r) dl\right] \tag{3.33}$$

Where I_0 and I are respectively, the incident intensity and the intensity of X-rays emitted from the opposite side. If $f_L = \ln\left(\frac{I_0}{I}\right)$ is set, we have

$$f_L = -\int_L g(r) dl \tag{3.34}$$

The absorption rate measured by the measuring instrument is defined by the integral form of the small displacement dl along the line of sight L. This cannot be solved independently, but if the integral values of multiple lines of sight are obtained by measurements, the local distribution $g(r)$ can be obtained by the inverse transformation of the above equation.

There are some analytical methods of reconstruction, such as Abel transform method, Colmac method, Fourier-Bessel method and so on. In this study, we adopt the reconstruction method of Abel transform which assumes the axial symmetry of the measured object.

As shown in Fig. 3.12 [62], if the local distribution is described as $I(r)$, the integrated value of the emission intensity is denoted as $f(y)$, which is obtained from the line

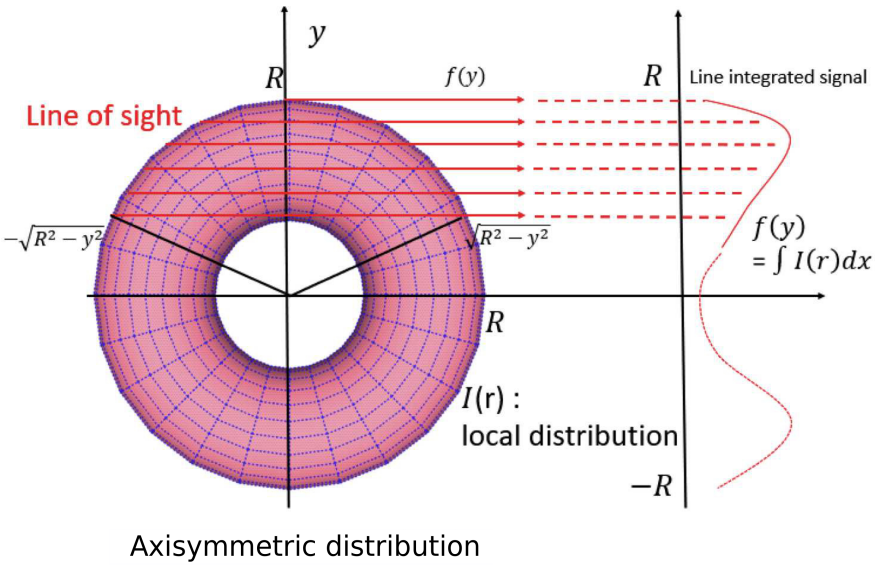

Fig. 3.12 Axisymmetric local structure $I(r)$ and its line-of-sight integral $f(y)$.

of sight of Y = y on the X-Y plane. The line-of-sight integration interval of the axisymmetric distribution, depending on R and the line-of-sight position y, can be represented by $[-\sqrt{R^2-y^2}, \sqrt{R^2-y^2}]$.

$$f(y) = \int_{-\sqrt{R^2-y^2}}^{\sqrt{R^2-y^2}} I(r)dx \tag{3.35}$$

$$= 2\int_y^R \frac{I(r)rdr}{\sqrt{r^2-y^2}} \tag{3.36}$$

Using the inversion formula, we have

$$I_r = -\frac{1}{\pi}\int_r^R \frac{df(y)}{dy}\frac{dy}{\sqrt{y^2-r^2}} \tag{3.37}$$

Using equation Eq. (3.37), the local distribution $I(r)$ can be obtained from the measured value $f(y)$ (line-of-sight integrated value). In addition, using a spectroscope to divide the measurement signals into signals of each wavelength and performing Abel transform, the local emission intensity distribution of the wavelength at each point can be obtained. Ion temperature and flow velocity can be measured using Eq. (3.31) and Eq. (3.32).

3.3.4 Langmuir Probe

A Langmuir probe, also called electrostatic probe, is a device used to measure the electron temperature, electron density, and electric potential of a plasma. It works by inserting one or more electrodes into a plasma, with a constant or time-varying electric

potential between the various electrodes or between them and the surrounding vessel. The measured currents and potentials in this system allow the determination of the physical properties of the plasma.

The triple probe used in this study, can measure the instantaneous values of electron density and electron temperature, its schematic circuit is shown in Fig. 3.13. Three adjacent probes P_1, P_2, and P_3 are used simultaneously, and bias voltage V_{d2} is applied between P_1 and P_2, and V_{d3} is applied between P_1 and P_3. The electric potentials of P_1, P_2 and P_3 are set to V_1, V_2 and V_3, respectively, the floating potential is sandwiched between them as shown in Fig. 3.13 (b). As bias voltage shown in Fig. 3.13 (a), the potential of P_1 is the highest, P_1 flows electron current I_1, P_2 and P_3 flow ion currents I_2 and I_3, the relationship among them is $I_1 = I_2 + I_3$. Assuming the electron velocity is Maxwell distribution, probe currents are given as,

$$-I_1 = -I_e(V_1) + I_i(V_1) = I_{e0}e^{-\phi_1} + I_i(V_1) \tag{3.38}$$

$$I_2 = -I_e(V_2) + I_i(V_2) = I_{e0}e^{-\phi_2} + I_i(V_2) \tag{3.39}$$

$$I_3 = -I_e(V_3) + I_i(V_3) = I_{e0}e^{-\phi_3} + I_i(V_3) \tag{3.40}$$

Where I_{e0} is thermal diffusion current, being described as

$$I_{e0} = \frac{1}{4}Sn_e e\sqrt{\frac{8k_BT_e}{\pi m_e}} \tag{3.41}$$

$$\phi_{1,2,3} = \frac{eV_{1,2,3}}{k_BT_e} \tag{3.42}$$

Where S is the area of cross-section of the probe, T_e is the electron temperature.

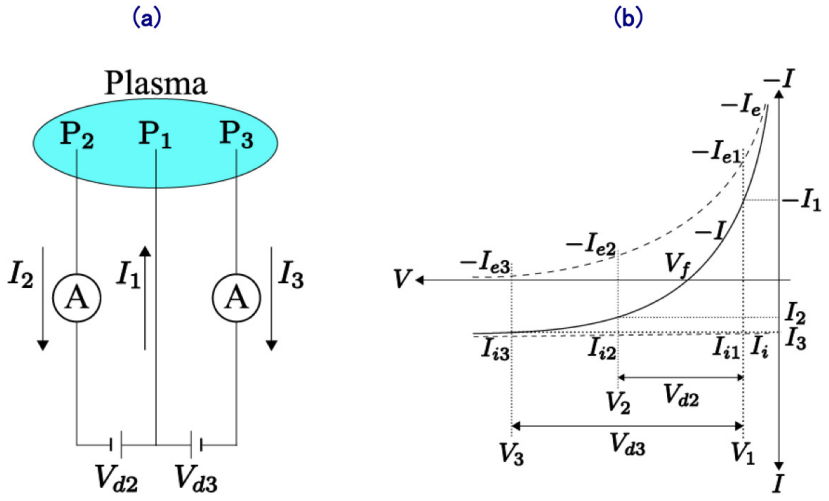

Fig. 3.13 (a) Schematic view and (b) I - V characteristics of triple langmuir probe.

Assuming that the ion current is almost constant, i.e. $I_i(V_1) \approx I_i(V_3) \approx I_i(V_3) = I_i$, eliminating I_i in formula Eq. (3.38) - Eq. (3.40) gives:

$$\frac{I_1 + I_2}{I_1 + I_3} = \frac{1 - e^{\phi_2}}{1 - e^{\phi_3}} \tag{3.43}$$

Due to the current values I_1, I_1 and I_1 as measured values, are the known conditions, from Eq. (3.42) and Eq. (3.43), we can get

$$I_i = \frac{I_3 - I_2 e^{\phi_{\Delta V}}}{1 - e^{\phi_{\Delta V}}} \tag{3.44}$$

Where

$$\phi_{\Delta V} = \frac{e(V_3 - V_2)}{k_B T_e} \tag{3.45}$$

If the electron temperature T_e is obtained, the ion current I_i can be uniquely solved. If the ion saturation current I_i^{sat} is assumed to be equal to I_i, there is

$$I_i^{sat} = \exp\left(-\frac{1}{2}\right) e n_e S \sqrt{\frac{k_B T_e}{m_i}} \tag{3.46}$$

n_e can be solved from Eq. (3.46) [68].

CHAPTER 4

Dynamics of Plasmoid with Parallel Plasma Current in Early Reconnection Phase of Two Merging Tokamak Plasmas

As introduced in chapter 3, TS-6 device is constructed to produce a high-beta spherical tokamak (ST) by axially merging two tokamak plasmas. In this dissertation, push-mode magnetic reconnection experiments is studied.

Locations of high-resolution pickup coils are shown in Figure 3.6, of which B_z pickup coils is aimed to measure magnetic field and write magnetic flux surface in detail are described in a table shown in Figure 3.8. The measured signal is the output voltage of the amplifier, i.e. the V_{out} of Eq. (3.9), we calculate axial magnetic field B_z of the pickup coil by Eq. (3.9).

Figure 4.1 (a) shows an evolution of PF1/2 coil currents, TF current, and plasma current. Its enlarged view is shown in Fig. 4.1 (b), only taking PF1 and plasma current as an example. Black line describes TF current, blue and green lines show PF1/2 currents, and red line represents the plasma current. These currents are all measured through the Rogowski coils outside the device, so they only represent the current though one turn of each coil. Since the turns of the TF coils and PF 1/2 coils are 12 and 3, respectively, their total equivalent currents should be multiplied by their respective turns with the currents shown in Fig. 4.1. As described in section "ST Merging Startup Operation" of chapter 3, plasma is produced during the phase I. When the currents of PF coils reverse their direction (phase II), a repulsive force will be generated between them and their adjacent tokamak plasma. These repulsive forces will push the two tokamaks toward the midplane, where magnetic reconnection occurs. We performed experiments through hydrogen and argon (Ar) discharge.

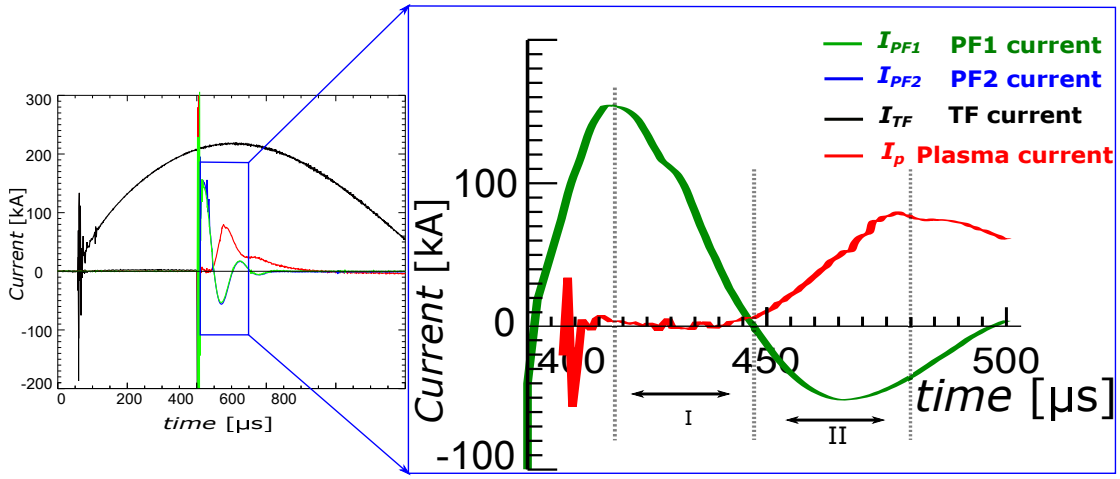

Fig. 4.1 (a) Evolution of the currents of TF coil, PF coils and plasma. (b) The enlarged view of (a), taking PF1 and plasma currents as examples. Black line: TF; Blue and green lines: PF 1 and 2; Red line: plasma.

4.1 Spontaneous Formation of Plasmoid during the Early Phase of Reconenction

In the experiment of hydrogen discharge, the PF coils and TF Coil are respectively charged up to 39 kV and 3.4 kV, and the DC current of EF coil is 150 A. During ramp-up phase of the plasma current, the merging of the two STs takes place within about 35 μs (445 $\sim$ 480 μs). We divide the merging phase into two parts, one is early reconnection phase (Phase I) with smaller plasma current, and the other is main reconnection phase (phase II) with larger plasma current, as shown in Fig. 4.3 (a). Figure 4.2 (a) shows the evolution of the two-dimensional profile of the poloidal magnetic flux in the early reconnection phase, which is measured by the new 2D high-resolution magnetic probe array. A plasmoid (closed magnetic flux surface) is clearly observed near the midplane on the poloidal cross-section of two merging tokamak plasmas.

The PF currents reverse their polarity at about 447 μs, then tokamak plasma currents start to be antiparallel to the PF currents, causing the two tokamak plasmas separate from the PF coils. During the Phase I, although two STs have been separated from the PF coil currents and are pushed to merge together, they are still far apart. Due to the long distance between the two STs, the curvature of the magnetic field lines of the tokamak near the midplane is poor, the instability occurs. As a result, a part of peripheral plasma is detached from the main tokamak plasma, forming a plasmoid (or called magnetic island) and a new X-point. This is the first observation of plasmoid formation in the early magnetic reconnection phase of the two merging tokamak plasmas.

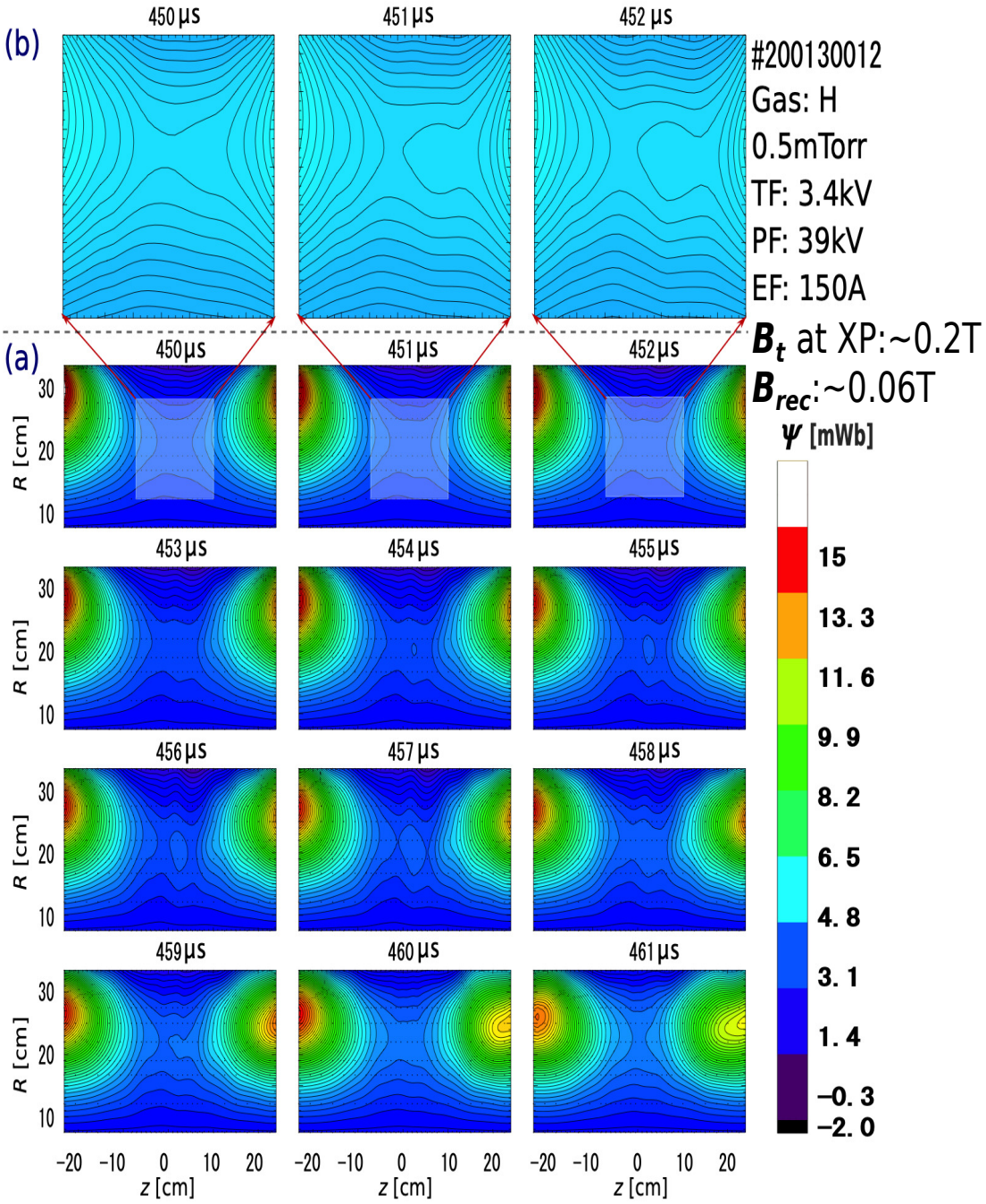

Fig. 4.2 Evolution of the contour of the poloidal magnetic flux. A plasmoid is formed, when a part of peripheral plasma approaching the mid-plane is detached from the tokamak plasma. At the same time, two X-points are formed. Guide field B_g is about 0.15 T, B_t at X-point is about 0.2 T, and the reconnection field is about 0.06 T.

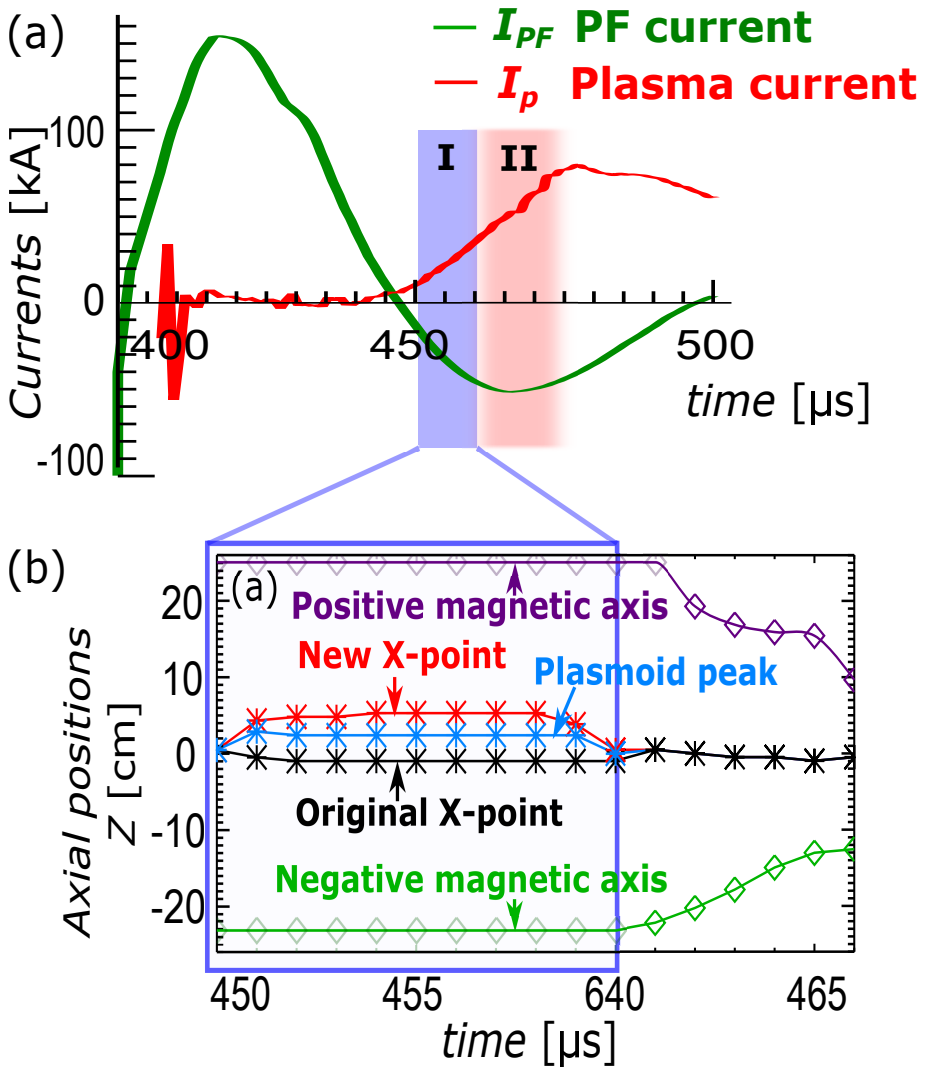

Fig. 4.3 (a) The waveforms of PF and plasma currents and two reconnection phases. Phase I and phase II are denoted as the early (or initial) reconnection phase and the main reconnection phase. (b) axial positions of magnetic axes of two STs, X-points and plasmoid peak.

4.2 Analysis of Plasmoid Formation

4.2.1 Occurrence of Pull-mode Reconnection in Push-mode Reconnection Experiment

Figure 4.4 (a) shows the evolution view of the reconnected flux (common flux), and (b) and (c) are the enlarged views of two periods 437 $\sim$ 454 μs and 454 $\sim$ 460 μs. Obviously, 443 μs is a turning point. What is happened before and after 443 μs? Figure 4.5 (a) shows the evolution of the radial maximum of private magnetic flux along Z axis during 441 $\sim$ 444 μs. In the private-to-common reconnection (Pattern I), common flux increase when the reconnection proceeds, while it is opposite in the common-to-private

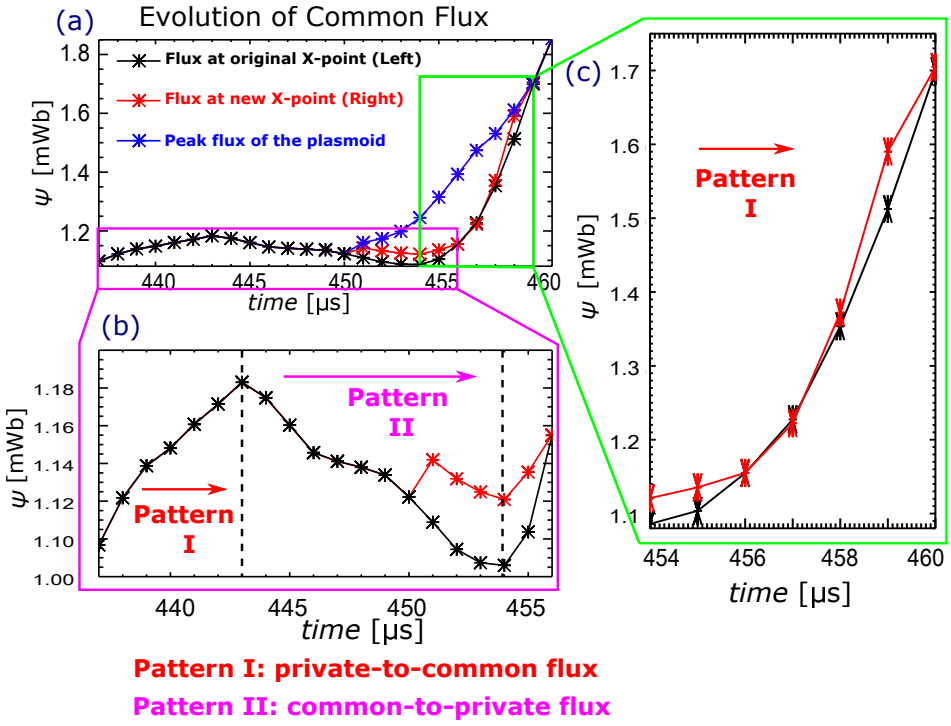

Fig. 4.4 (a) Evolution of the common flux. Black line and red line show the common flux at original X-point (left) and new X-point (right) after the plasmoid is formed. Blue line show the peak magnetic flux of the plasmoid. (b) and (c) are the enlarged view of the two periods 437 $\sim$ 456 μs and 454 $\sim$ 460 μs.

reconnection.

Figure 4.4 (b) and Fig. 4.5 (a) indicate that the magnetic reconnection before 443 μs is the typical private-to-common reconnection of the merging-type experiment. But after about 443 μs, the plasma current is formed shown in Fig. 4.3 (a), then the PF currents decrease to 0 and reverse their direction soon. It is considered that the reconnection change from the private-to-common pattern to the common-to-private pattern locally and temporally, the transition process of which is shown in Fig. 4.5 (b).

4.2.2 Plasmoid Formation Process

The Pattern II reconnection continues until 454 μs, and plasmoid is formed from 451 μs, as shown in Fig. 4.4 (b). A detailed precess of how the plasmoid is formed, grows, and is absorbed corresponding to formation process, pileup process and absorption process, is shown in Fig. 4.6,

At 450 μs, the private flux generated by the Pattern II magnetic reconnection, which has been attached to the right tokamak and has not been completely flowed into it yet, has bad curvature and is compressed into almost antiparallel lines by the upper and lower inflows. At 451 μs, due to the instability of the magnetic field lines with bad curvature, a plasmoid is spontaneously formed and accompanied by a new X-point for-

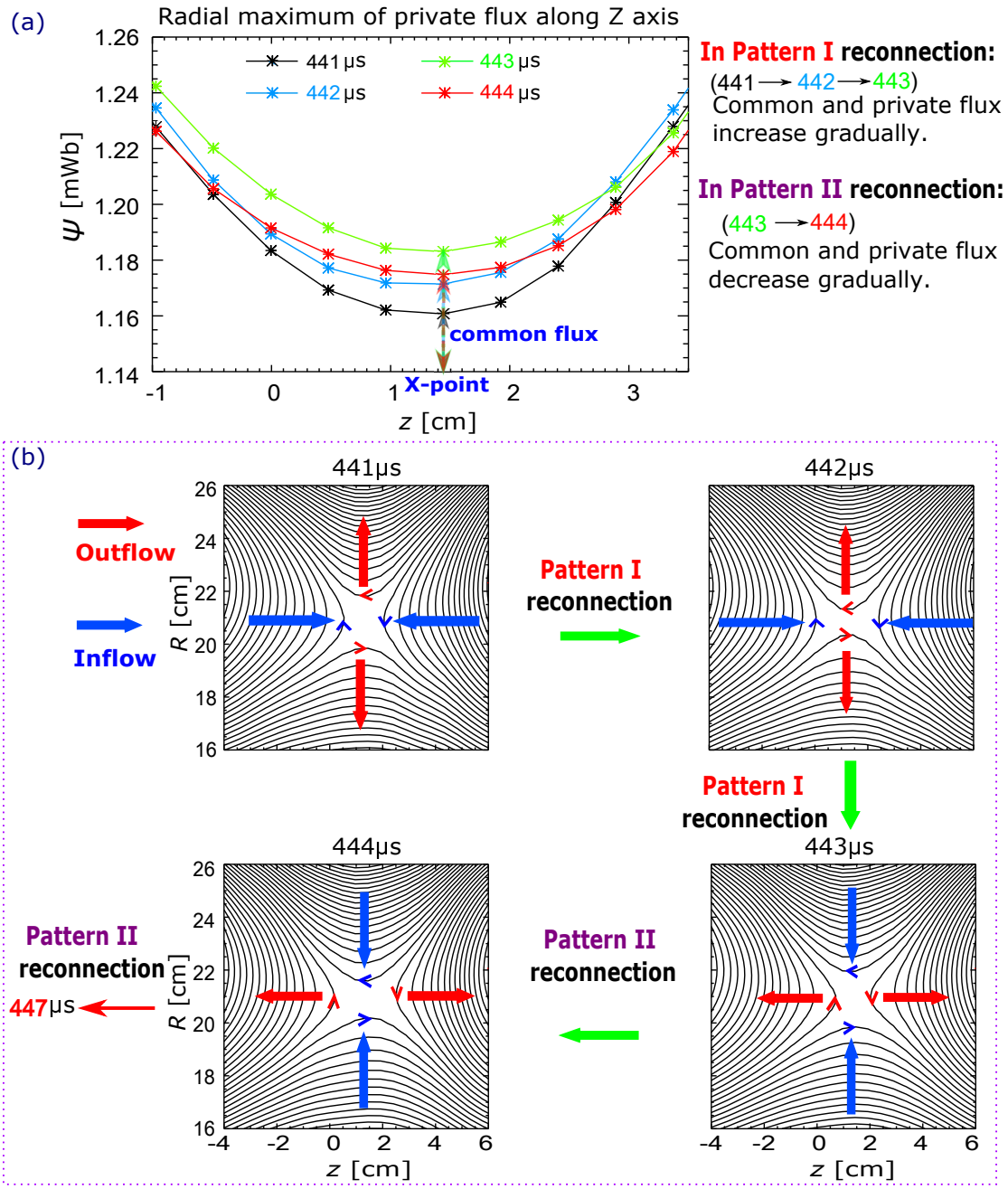

Fig. 4.5 (a) Evolution of the radial maximum of private magnetic flux along Z axis during $441 \sim 444$ μs. When the reconnection changes from private-to-common pattern to common-to-private pattern, the evolution of common and private flux change accordingly. (b) The transition process from private-to-common patterne to common-to-private pattern during 441 μs ~ 444 μs. Blue and red arrows represent the inflow and outflow, respectively. Red '+' shows the position of radial maximum of the poloidal magnetic flux.

mation on the right side. At the same time, the Pattern II reconnection at the original X-point (left) continues. During the formation process, the plasmoid grows gradually because the plasma of the merging tokamak on the right side is transported to the plasmoid along the magnetic field lines and piles up in it. The plasmoid grows in both the size and the magnetic flux until 454 μs.

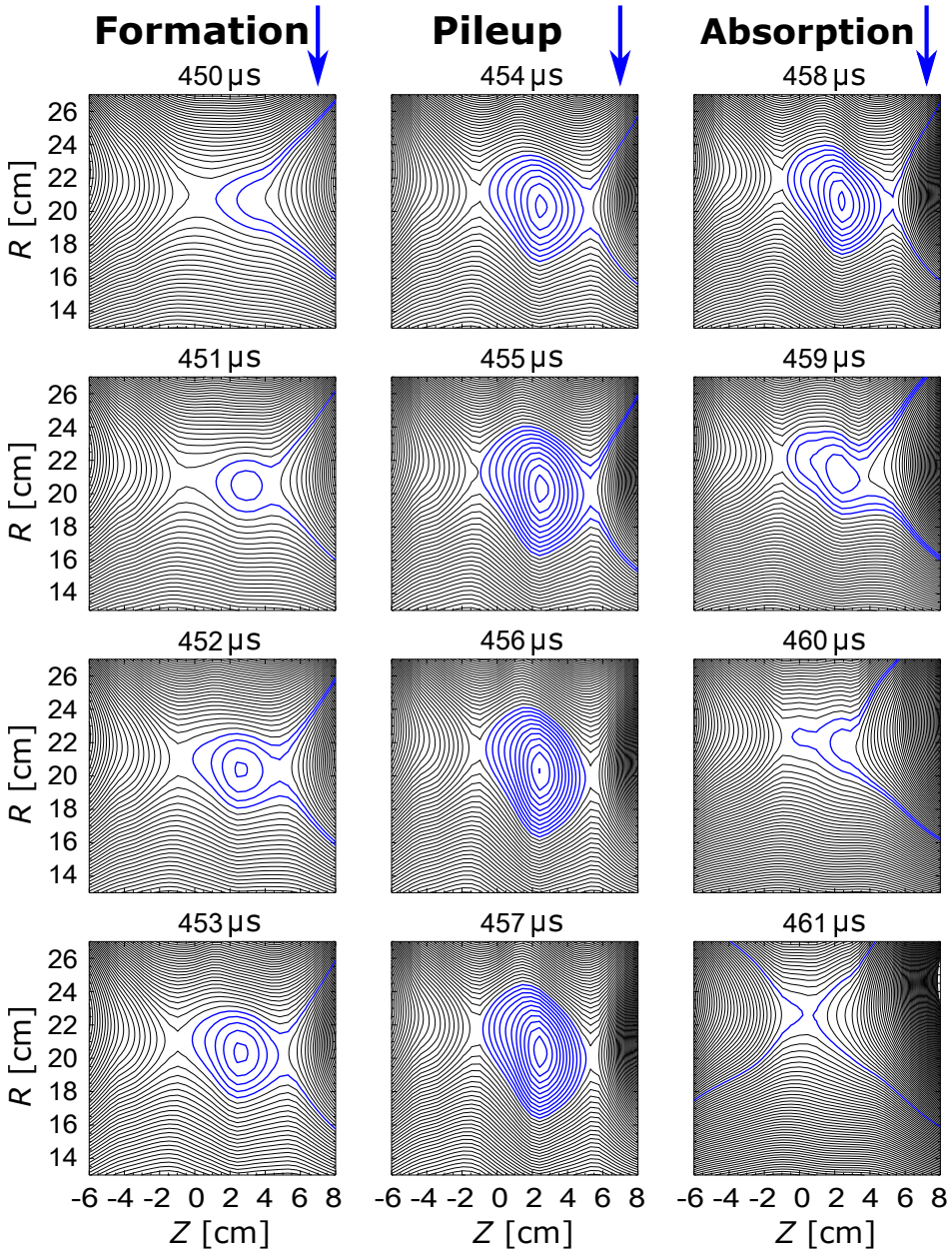

Fig. 4.6 Formation and growth process of the plasmoid. The axial size of the plasmoid peaks at 454 μs, then as the plasmoid grows, the plasma piles up in it, while keeping the axial scale unchanged. The magnetic flux of the plasmoid peaks at about 456 μs.

As shown in Fig. 4.4 (b), the common flux become to increase from 454 μs , which indicates that the Pattern I reconnection starts again. From 454 μs to 455 μs, the common flux at left X-point increases faster than at the right side, which suggests that the

plasmoid starts to merge with the left tokamak in pattern I reconnection and the right side is still in Pattern II reconnection. The similar process continues until 456 μs. At 456 μs, when the common fluxes of the two X-points are the same, the size and magnetic flux of the plasmoid reach the peak values, the magnetic energy stored inside the plasmoid also peaks. Then the plasmoid begins to merge with the two tokamaks simultaneously. The similar process continues until the plasmoid is completely absorbed to the two tokamaks at 460 μs, then the typical Pattern I reconnection starts again. The above results show that the formation and growth of the plasmoid is due to a temporal common-to-private pattern reconnection, while the absorption of it is caused by the typical private-to-common pattern reconnection.

4.3 Plasmoid with Parallel Plasma Current

Figure 4.7 shows the evolution of the toroidal current density J_t and poloidal magnetic flux. Lines represent magnetic flux, color shows the current density. It is can be seen that the plasmoid current is parallel to the tokamak plasma currents.

Why is the plasmoid current parallel to the plasma current? As shown in Fig. 4.3 (b), during the plasmoid formation, the two merging tokamaks are still far apart, and their magnetic field lines intersect at an angle greater than 90^o, as shown in Fig. 4.8. Therefore, the polarity of the current around X-point remains unchanged and is parallel to the tokamak plasma currents.

4.4 Characteristics of the Sheet Currents

After the plasmoid is formed, as the plasmoid grows, the intersection angles between the magnetic field lines of the plasmoid and the two tokamaks are less than 90^o. Therefore, the polarities of the current near the two X-points change and are antiparallel to the tokamak plasma current, whose schematic diagram takes 456 μs as an example shown in Fig. 4.9.

Figure 4.10 shows an enlarged view of the plasmoid and current sheets. During the formation of the plasmoid, two current sheets are also induced around two X-points, and the right one between the plasmoid and its parent tokamak plasma is dominant. As the plasmoid grows, upstream plasma inflows also pile up in the current sheets as shown in Fig. 4.11. During this process, the current sheet is compressed by the enlarging attraction force between the plasmoid and the tokamak. When the plasmoid reaches its peak, the current sheets are also compressed the most, i.e. they peak at the same time at 457 μs. When the plasmoid merges with the two major tokamak plasmas simultaneously, the current sheets become weak rapidly.

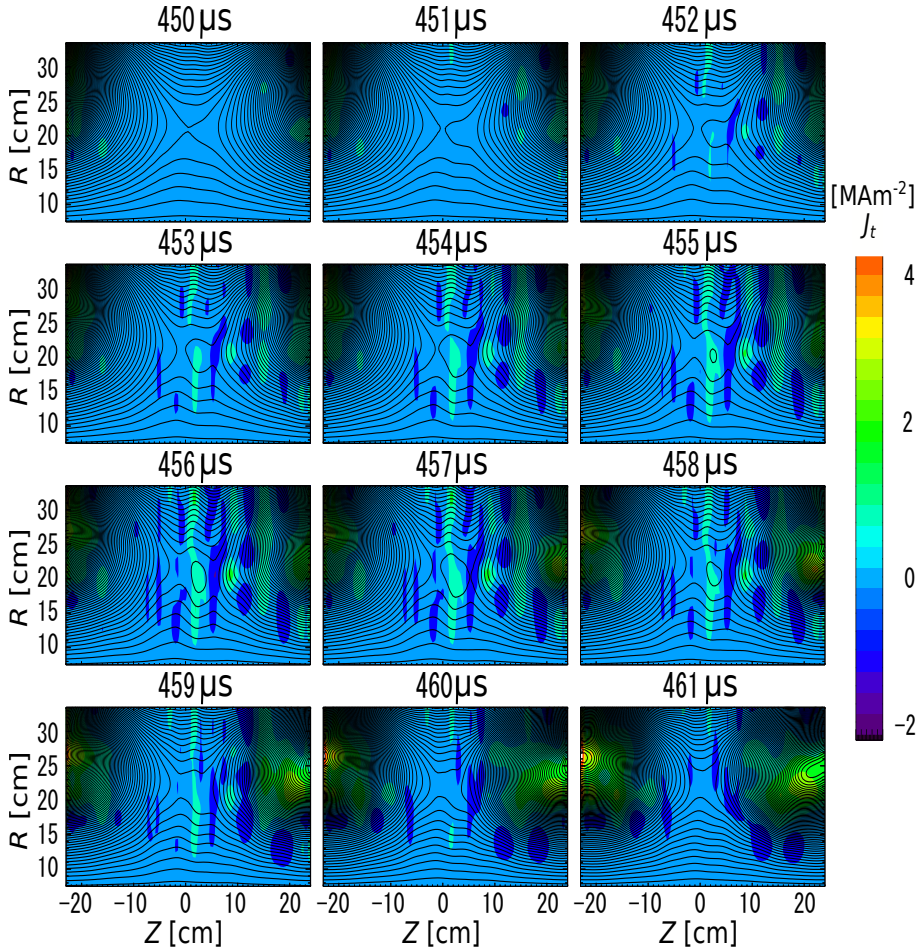

Fig. 4.7 Evolution of the poloidal magnetic flux and toroidal current density J_t. Lines represent magnetic flux, color shows the current density. The color shows clearly that the toroidal plasmoid current is parallel to the tokamak plasma currents.

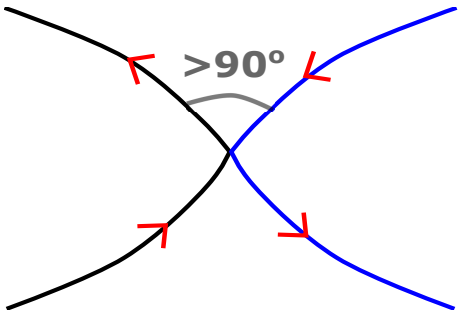

Fig. 4.8 Schematic view of the angle at which the magnetic field lines intersect being greater than 90^o.

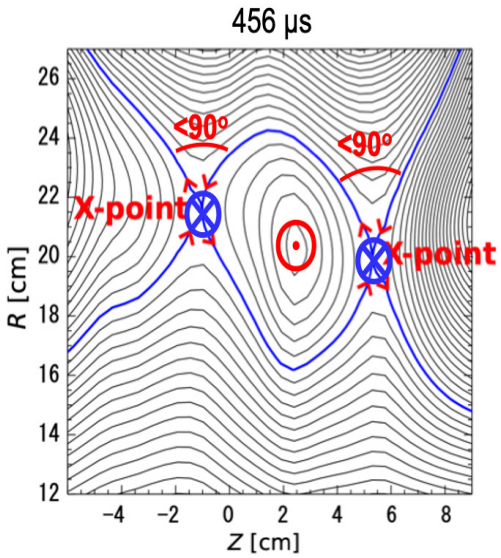

Fig. 4.9 Schematic view of the polarity change of the sheet current.

4.5 Effect of Plasmoid Absorption on Common Flux Ratio

The toroidal electric field E_t at X-point called reconnection electric field is used to describe the reconnection speed. On the other hand, the common flux ratio (also called reconnected flux ration) is defined as

$$\alpha = \frac{\Psi_{com}}{\min(\Psi_{peak1}, \Psi_{peak2})} \tag{4.1}$$

Where the Ψ_{com} represents the reconnected magnetic flux, and is also called common flux. The $\min(\Psi_{peak1}, \Psi_{peak2})$ indicates the smaller of the poloidal magnetic fluxes at the two magnetic axes of the merging tokamaks, as shown in Fig. 4.12. During the merging of two ST plasmas, the common flux gradually increases through magnetic reconnection and finally reaches the same value as the $\min(\Psi_{peak1}, \Psi_{peak2})$, indicating the end of the merging process. So the common flux ratio is also used to evaluate whether the magnetic reconnection is fast or slow.

Figure 4.13 (a) shows the evolution of plasmoid size defined as the axial interval between two X-points. Figure 4.13 (b) shows the evolution of the grown magnetic flux of the plasmoid, i.e. the plasmoid peak flux relative to the common flux. we observed that the evolution of the plasmoid effects the reconnection speed and the common flux ratio, as shown in Fig. 4.13 (d - e). However, during the early reconnection phase of ($450 \sim 461$ μs), due to the constraint of the magnetic field measurement, although the axial positions of magnetic axes are unable to traced exactly ,the velocities of them and the common flux ratio are also unable to be calculated, the reconnection speed E_t can be accurately calculated. During the plasmoid formation process, the magnetic

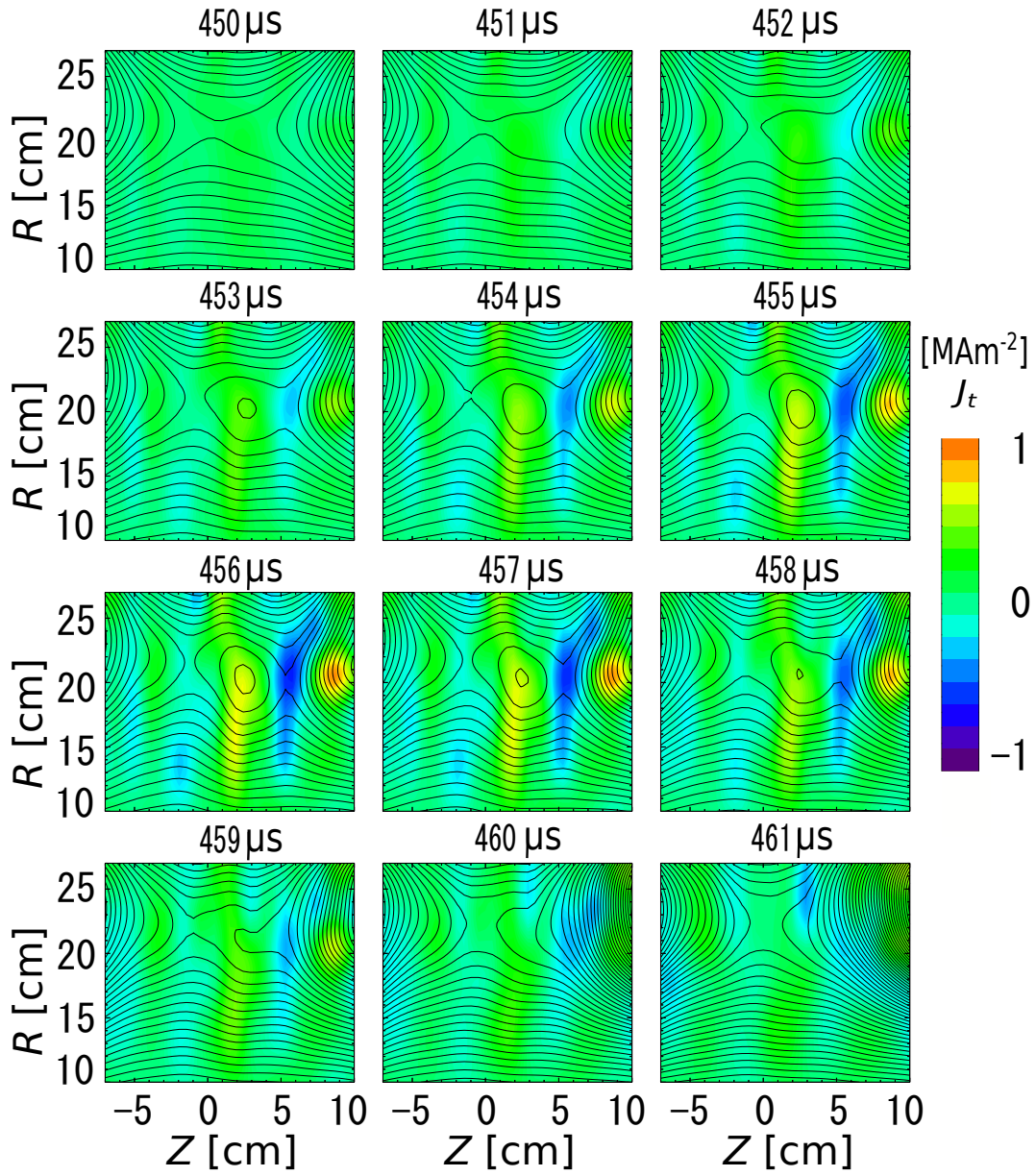

Fig. 4.10 Enlarged view of evolution process of the plasmoid and current sheets. The plasmoid and current sheets peak at the same time (457 μs).

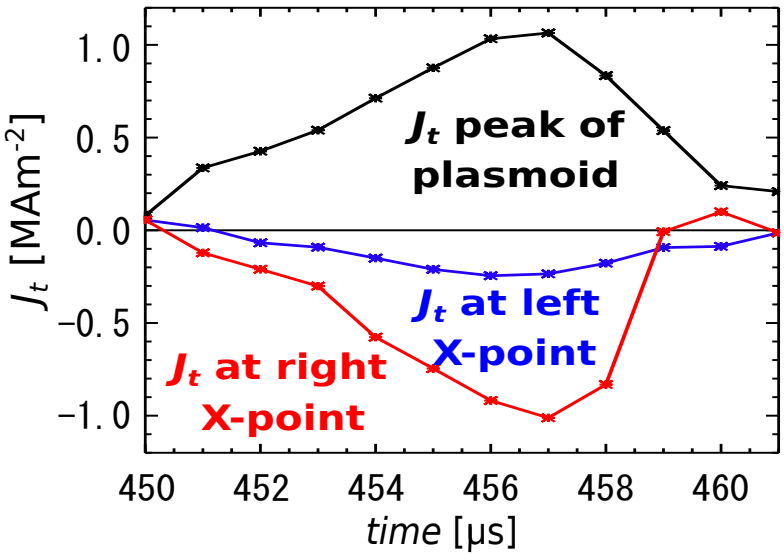

Fig. 4.11 The evolution of the plasmoid and sheet currents at two X-points. They peak at the same time at 457 μs.

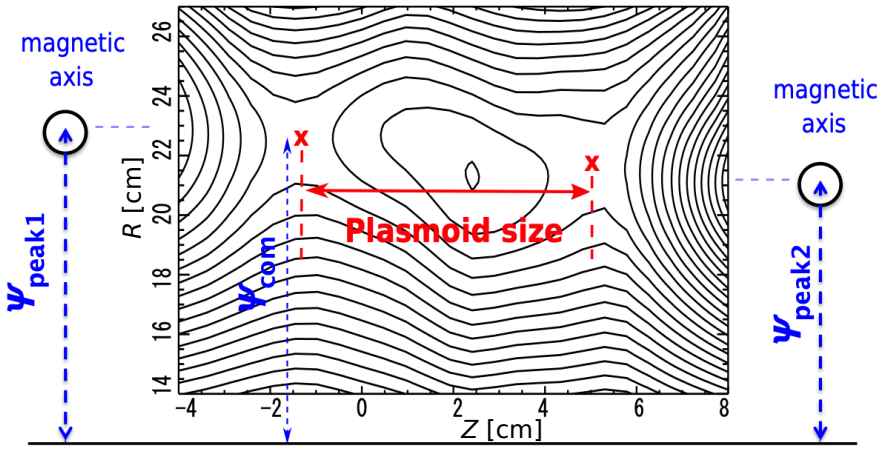

Fig. 4.12 Definition of plasmoid size (axial distance between two X-points), common flux, and peak flux.

field lines of the two major tokamak plasmas are unable to directly contact each other, so the magnetic reconnection is inhibited. Magnetic reconnection speed is slow but the plasmoid grows and plasma piles up in the current sheet. In the plasma pileup process (454 $\sim$ 457 μs), the situation is similar to the above process, but since the plasmoid has begun to merging with the left tokamak plasma, the reconnection speed become somewhat fast. During the plasmoid absorption process, the reconnection speed gradually increases at first. But as the plasmoid is almost absorbed into the two STs, its flux decrease to a certain value, the merging between it and the STs can not continue. In addition, because the plasmoid has not completely disappeared yet, acting as an obstacle between the plasmoid and the STs. Although the two STs approach each other, their private flux are unable to reconnect. Furthermore, there is an inevitable natural decay of common flux. Above reasons cause a temporary decrease of the reconnection speed. Right after the fully absorption of the plasmoid, the velocities of the two STs in the left and right side reaches about 60 km/s and 20 km/s, respectively; both the common flux ratio and reconnection speed increase rapidly and significantly, as shown in Fig. 4.13 (d - e). The absorption of the plasmoid is considered to trigger the initial fast reconnection (initial fast phase).

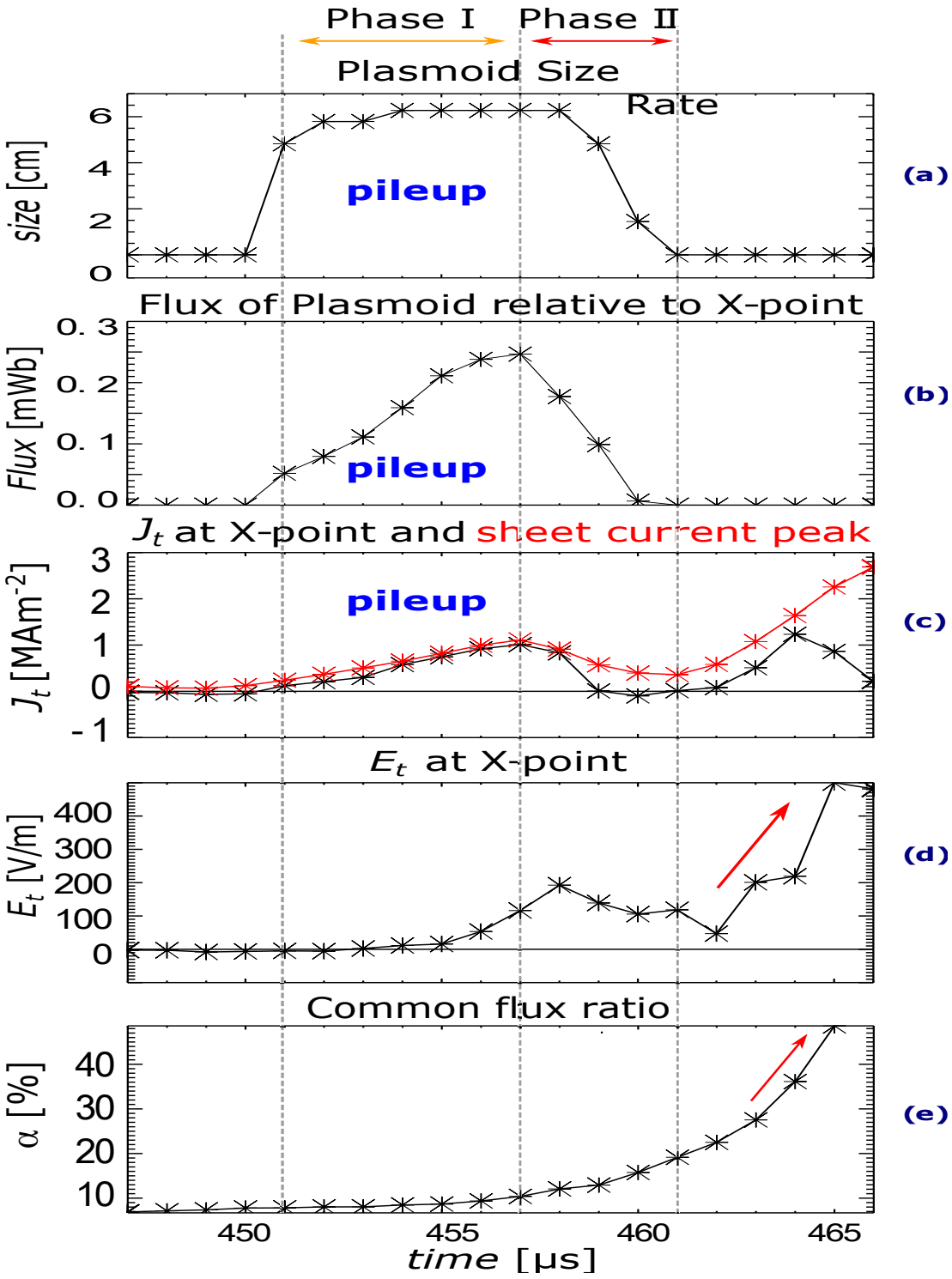

Fig. 4.13 Evolution of (a) the plasmoid size defined by the axial interval between two X-points, (b) plasmoid flux relative to common flux, (c) current density J_t at the current sheet peak (red) and the dominant X-point (black), (d) reconnection electric field E_t (Reconnection speed), (e) The reconnection rate which is the ratio of common flux to peak flux at magnetic axis of merging tokamak plasma.

4.6 Plasma Heating Characteristics around the Plasmoid

4.6.1 Ion Heating around the Plasmoid

2D ion temperature profile is measured by the 2D ion Doppler tomography system with 288 channels. The system consists of axial 18 channels and radial 16 channels, its measurement region is shown in Fig 3.6. The axial channels are located in the range of - 8 $\sim$ 9 cm wth a interval of ΔZ = 1 cm, while radial channels are located in the range of 7.7 $\sim$ 27 cm with non-uniform interval of ΔR = 1.1 $\sim$ 1.3 cm. Its spacial resolution satisfying the ion-gyro scale, has been confirmed that it is available to investigate the fine structure of reconnection heating in the reconnection region [18].

Figure 4.14 shows the ion heating profile together with the 2D magnetic flux profile at the five characteristic time frames of t = 49, 52, 55, 58 and 61 μs in the early reconnection phase. At t = 49 μs, ion heating is almost not visible. At t = 52 μs, ion temperature increases around the new X-point as well as the downstream outflow from the original X-point (left). At t = 55 and 58 μs, the heating of downstream ion from X-points and ion at the new X-point increase effectively. At t = 61 μs, right after the fully absorption of the plasmoid into the STs, downstream ion is heated up to 10 $\sim$ 12 eV due to the bi-directional reconnection outflow from the X-points.

Right after the plasmoid absorption, the common flux ratio α reaches about 20% and the downstream ion T_i reaches about 10 $\sim$ 12 eV, while the maximum of T_i is about 30eV after merging (α = 100%). It suggests that a considerable amount of magnetic energy stored around the current sheets during the plasmoid formation is converted to thermal and kinetic energy of ions, providing the initial ion heating for the merging tokamaks.

4.6.2 Electron Heating around the Plasmoid

Figure 4.15 only shows a 2D contour of electron temperature and poloidal magnetic flux on the left side of the plasmoid (Z = - 20 $\sim$ 0 cm), due to the limitation of the Langmuir probe measurement. However, It can be seen that the electrons are not heated too much in the outflow area, but on the contrary, the heating effect near the current sheet is obvious, reaching a peak near the X-point.

Since the mass of electrons is much smaller than that of ions, they are more easily accelerated than ions in the area where electric field and toroidal current are concentrated. This agrees with the experimental results of electron heating and accelerating around X-point in the current sheet. Due to the limitation of the channels of the Langmuir probe, the 2D global distribution of electron temperature can only be obtained by multi-shot scanning, and the scan date is limited by the reproducibility of the plasma, so it is somewhat inaccurate.

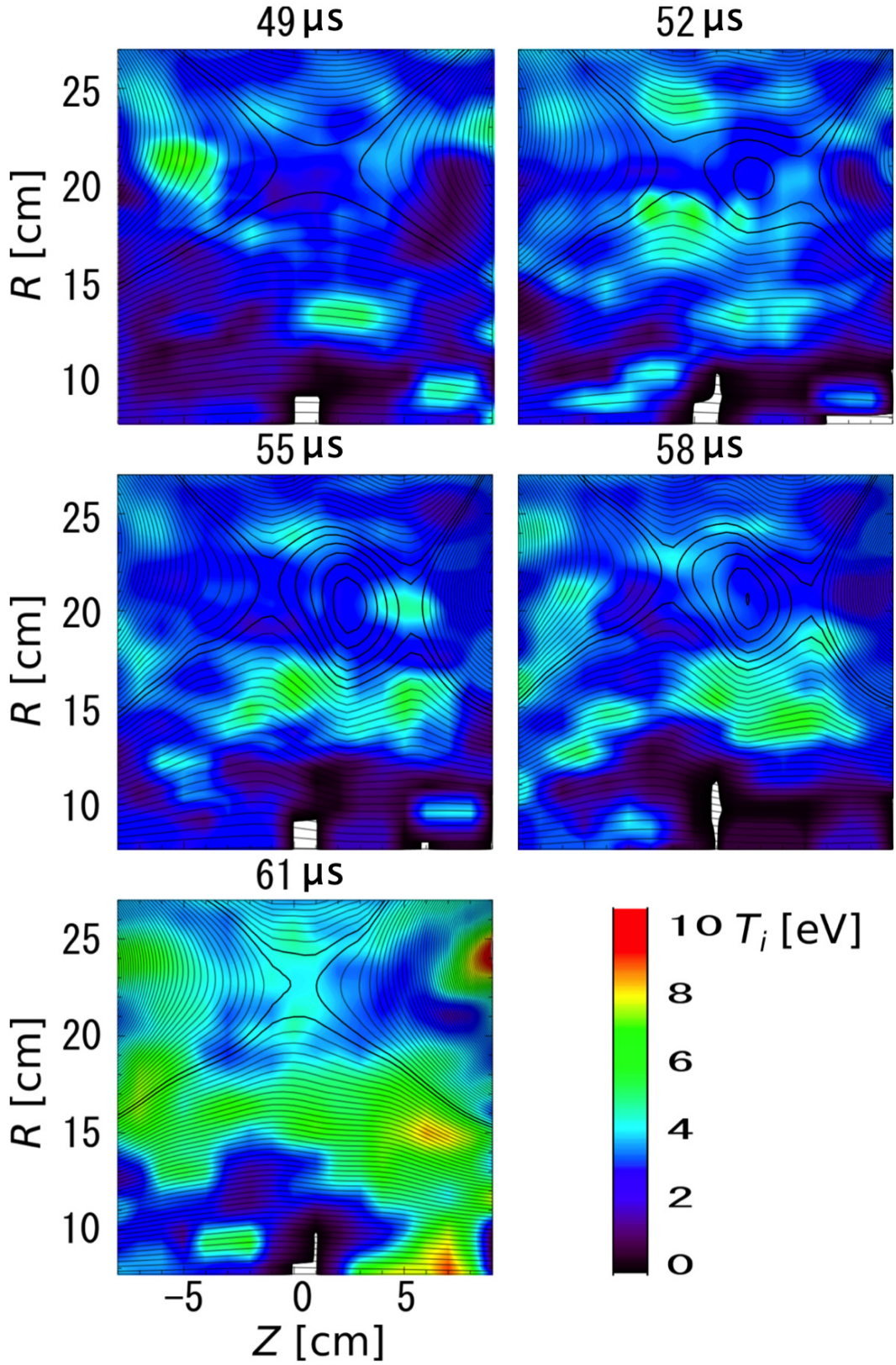

Fig. 4.14 2D ion temperature profile around the plasmoid. It is measured by a 2D high-resolution ion Doppler tomography system. The downstream ion of the two outflows flowing toward the center are heated effectively, especially when the plasmoid are completely merged, ion heating is significantly. The formation and absorption of the plasmoid allows an initial ion heating.

From the Fig. 4.13 (e), we can see that at the end of the initial fast reconnection, reconnection rate reaches up to about 50 %. It suggests that a considerable amount of magnetic energy is converted to thermal energy and kinetic energy of ions. Figure 4.14 and Fig. 4.15 show that the ion and electron temperature can reach up to about half of their maximum value in the whole reconnection period, so the proportion of the initial plasma heating is quite large and should not be ignored.

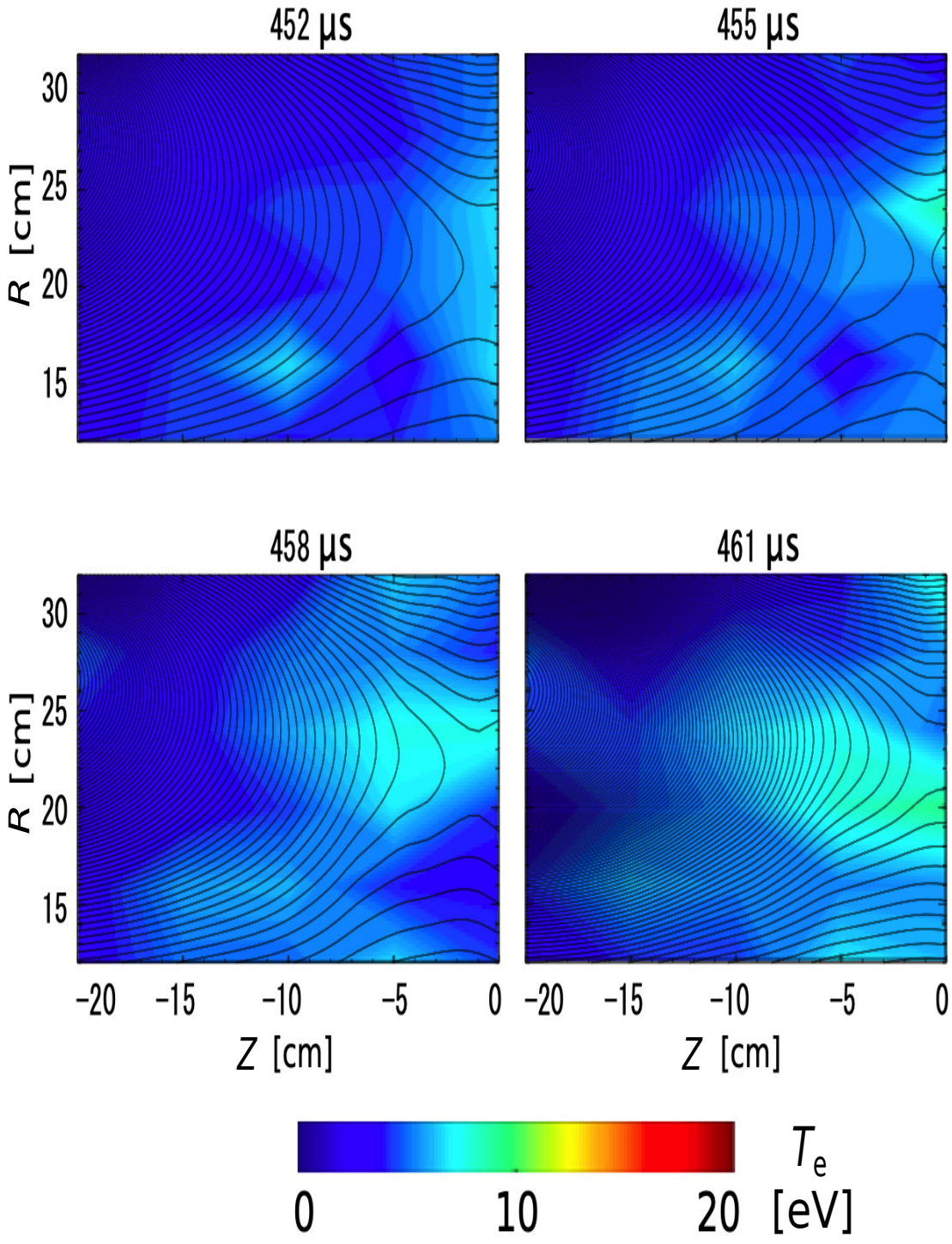

Fig. 4.15 2D electron temperature distribution around the left X-point. It is measured by the Langmuir probe multi-shot scanning.

4.7 Plasma Density around the Plasmoid

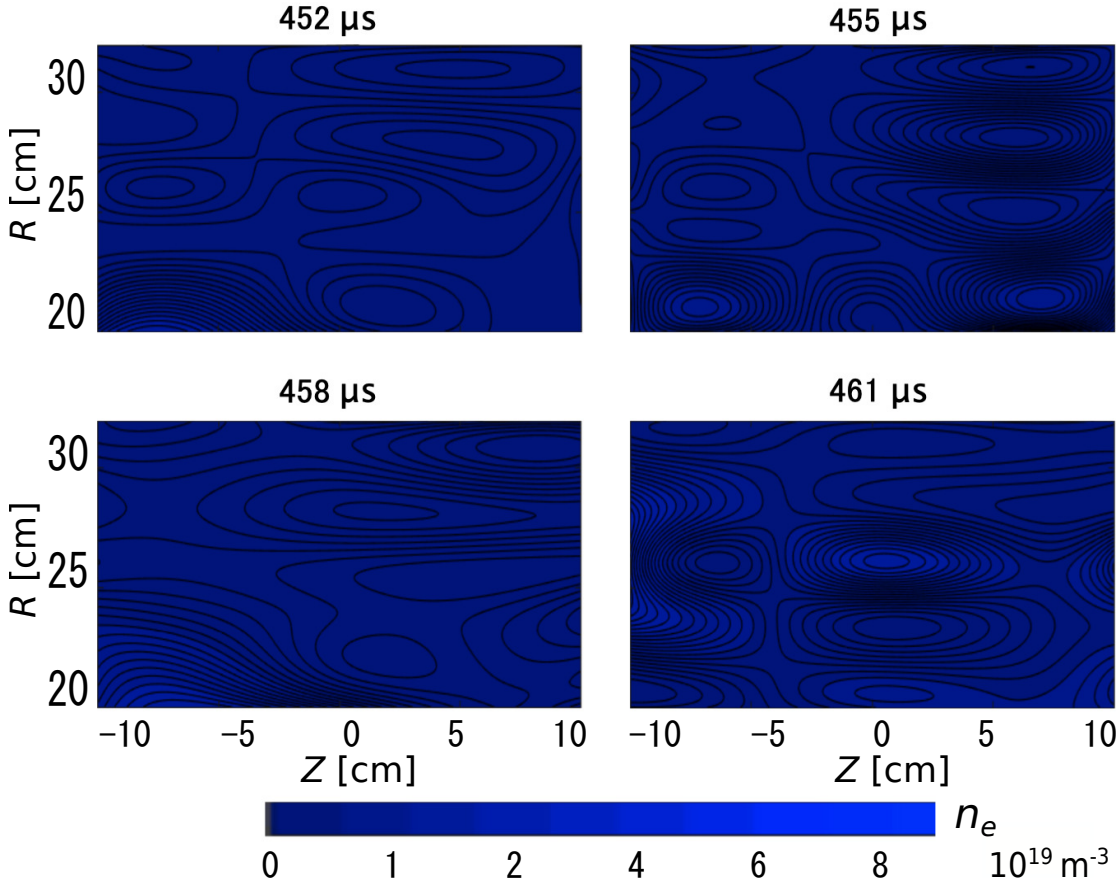

Fig. 4.16 2D electron density distribution around the left X-point. It is measured by the Langmuir probe multi-shot scanning.

CHAPTER 5

The Characteristics of the Plasmoid

5.1 Plasmoid Formation Independent of the Gas Species

In order to investigate the dependence of the plasmoid formation on the gas species in the early phase of magnetic reconnection, the experiments are performed with the hydrogen and argon which differ greatly in ion mass, respectively. For each gas species, multi-shot experiments at various discharge gas pressure are conducted. The results show that above a certain discharge pressure, the plasmoid is always generated. It suggests that the formation of the plasmoid does not depend on the gas species, meaning that it does not depend on the ion mass. The conclusion can be explicated by the fact that in the early merging phase, the plasma temperature is low and the scale of the plasmoid is large, the spontaneous formation of the plasmoid is independent of the ion gyro-radius (ion mass or ion species).

5.2 The Plasmoid in Different Operation Conditions

The spontaneous formation of the plasmoid in the early phase of reconnection is not observed in the experiments with extremely low discharge gas pressure, either in hydrogen plasma discharge or argon plasma discharge. The approximate threshold values of the discharge pressure of hydrogen and argon that can form a plasmoid are 0.32 mTorr and 0.04 mTorr, respectively. Figure 5.1 shows an example of experimental operation (H: 0.32 mTorr) without forming a plasmoid.

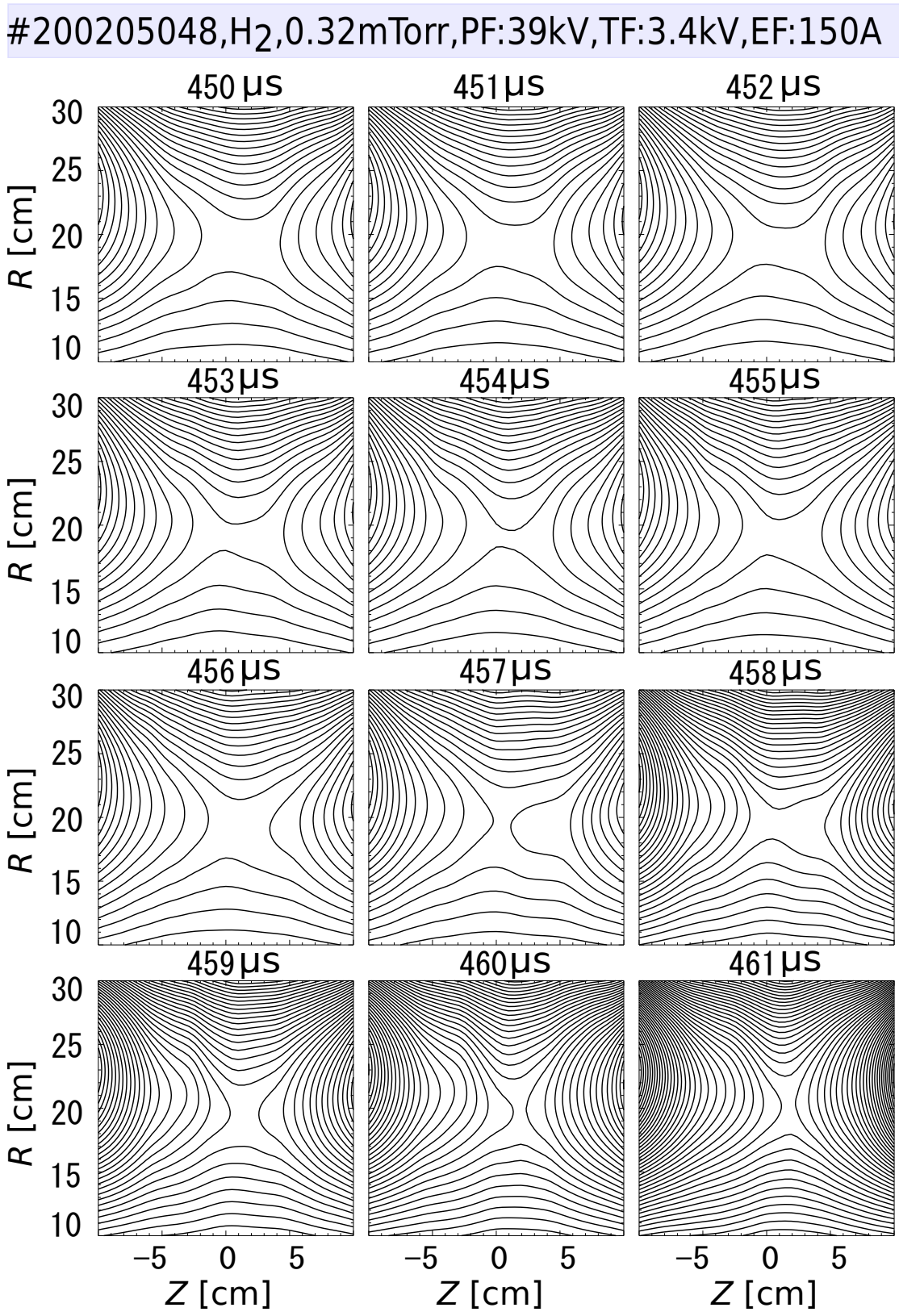

Fig. 5.1 Evolution of the 2D contour of the poloidal magnetic flux, without forming a plasmoid. Hydrogen pressure: 0.32 mTorr.

The dependence of the plasmoid on the gas pressure and guide field ratio is investigated by performing three operations at each discharge gas pressure. In each gas pressure, the voltage of the TF coil is charged to 2.5 kV, 3.0kV, and 3.4kV, respectively, while the PF discharge voltage and EF coil current are kept unchanged. The temporal evolution of the axial size of the plasmoid are shown in Fig. 5.2 - 5.4.

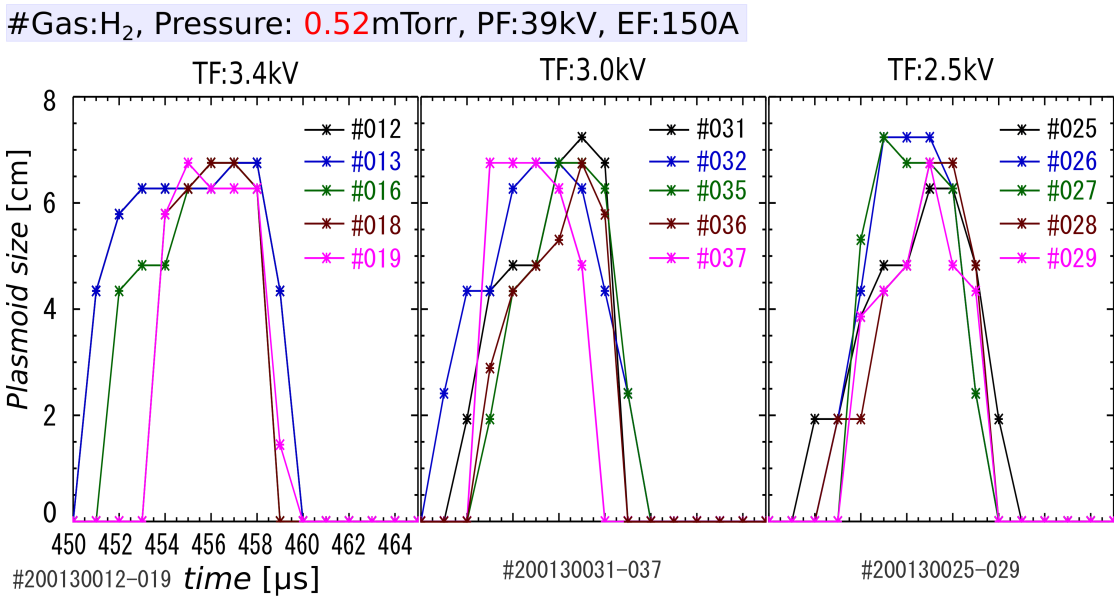

Fig. 5.2 The temporal evolution of the axial size of the plasmoid at 0.52 mTorr of gas pressure. The duration of the plasmoid can be read from the time axis.

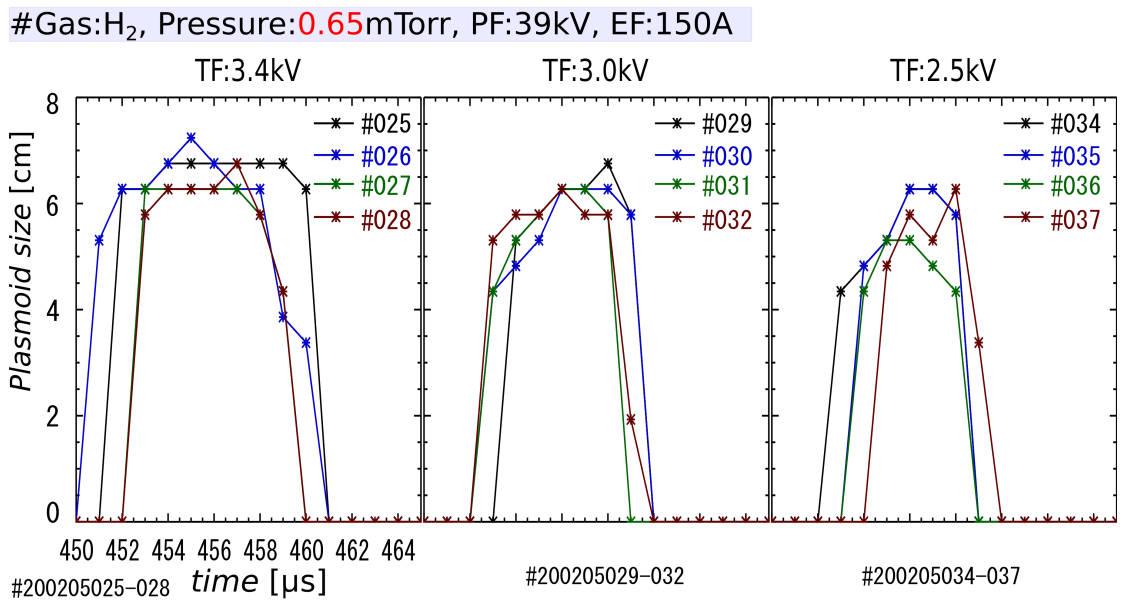

Fig. 5.3 The temporal evolution of the axial size of the plasmoid at 0.65 mTorr of gas pressure. The duration of the plasmoid can be read from the time axis.

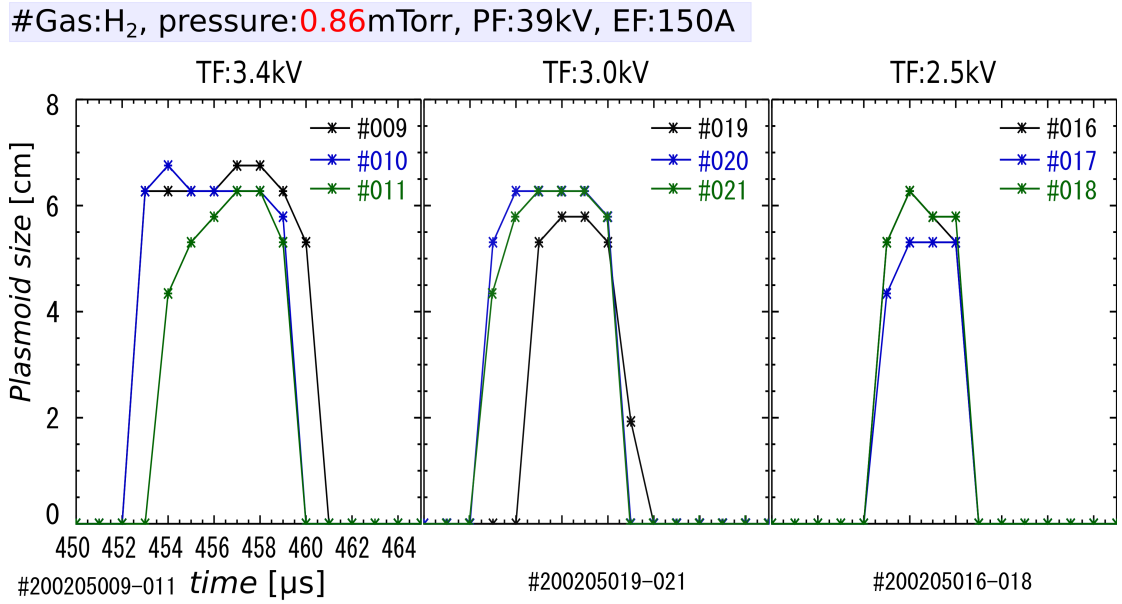

Fig. 5.4 The temporal evolution of the axial size of the plasmoid at 0.86 mTorr of gas pressure. The duration of the plasmoid can be read from the time axis.

5.3 Relationship between Axial Maximum Size and Guide Field Ratio

The relationship between the axial maximum size of the plasmoid and guide field ratio is shown in Fig. 5.5. The plasmoid size shown in Fig. 5.5 is calculated from the mean of the axial maximum sizes of the plasmoid of multiple shots in the same operation, and the error bar is calculated by the standard deviation. The result indicates that, in relatively lower gas pressure discharge experiments (H: 0.52 mTorr), the axial scale of the plasmoid is larger and constant, independent of the guide field ratio $\frac{B_g}{B_r}$; in relatively higher pressure discharge experiments (0.65 mTorr and 0.86 mTorr), the plasmoid size increases slightly as the guide field ratio increases, and the evolutions of them are almost the same; at high guide field ratio, the size of plasmoids in all gas pressure cases tends to be constant; interestingly, the larger the guide field ratio is, the more stable the reproducibility of the plasmoid (smaller error bar) is.

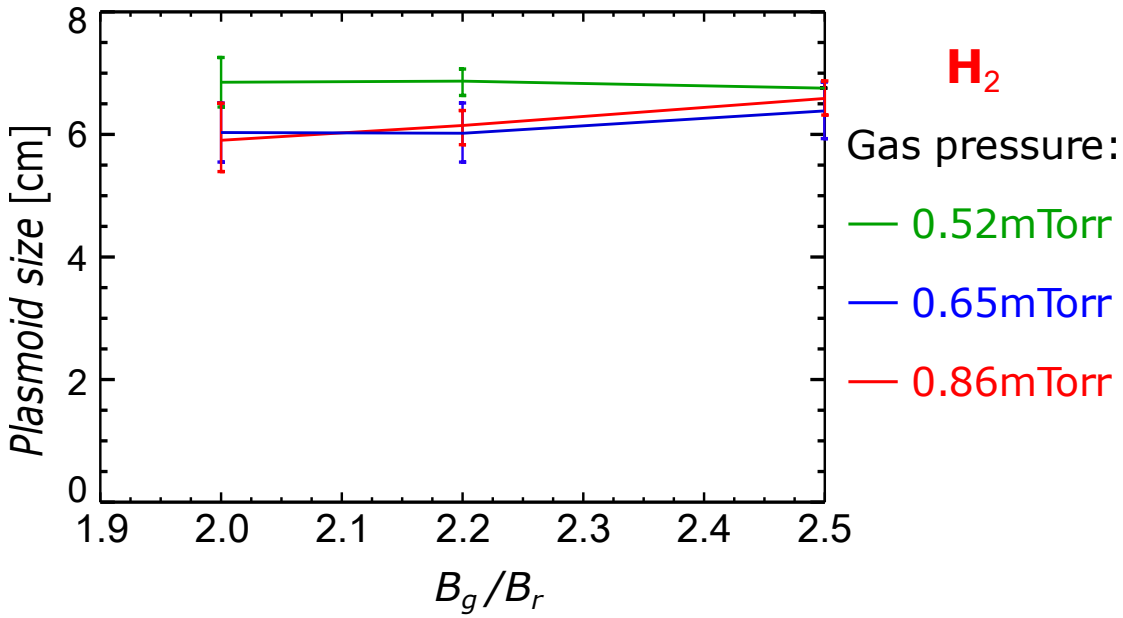

Fig. 5.5 The relationship between the axial maximum size of the plasmoid and the guide field ratio $\frac{B_g}{B_r}$. The plasmoid size is the mean of the axial maximum size of the plasmoid in multiple shots at the same gas pressure. The axial scale of the plasmoid tends to be consistent when the $\frac{B_g}{B_r}$ is the same under the three gas pressure, in the high-guide field ratio experiment.

5.4 Relationship between Duration and Guide Field Ratio

Figure 5.6 shows the relationship between the plasmoid duration and the guide field ratio. The plasmoid duration and its error bar are calculated using the same method as the plasmoid size shown in Fig. 5.5. The result shows that, in lowest gas pressure discharge experiments (H: 0.52 mTorr), the plasmoid duration is larger and constant, almost independent of the guide field ratio $\frac{B_g}{B_r}$, similar to the event of the plasmoid size; at low guide field ratio, the lower the gas pressure is, the longer the plasmoid duration is; as the guide field ratio increases, the difference in the plasmoid durations in various situations becomes smaller; at high guide field ratio, they tend to be constant, which is consistent with the dependence of the plasmoid size on the guide field ratio; but the larger the guide field ratio is, the bigger the error bar of the plamsoid duration is, which is opposite to the event of the plasmoid size.

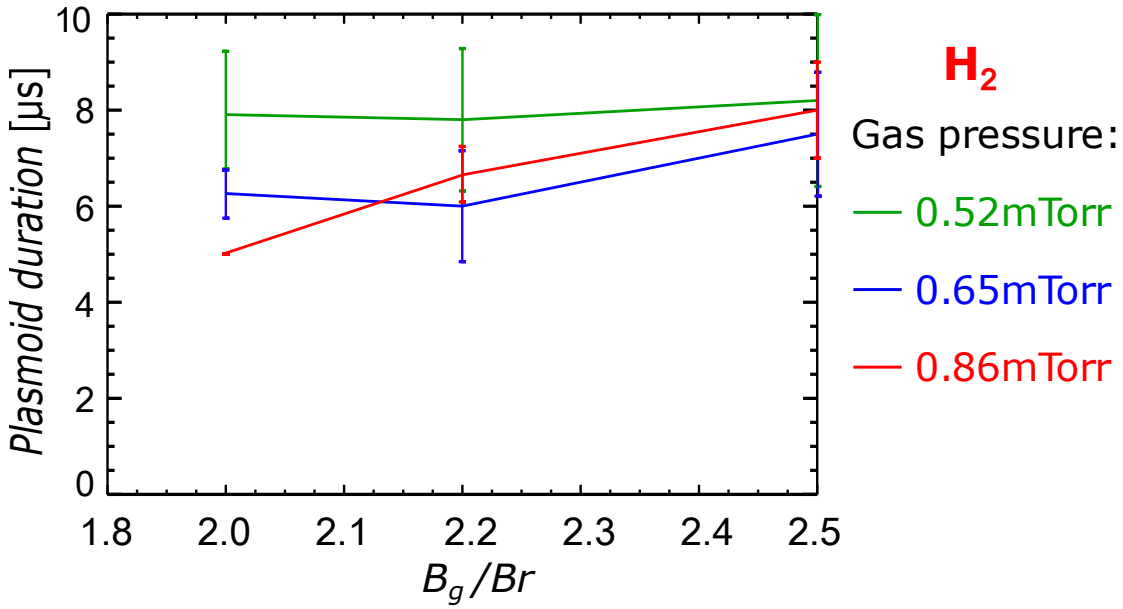

Fig. 5.6 The relationship between the duration of the plasmoid and the guide field ratio $\frac{B_g}{B_r}$. The plasmoid duration tends to be consistent when the $\frac{B_g}{B_r}$ is the same under the three gas pressure, in the high-guide field ratio experiment.

The characteristics of the plasmoid duration and size in high guide field ratio experiments are similar.

CHAPTER 6

Dynamics of Plasmoid with Antiparallel Plasma Current in Main Reconnection Phase of Two Merging Tokamak Plasmas

6.1 Evolution of the Current Sheet

The plasmoid absorption in the early phase of the reconnection triggers the reconnection to the initial fast reconnection. The first fast reconnection lasts a few microseconds, during which a current sheet is quickly formed as shown in Fig. 6.1.

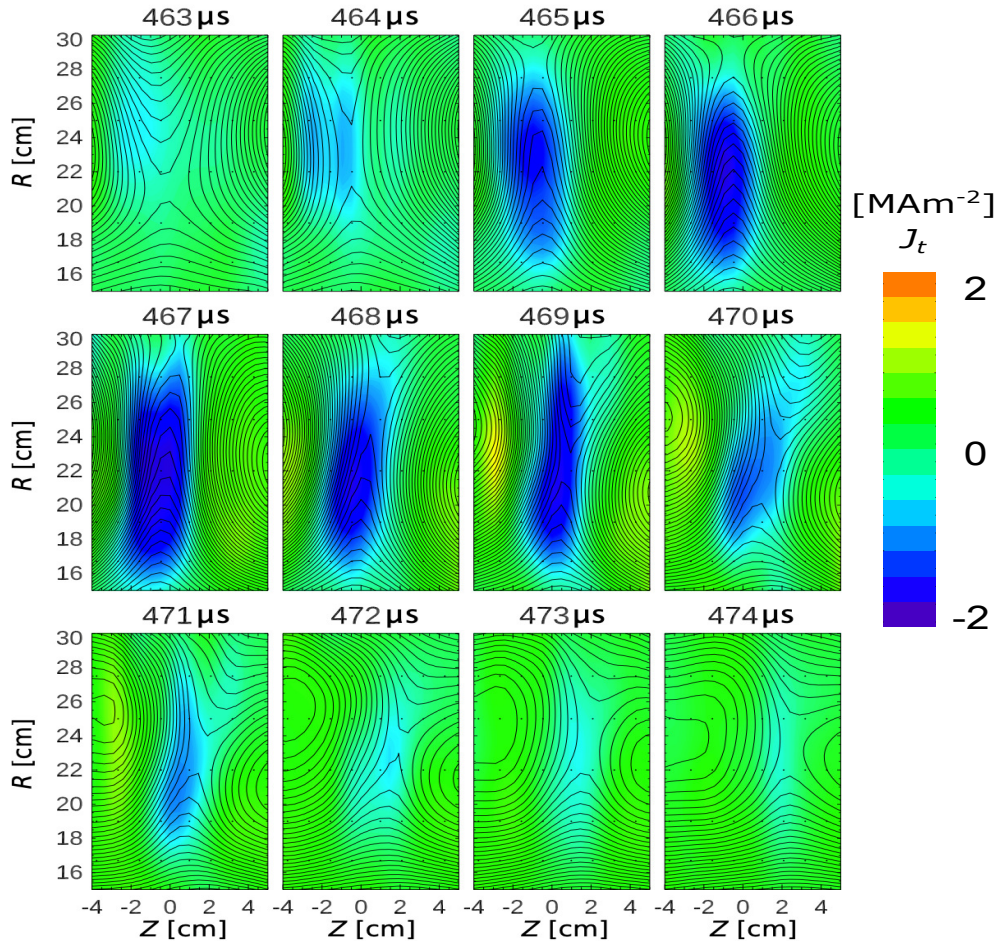

Fig. 6.1 Evolution of the current sheet. The current sheet is quickly formed and then compressed into an elongated rectangular shape.

Figure 6.2 (a) shows the temporal evolution of the axial position of the X-point and two magnetic axes. When the magnetic axes reach their maximum velocities at 466 μs, the density of sheet current peaks while the current density at X-point is weakest, as shown in Fig. 6.2 (b) and (c). Then the plasma piles up in the current sheet, at the same time, the current sheet is approximately compressed into an elongated rectangular shape shown in Fig. 6.1, and the peak density of the sheet current almost does not change, as shown in Fig. 6.2 (c).

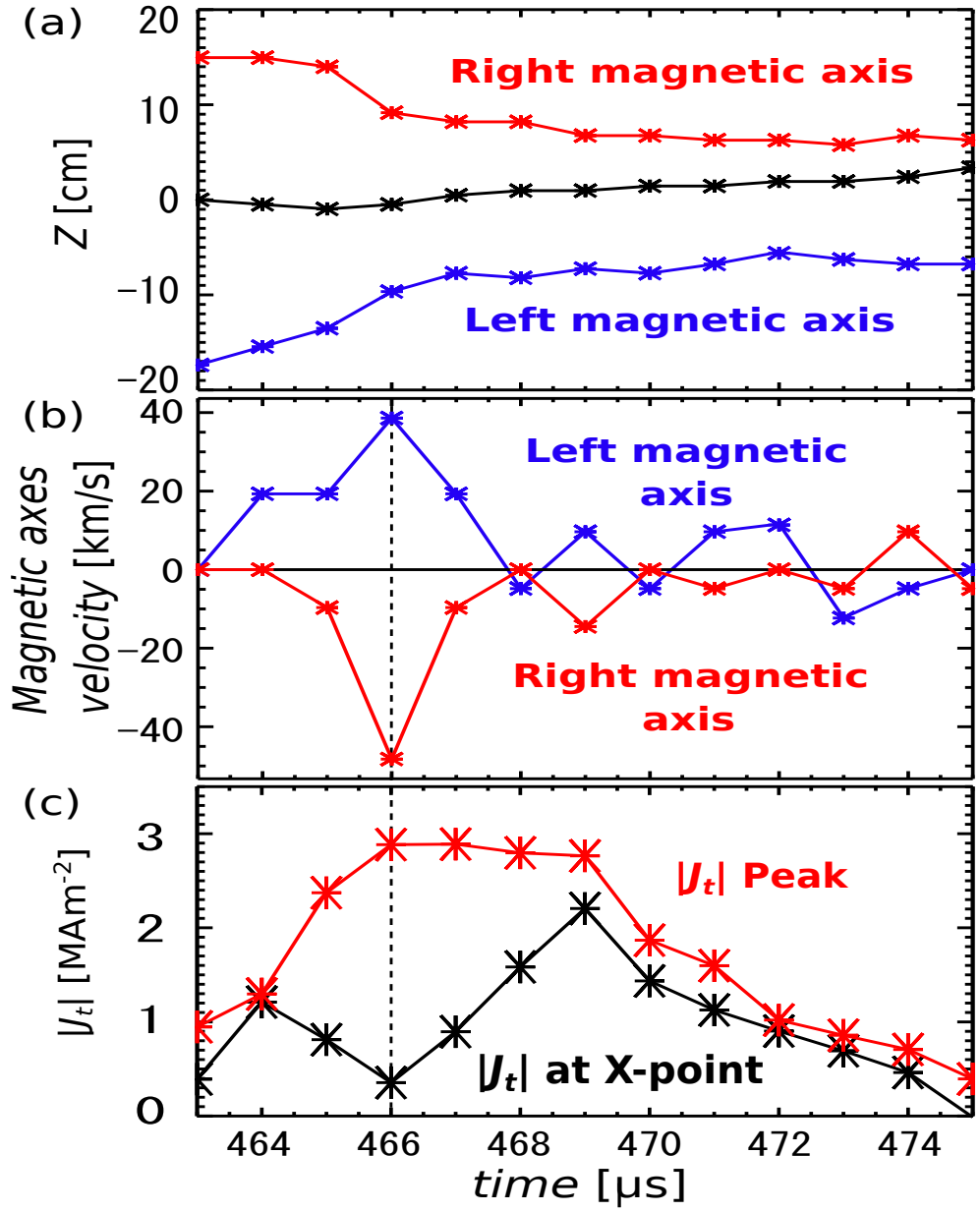

Fig. 6.2 (a) Evolution of the axial position of the X-point and magnetic axes of the tokamak plasmas. (b) Evolution of the velocity of the two magnetic axes. (c) Evolution of the current density $|J_t|$ at X-point (black) and $|J_t|$ peak (red). When the velocity of the magnetic axes reaches peak value 40 km/s, the density of the sheet current peaks.

6.2 Radial shift of the X-point

The initial fast reconnection is so fast that the newly reconnected flux is rapidly accumulated around the X-point. And at the same time, the common flux together with the current sheet is strongly compressed into an elongated shape by the two approaching tokamaks, causing the X-point to quickly shift outward while the density peak of the sheet current moves inward in the radial direction, as shown in the Fig. 6.3 (a). As the magnetic reconnection continues, the common flux is almost compressed into antiparallel lines, resulting in the weakening of the tensor force of the outflow. Therefore, the common flux continues to accumulate, and the X-point continues to shift outward, forming a transition phase of the magnetic reconnection, during which the plasma piles up in the current sheet. During the transition phase, the reconnection rate defined as the ratio of the common flux to peak poloidal flux at the magnetic axis of the merging tokamak plasma, increases very slowly, as shown in the Fig. 6.3 (b).

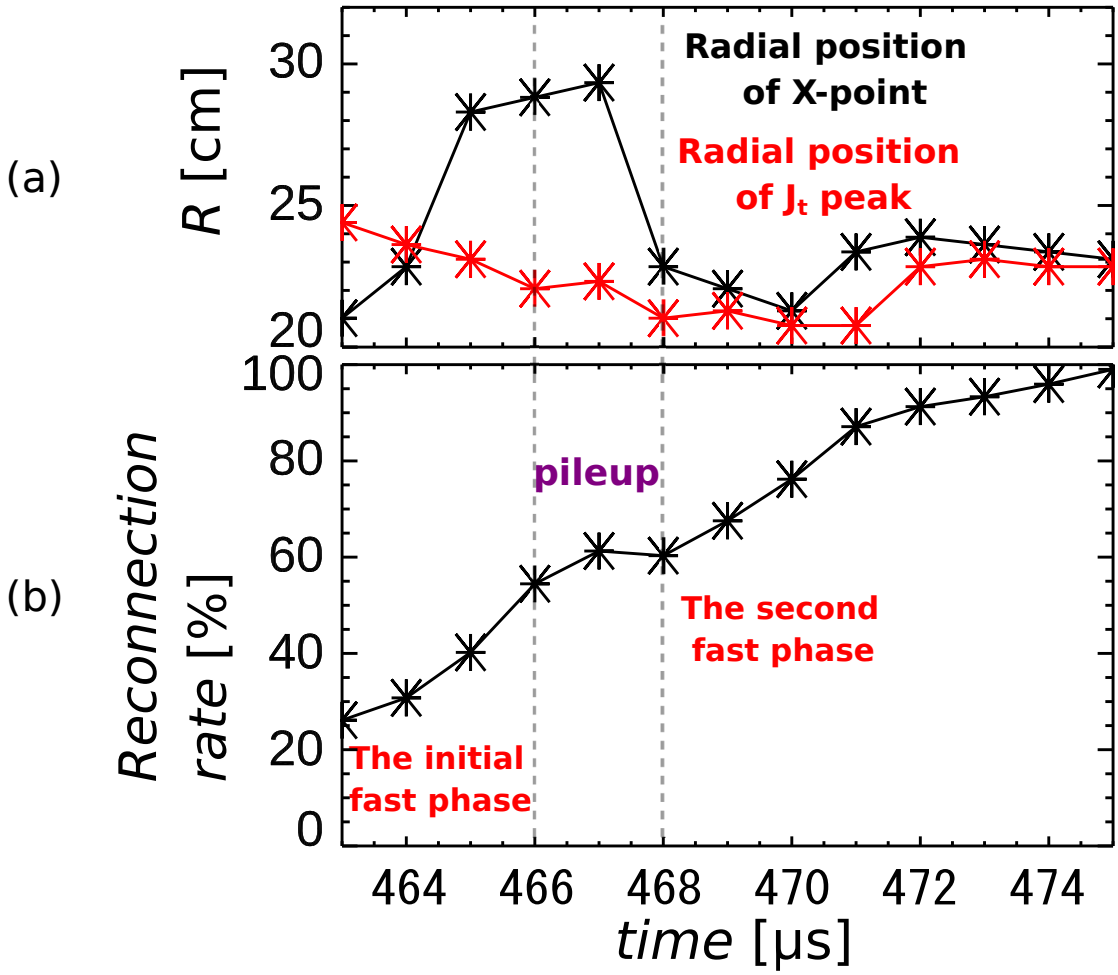

Fig. 6.3 (a) Evolution of the radial position of the X-point and the density peak of the current sheet. (b) Evolution of reconnection rate. The reconnection rate is the ratio of the common flux to peak poloidal flux at the magnetic axis.

6.3 Driven Formation of Plasmoid with Antiparallel Plasma Current in Current Sheet

During the transition phase (or plasma pileup phase), when the antiparallel lines of the common flux contact each other and reconnect, forming a new X-point and a plasmoid with antiparallel plasma current inside the current sheet, an shown in the Fig. 6.4. This plasmoid is completely differently from the plasmoid formed in the early phase of the magnetic reconnection.

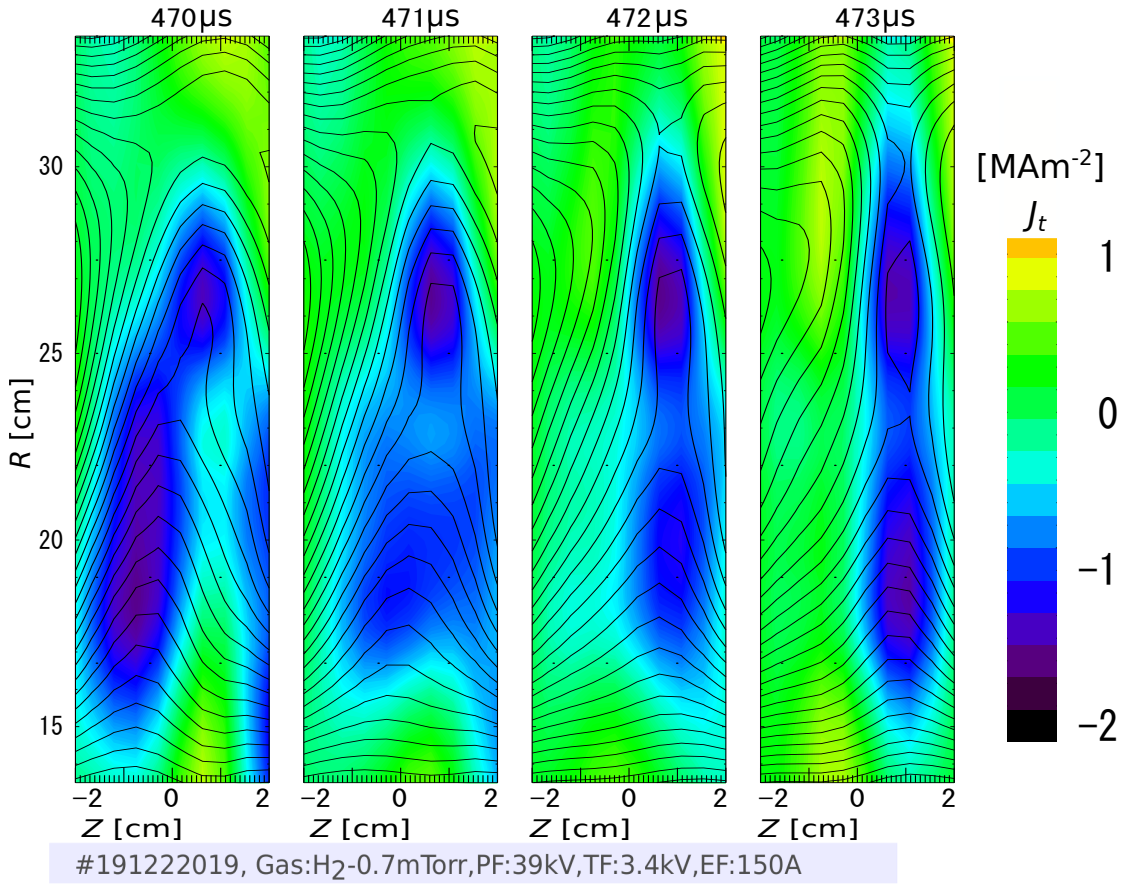

Fig. 6.4 A plasmoid with antiparallel plasma current is formed of common flux in the current sheet.

6.4 Effect of Plasmoid Ejection on Reconnection Speed

When the plasmoid is formed, the current sheet is torn and divided into two parts. The two current sheets move radially outward an inward, respectively, forming the current sheet ejection, as shown in Fig. 6.5. The ejection of the current sheet and plasmoid triggers the reconnection to an impulsive phase, as shown in Fig. 6.6.

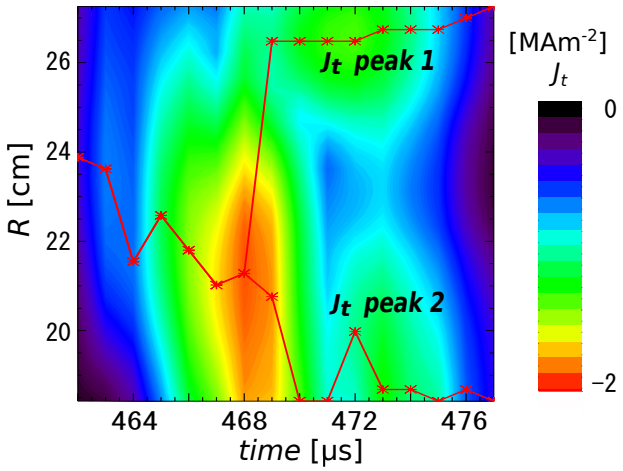

Fig. 6.5 The trace of the density peak of the current sheet. The current sheet splits into two parts after the plasmoid is formed.

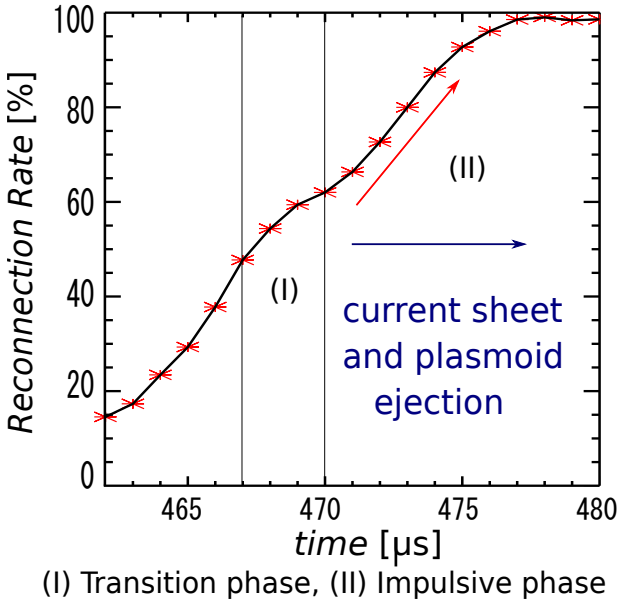

Fig. 6.6 Evolution of the reconnection rate. (I) shows transition phase. (II) shows impulsive phase. When the current sheet is torn and ejected outward together with the plasmoid, fast impulsive reconnection is triggered.

6.5 Reconnection Rate with/without Plasmoid Formation

In order to investigate the effect of the plasmoid on the reconnection rate, we tend to analyze two different cases with/without plasmoid formation. Even the operating conditions for the experiments are the same, the experimental results seem to be different. Due to the reproducibility and uncertainty of the plasma, the experimental results are divided into two cases. In the case A, the plasmoid is only formed in the early phase of the reconnection, and its current is parallel to the tokamak plasma currents. Let's call it an early plasmoid. In the case B, the plasmoid is formed not only in the early phase but also in the transition phase of the reconnection.

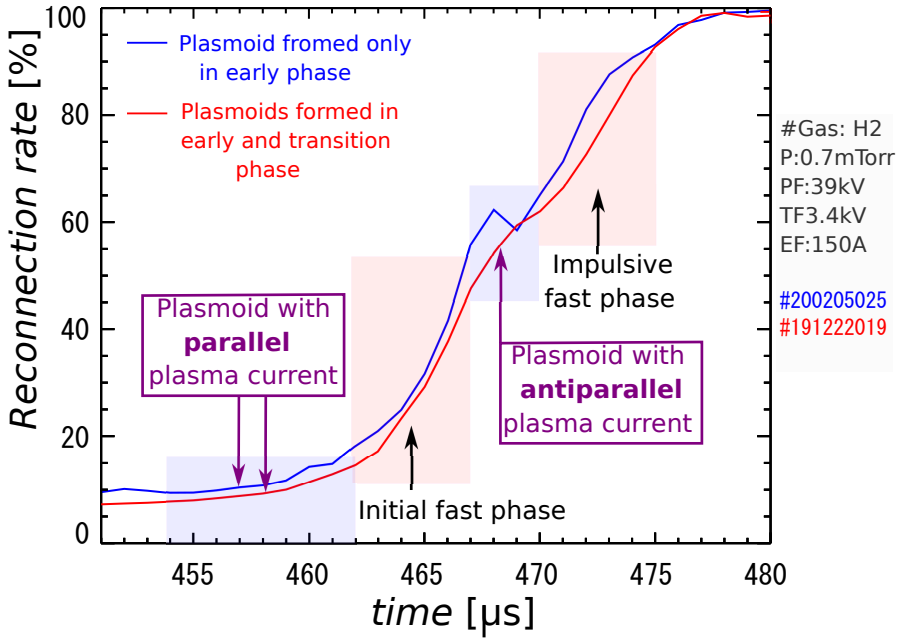

Fig. 6.7 Evolution of the reconnection rate in two cases. Case A (blue): the plasmoid is only formed in the early phase of the reconnection. Case B (red): the two types of plasmoid are formed in the early and transition phase, respectively.

The first plasmoid is the same type of the early plasmoid of the case A, while the second plasmoid with antiparallel plasma current is formed in the current sheet. The early plasmoid is always formed except in extremely low gas pressure as described in the chapter 5, while the probability of the formation of the second plasmoid is very low. The reconnection rate of two cases is shown in Fig. 6.7. The plasma piled up in the transition phase is released in a short time, usually accompanied by the current sheet ejection, which triggers the second fast phase of the reconnection. Owing to the short duration of the second plasmoid and the limitation of the radial and temporal resolution of the magnetic probe array, the effect of the plasmoid ejection on reconnection speed/rate remains unsolved.

6.6 Effect of Current Sheet Ejection on Plasma Heating

During the second fast phase of the reconnection, when the current sheet is ejected outward inboard, maybe accompanied by plasmoid ejection, the ion is heated effectively and significantly in downstream outflow, as shown in Fig. 6.8. However, due to the limitation of the spacial and temporal resolution of the ion tomography system and magnetic probe array, and the short duration of the second plasmoid, and since the plasmoid ejection mostly occurs together with the current sheet ejection, the specific effect of the plasmoid ejection on the ion heating is unclear.

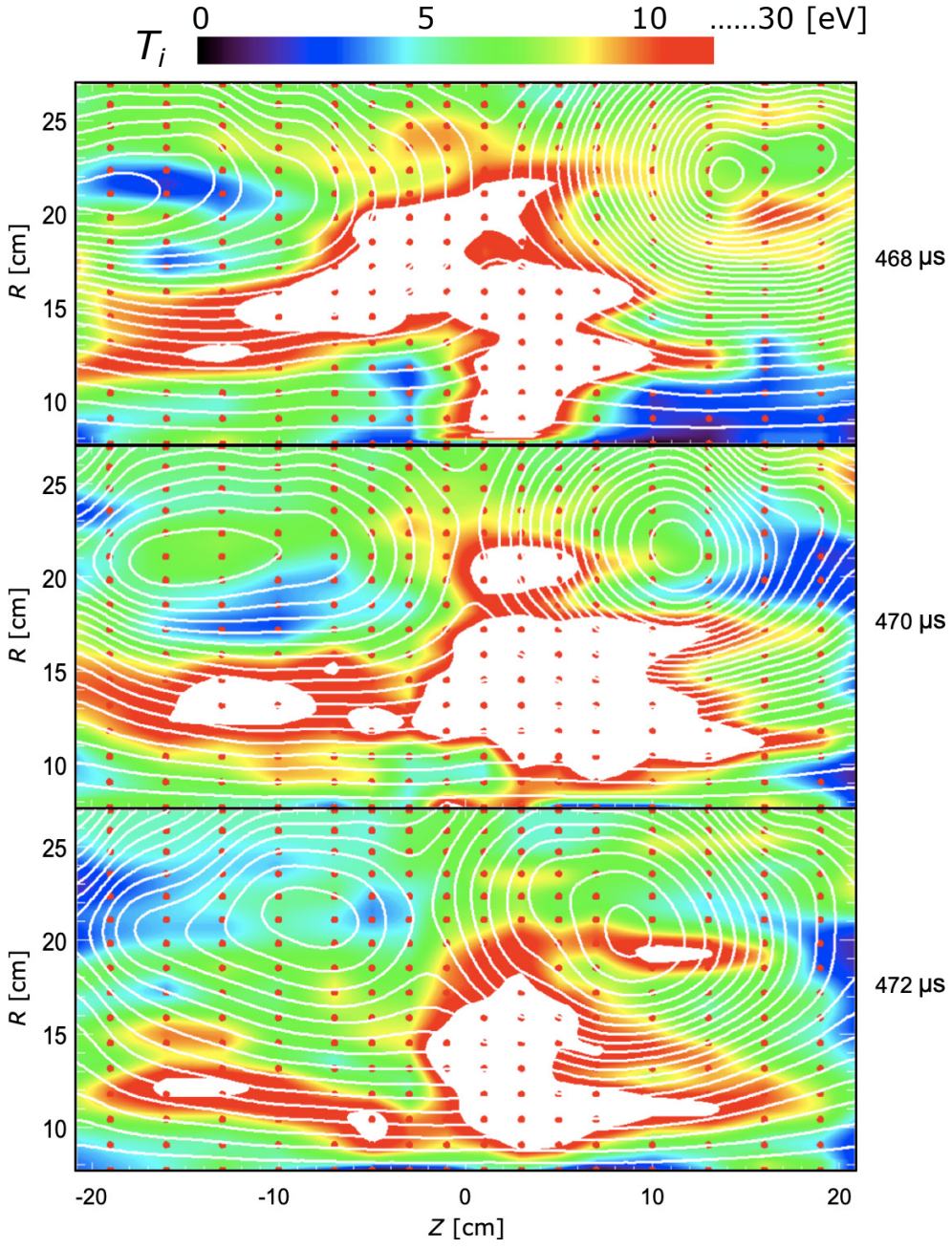

Fig. 6.8 Evolution of ion heating in fast reconnection phase.

CHAPTER 7

Discussion and Conclusions

Our new 2D magnetic probe array satisfies ion-gyro scale spatial resolution though the optimization of pickup coils assembly into a limited space using super-high resolution 3D printer ($\leq$ 16 μm). The plasmoid was clearly observed in the two stages of reconnection process, before the initiation of fast reconnection and before entering the impulsive phase as introduced in previous chapters. In this chapter, we discuss the differences between the two types of plasmoids in terms of generation cause, generation conditions, and so on, and summarize the new findings in the experiments.

7.1 Comparison between Two Types of Plasmoid

- Different formation conditions
  The new type plasmoid in the early reconnection phase is almost always formed except under extremely low gas pressure and/or low guide field (guide field ratio: < 2), while the typical one was unable to be observe in fully compressed current sheet only under the conditions of extremely low gas pressure and high guide field (guide field ratio: $4 \sim 5$). Even in above conditions, the typical plasmoid was not often observed. Perhaps its formation has a certain probability, perhaps it could not be observed due to the temporal constraint of the magnetic diagnostic system.

- Different toroidal current polarity
  The new type plasmoid has parallel plasma current, while the typical one has antiparallel one.

- Different aspect ratio
  Aspect ratio (axial/radial) of the new type plasmoid formed at the beginning of merging is axially elongated, while the aspect ratio of the typical type plasmoid formed at the end of merging is radially elongated.

- Different duration and scale
  The new type plasmoid is characterized by long duration ($\sim$ 9 μs) and large scale ($\sim$ 7 cm), while the typical one is opposite to the former ($\sim$ 1 μs, $\sim$ 1 cm).

- Different plasma parameters
  The plasmoid in early merging phase with the following parameters:
  Radial position of magnetic axes $R \approx 0.28$ m; guide field $B_g \approx 0.15$ T, reconnection field $B_r \approx 0.06 \sim 0.065$ T, guide field ratio $\frac{B_g}{B_r} \approx 2.4$; ion density around the X-point n_i(= n_e) $\approx 1 \sim 2 \times 10^{19}\ m^{-3}$; ion temperature $T_i \approx 10$ eV; electron temperature $T_e \approx 8$ eV.
  The plasmoid in main phase with the following parameters:
  Radial position of magnetic axes $R \approx 0.22$ m; guide field $B_g \approx 0.19$ T, reconnection field $B_r \approx 0.055$ T, guide field ratio $\frac{B_g}{B_r} \approx 3.5$; ion density around X-point n_i (= n_e) $\approx 4 \sim 5 \times 10^{20}\ m^{-3}$; Alfvén velocity $V_A \approx 50 \sim 60$ km/s; ion temperature $T_i \approx 30$ eV; electron temperature $T_e \approx 10$ eV.

Although the plasmoid formation in early phase is seemed to be independent of the gas pressure, the plasmoid was not observed in very low gas pressure experiments. The dependence of the duration and axial scale of the plasmoid on gas pressure and guide field ratio is very slight. It suggests that this plasmoid has a high reproducibility and can be used as a usual phase to increase reconnection speed. The plasmoid in the main reconnection phase was observed only when the current sheet is rapidly compressed to be elongated shape in the high-guide field reconnection experiments, but it does not necessarily appear. Because it occurs too fast and the scale is small, high spatial and temporal resolution magnetic probe array is required. It is difficult to achieve high-resolution in both R and Z directions because of the need to ensure a plasma passing rate in the experiments. Although the current experimental results indicate that the second plasmoid has a poor reproducibility, it may just be that we have not observed it.

7.2 Conclusions

Experimental study of dynamics magnetic reconnection in tokamak plasma merging experiment lead to the following conclusions:

- Two types of plasmoids were observed during the magnetic reconnection of the merging tokamaks. They usually appear asynchronously under different discharge gas pressure condition, occasionally appear synchronously in lower gas pressure.

- When the plasmoid in the early merging phase is fully absorbed to the merging tokamaks, the reconnection increases significantly, and the heating the downstream ion around the plasmoid increases.

- When the plasmoid in the main reconnection phase is ejected with the current sheet, the reconnection increases significantly, and the downstream ion is heated effectively and significantly.

- The plasma piled up during the plasmoid formation process is released rapidly when the plasmoid is completely absorbed. These processes contribute to increase reconnection speed by driving the inflow from the two merging tokamaks and triggers the transition into fast reconnection. At the same time, the accumulated magnetic energy is quickly converted to thermal and kinetic energy of ions. The physical mechanism of the both types of plasmoids on increasing the magnetic reconnection and ion heating is considered to be similar.

Although the two types of the plasmoid are the local structures at around the X-point and needs to be studied in more detail, they were confirmed to trigger the fast reconnection and heat the ion in the downstream outflow.

REFERENCES

[1] International Atomic Energy Agency. Trend in electricity supplied, 2019.

[2] IEA NEWS. Steep decline in nuclear power would threaten energy security and climate goals, 2019.

[3]

[4] G W C Laby and T H Kaye. *Tables of Physical and Chemical Contants*. Middlesex, 2005.

[5] F F. Chen. *INTRODUCTION TO PLASMA PHYSICS AND CONTROLLED FUSION*, volume 1. Springer, 2006.

[6] J. Wssson. *Tokamaks*. Oxford University Press, 2011.

[7] S. Ishida et al. Achievement of high fusion performance in JT-60U reversed shear discharges. *Phys. Rev. Lett.*, 79(20):3917–3921, 1997.

[8] Team JET. Fusion energy production from a deuterium-tritium plasma in the JET tokamak. *Nuclear Fusion*, 32(2):187–203, 1992.

[9] M.G. Bell et al. Overview of DT Results from TFTR. *Nuclear Fusion*, 35(12):1429–1436, 1995.

[10] ITER Organization. ITER Device (iter web site).

[11] M. Gryaznevich et al. Achievement of record β in the start spherical tokamak. *Phys. Rev. Lett.*, 80(18):3972–3975, 1998.

[12] Y. Ono et al. Ion and electron heating characteristics of magnetic reconnection in tokamak plasma merging experiments. *Plasma Physics and Controlled Fusion*, 54(12):124039, 2012.

[13] Y. Ono et al. Ion acceleration and direct ion heating in three-component magnetic reconnection. *Phys. Rev. Lett.*, 76:3328–3331, 1996.

[14] H. Tanabe et al. Two dimensional imaging measurement of magnetic reconnection outflow in the ts-4 toroidal plasma merging experiment. *Plasma and Fusion Research*, 8:2405088–2405088, 2013.

[15] M. Inomoto et al. Centre-solenoid-free merging start-up of spherical tokamak plasmas in utst. *Nuclear Fusion*, 55(3):033013, 2015.

[16] R.J. Akers et al. Neutral beam heating in the START spherical tokamak. *Nuclear Fusion*, 42(2):122–135, 2002.

[17] M. Ono et al. Exploration of spherical torus physics in the NSTX device. *Nuclear Fusion*, 40(3Y):122–135, 2000.

[18] H. Tanabe et al. Investigation of fine structure formation of guide field reconnection during merging plasma startup of spherical tokamak in TS-3U. *Nuclear Fusion*, 59(8):086041, 2019.

[19] R. G. Giovanelli. A Theory of Chromospheric Flares. *Nature*, 158(4003):81–82, 1946.

[20] W. Gonzalez et al. *Magnetic Reconnection Concepts and Applications*. Springer, 2016.

[21] M. Yamada et al. Magnetic Reconnection. *Rev. Mod. Phys.*, 82(1):603–664, 2010.

[22] NASA, GSFC, and SDO. Figure credit: https://svs.gsfc.nas.gov, 2020.

[23] SOHO and NASA. Figure credit: https://earthsky.org/space., 2020.

[24] Gordon Holman and NASA. Figure credit: https://www.researchgate.net., 2020.

[25] NASA. Image credit: https://helios.gsfc.nasa.gov., 2020.

[26] J. W. Dungey. Interplanetary Magnetic Field and the Auroral Zones. *Phys. Rev. Lett.*, 6(2):47–48, 1961.

[27] ESA Science and Technolegy. Articles on measurements made from the Cluster II spacecraft mission, 2020.

[28] J. L. Burch et al. Electron-scale measurements of magnetic reconnection in space. *Science*, 352(6290):aaf2939.

[29] NASA NEWS. THEMIS Satellites Discover What Triggers Eruptions of the Northern Lights, 2008.

[30] V. Angelopoulos et al. Tail reconnection triggering substorm onset. *Science*, 321(5891):931–935.

[31] M. Tariq. Secret of Colorful Auroras Revealed, 2008.

[32] H. Alfven. Existence of Electromagnetic-Hydrodynamic Waves. *Nature*, 150(3805):405–406, 1942.

[33] B. Ghosh. *Basic Plasma Physics*. Alpha Science, 2014.

[34] P.M. Bellan. *Fundamentals of Plasma Physics*. Cambridge University Press, 2008.

[35] K. Shibata and T. Magara. Solar flares: Magnetohydrodynamic Processes. *Living Reviews in Solar Physics*, 8(1):6, 2011.

[36] E. N. Parker. Sweet's mechanism for merging magnetic fields in conducting fluids. *Journal of Geophysical Research*, 62(4):509–520, 1957.

[37] P. A. Sweet. Electromagnetic Phenomena in Cosmical Physics. 1958.

[38] L. Spitzer. *Physics of fully ionized gases*. Interscience Publishers, 1962.

[39] X. Wang. Talking about Magnetic Reconnection (7), 2019.

[40] D. Biskamp. Magnetic reconnection via current sheets. *The Physics of Fluids*, 29(5):1520–1531, 1986.

[41] D. A. Uzdensky and R. M. Kulsrud. Two-dimensional numerical simulation of the resistive reconnection layer. *Physics of Plasmas*, 7(10):4018–4030, 2000.

[42] B. U. Ö. Sonnerup. *Magnetic field reconnection*, volume 3. 1979.

[43] Y. Ono et at. Experimental investigation of three-componebt magnetic reconnection by use of merging spheromak and tokamaks. *Physics of Plasmas*, 4:1953, 1997.

[44] M. Yamada et at. Experimental study of two-fluid effects on magnetic reconnection in laboratory plasma with variable collisionality. *Physics of Plasmas*, 13:052119, 2006.

[45] Y. Ono et al. Intermittent magnetic reconnection in TS-3 merging experiment. *Physics of Plasmas*, 18(11):111213, 2011.

[46] A. Ishizawa and R. Horiuchi. Suppression of Hall-Term Effects by Gyroviscous Cancellation in Steady Collisionless Magnetic Reconnection. *Phys. Rev. Lett.*, 95:045003, 2005.

[47] W.H. Bostick. Experimental Study of Ionized Matter Projected across a Magnetic Field. *Phys. Rev.*, 104(2):292–299, 1956.

[48] J. Lin et al. Plasmoids in reconnecting current sheets: Solar and terrestrial contexts compared. *J. Geophys. Res.*, 113:A11107, 2008.

[49] W. Daughton et al. Fully kinetic simulations of undriven magnetic reconnection with open boundary conditions. *Physics of Plasmas*, 13(7):072101, 2006.

[50] J. F. Drake et al. Formation of secondary islands during magnetic reconnection. *Geophysical Research Letters*, 33(13), 2006.

[51] Y. Liang et al. Observations of secondary structures after collapse events occurring at the $q = 2$ magnetic surface in the TEXTOR tokamak. *Nuclear Fusion*, 47(9):L21–L25, 2007.

[52] R. Samtaney et al. Formation of Plasmoid Chains in Magnetic Reconnection. *Phys. Rev. Lett.*, 103(10):105004, 2009.

[53] M. Inomoto and N. Nishizuka. Plasmoid Ejection and Non-Steady Magnetic Reconnection. *J. Plasma Fusion Res.*, 89(11):769–773, 2013.

[54] K. Shibata and S. Tanuma. Plasmoid-induced-reconnection and fractal reconnection. *Earth, Planets and Space*, 53(6):473–482, 2001.

[55] J. N. Leboeuf et al. Dynamic magnetic x points. *The Physics of Fluids*, 25(5):784–799, 1982.

[56] E. R. Priest. The magnetohydrodynamics of current sheets. *Reports on Progress in Physics*, 48(7):955–1090, 1985.

[57] T. Tajima et al. Current loop coalescence model of solar flares. *The Astrophysical Journal*, 321, 1987.

[58] Y. Hayashi et al. Impulse-type recombination phenomenon of magnetic field lines in plasma (in Japanese). *IEEJ Transactions A*, 132(3):239–244, 2012.

[59] S. Dorfman et al. Three-dimensional, impulsive magnetic reconnection in a laboratory plasma. *Geophysical Research Letters*, 40(2):233–238, 2013.

[60] M. Kawanami. Improvement of spherical tokamak generation efficiency using washer gun type plasma source (in Japanese). *Master Thesis*, 2018.

[61] T. Ii. Generation and maintenance of ultra-high beta torus plasma using high power heating of neutral beam injection and magnetic reconnection (in Japanese). *Doctoral Dissertation*, 2013.

[62] H. Tanaka. Elucidation of global ion heating mechanism of high-guided magnetic field reconnection using spherical tokamak merging (in Japanese). *Master Thesis*, 2020.

[63] T. Uchida and N. Inoue. *Nuclear Fusion and Plasma Control (in Japanese)*, volume 2. 1982.

[64] R. J. Fonck et al. Determination of plasma-ion velocity distribution via charge-exchange recombination spectroscopy. *Phys. Rev. A*, 29(6):3288–3309, 1984.

[65] R C Isler. An overview of charge-exchange spectroscopy as a plasma diagnostic. *Plasma Physics and Controlled Fusion*, 36(2):171–208, 1994.

[66] H. Tanabe. Development of two-dimensional local ion temperature / velocimeter using doppler spectroscopic tomography (in Japanese). *Master Thesis*, 2010.

[67] H. Tanabe. Elucidation of high beta spherical tokamak coalescence formation mechanism using ion doppler tomography (in Japanese). *Doctoral Dissertation*, 2013.

[68] Y. Hayashi. Experimental verification of speeding-up mechanism of magnetic reconnection by unsteady effect (in Japanese). *Doctoral Dissertation*, 2012.

LIST OF PUBLICATIONS

Academic Papers

1. Q. Cao, H. Tanaka, Y. Cai, M. Akimitsu, J. Xiang, H. Tanabe and Y. Ono, "Plasmoid formations and absorption in early merging phase of two tokamak plasmas" (to be submitted)

2. Q. Cao, Y. Cai, M. Akimitsu, J. Xiang, T. Ahmadi, H. Tanaka, H. Tanabe and Y. Ono,"Spontaneous Formation of Plasmoid during Early Magnetic Reconnection Phase of Two Merging Tokamaks", IEEJ Trans. Vol.15, No.9 (2020)

3. H. Tanabe, Q. Cao, H. Tanaka, T. Ahmadi, M. Akimitsu, A. Sawada, M. Inomoto and Y. Ono, "Investigation of fine structure formation of guide field reconnection during merging plasma startup of spherical tokamak in TS-3U", Nuclear Fusion 59, 086041 (2019)

4. H. Tanabe, Q. Cao, H. Tanaka, T. Ahmadi, M. Akimitsu, A. Sawada, M. Inomoto and Y. Ono, "Recent Progress in High Resolution 2D Imaging Measurements of Reconnection Heating during Merging Plasma Startup in TS-3", Plasma and Fusion Research 14, 3401110 (2019)

5. H. Tanaka, Y. Ono, H. Tanabe and Q. Cao, "First Global Doppler Tomography Measurement of Ion Heating of Merging Tokamak Plasmas", IEEJ Trans. FM 139, 8 (2019) (in Japanese)

6. M. Akimitsu, Y. Ono, Q. Cao, R. Masuki and H. Tanabe, "Development of High-resolution Two-dimensional Magnetic Field Measurement System by Use of Printed-circuit Technology',' IEEJ Trans. FM Vol.138, No.9, pp.480-481 (2018) (in Japanese)

7. M. Akimitsu, Y. Ono, Q. Cao and H. Tanabe, "High-Resolution 2D Magnetic Field Measurement of Magnetic Reconnection Using Printed-Circuit Board Coils", Plasma and Fusion Research 13, 1202108 (2018)

8. S. Kamio, Q, Cao, K. Abe, M. Sakumura, N. Suzuki, T.G. Watanabe, K. Ishiguchi, R. Imazawa, T. Yamada, M. Inomoto, Y. Takase and Y. Ono, "Multipoint Spectroscopy Measurement of Spherical Tokamak Heating by Magnetic Reconnection in UTST", Plasma and Fusion Research 6,2402033 (2011)

9. S. Kamio, N.Suzuki, Q, Cao, K. Abe, M. Sakumura, T.G. Watanabe, K. Ishiguchi, R. Imazawa, T. Yamada, M. Inomoto, Y. Takase and Y. Ono, "Development of Multi-channel Doppler Spectroscopic Measurement System Using 8 $\times$ 8 Multinode Photomultiplier Tube Assembly", Rev. Sci. Instrum. 83, 083103 (2012)

10. S. Kamio, K. Yamasaki, K. Takemura, Q, Cao, T.G. Watanabe, H. Itagaki, T. Tsutsui, K. Ishiguchi, R. Imazawa, T. Yamada, C.Z. Cheng, M. Inomoto, Y. Takase and Y. Ono, "Electron Acceleration by Magnetic Reconnection During Spherical Tokamak Merging Experiment", IEEJ Trans. FM 133, 4 (2013)

Conferences

1. Q, Cao, M. Akimitsu, A. Sawada, B. Anup, S. Kamiya, H. Tanaka, Y. Aoyama, E. Kubo, H. Tanabe and Y. Ono, "2D High-Resolution Magnetic Field Measurement of the Merging Tokamak Plasmas in New Reconnection Experiment: TS-6 (3U)", The 35th Annual Meeting, The Japan Society of Plasma Science and Nuclear Fusion Research, Osaka University, Dec. 2018

2. Q. Cao, M. Akimitsu, A. Sawada, B. Anup, S. Kamiya, H. Tanaka, H. Tanabe and Y. Ono, "2D High-Resolution Magnetic Field Measurement of the Merging Tokamak Plasmas in New Reconnection Experiment: TS-3U", The 27th International Toki Conference on Plasma and Fusion Research and The 13th Asia Pacific Plasma Theory Conference, Toki-City, Gifu, Japan, Nov. 2018

3. Q. Cao, M. Akimitsu, A. Sawada, H. Tanabe and Y. Ono, "2D High-Resolution Magnetic Field Measurement of the Merging Tokamak Plasmas in New Recon-

nection Experiment: TS-3U", 12th Nuclear Fusion and Energy Joint Conference, Piazza Tankai, Shiga Prefecture, Jun. 2018

4. Q. Cao, M. Akimitsu, R. Masuki, H. Tanabe and Y. Ono, "2D High-Resolution Measurement of High Guide-Field Magnetic Reconenction in TS-3U Spherical Tokamak Merging Experiment", Plasma Conference, Himeji, Nov. 2017

5. Q. Cao, M. Akimitsu, R. Masuki, H. Tanabe and Y. Ono, "2D High-Resolution Measurement of High Guide-Field Magnetic Reconnection in TS-3U Spherical Tokamak Merging Experiment", 59th Annual Meeting of the APS Division of Plasma Physics, Milwaukee, Wisconsin, Oct. 2017

6. Q. Cao, S. Kamio, N. Suzuki, K. Takemura, H. Itagaki, T. G. Watanabe, K. Yamasaki, K. Ishiguchi, T. Yamada, M. Ionomoto and Y. Ono, "Development of the Visible Light Tomography Diagnostics for UTST Spherical Tokamak Plasmas", 59th Annual Meeting of the APS Division of Plasma Physics, Salt Lake City, Utah, USA, Nov. 2011

7. Q. Cao, S. Kamio, K. Abe, M. Sakumura, N. Suzuki, T. Watanabe, R. Imazawa, T. Yamada, M. Ionomoto Y. Takase and Y. Ono, "Development of the Visible Tomography Measurement for UTST Device", Ookayama Campus, Tokyo Institute of Technology, Sep. 2011

8. Q. Cao, S. Kamio, K. Abe, M. Sakumura, N. Suzuki, T. Watanabe, R. Imazawa, T. Yamada, M. Ionomoto Y. Takase and Y. Ono, "Development of the Visible Light Tomography Measurement in UTST Device", The Institute of Electrical Engineers of Japan, Fundamentals and Materials, The University of Ryukyus, Sep. 2010

9. H. Tanabe, Q. Cao, H. Tanaka, M. Akimitsu, R. Someya, T. Ahmadi, M. Inomoto and Y. Ono, "micro/macro-scale ion heating and transport process of magnetic reconnection during merging plasma startup of TS-6 spherical tokamak", 61th Annual Meeting of the APS Division of Plasma Physics, Florida, USA, Oct. 2019

10. M. Akimitsu, Q. Cao, M. Keisuke, H. Tanaka and Y. Ono, "Plasmoid and blob of current sheet in TS-6 torus plasma merging experiment", HINODE13/OPElS2019, The University of Tokyo, Sep. 2019

11. H. Tanabe, Q. Cao, H. Tanaka, T. Ahmadi, M. Akimitsu, M. Inomoto and Y. Ono, "Experimental study of reconnection heating/transport process and its application to high temperature spherical tokamak formation", 9th East-Asia Schlool and Workshop on Laboratory, Space and Astrophysical Plasmas (EASW9), Nagoya University, Aug. 2019

12. H. Tanabe, Q. Cao, M. Akimitsu, A. Sawada, H. Tanaka, T. Ahmadi, M. Inomoto and Y. Ono, "Fine structure formation by reconnection heating/transport process in toroidal plasma merging experiments", MAX PLANCK PRINCETON CENTER WORKSHOP 2019 (MOCC2019), The University of Tokyo, Feb. 2019

13. M. Akimitsu, Q. Cao, H. Tanaka and Y. Ono, "High Resolution Magnetic Field Measurement of Magnetic Reconnection in TS-6 Device Using Printed-Circuit Board Coils", the 27th International Toki Conference on Plasma and Fusion Research and The 13th Asia Pacific Plasma Theory Conference, Toki-City, Gifu, Japan, Nov. 2018

14. M. Akimitsu, Q. Cao, A. Sawada, H. Tanaka and Y. Ono, "Development of high resolution two-dimensional magnetic field measurement system by use of printed-circuit technology", 59th Annual Meeting of the APS Division of Plasma Physics, Milwaukee, Wisconsin, Oct. 2017

15. H. Tanabe, M. Gryaznevich, Q. Cao, H. Tanaka, T. Ahmadi, M. Akimitsu, C. Z. Cheng, M. Inomoto and Y. Ono, "Ion and electron heating characteristic of magnetic reconnection in high field flux tube merging experiments", HINODE13/OPElS2019, The University of Tokyo, Sep. 2019

16. Y. Ono, H. Tanabe, M. Inomoto, Q. Cao, S. kamiya, H. Tanaka, H. Yamaguchi, C. Z. Cheng, S. Usami, R. Horiuchi, M. Gryaznevich, "Scaling Physics of Reconnection Heating for ST Merging Startup Experiment", International Spherical Tokamak Workshop (ISTW) 2019, Frascatti, Italy, Oct. 2019

17. Y. Ono, H. Tanabe, S. Kamiya, H. Tanaka, Y. Cai, Q. Cao, J. Xiang, M. Gryaznevich, S. Usami and R. Horiuchi,"Scaling Physics of Reconenction Heating and Acceleration in Tokamak Merging Experiments", 61th Annual Meeting of the APS Division of Plasma Physics, Florida, USA, Oct. 2019

18. H. Tanabe, M. Gryaznevich, Q. Cao, H. Tanaka, T. Ahmadi, M. Akimitsu, C. Z. Cheng, M. Inomoto and Y. Ono, "Ion and electron heating characteristic of magnetic reconnection in high field flux tube merging experiments", HINODE13/OPElS2019, The University of Tokyo, Sep. 2019

19. S. Kamio, K. Takemura, Q. Cao, H. Iatagaki, N. Suzuki, T. G. Watanabe, K. Yamasaki, K. Ishiguchi, R. Imazawa, T. Yamada, M. Ionomoto and Y. Ono, "Study of magnetic reconnection heating in UTST measured by Doppler spectroscopy", 21st International Toki Conference, Toki-city, Gifu, Japan, Nov. 2011

20. S. Kamio, K. Takemura, K. Yamasaski, Q. Cao, H. Iatagaki, T. G. Watanabe, T. Yamada, M. Ionomoto and Y. Ono, "Spectroscopic Measurement of Energy Conversion in Magnetic Reconnection during Spherical Tokamak Merging Experiment", 54th Annual Meeting of the APS Division of Plasma Physics, Providence, RI, USA, Oct. 2012